Synchrotron Radiation Sources driven by Laser-Plasma Accelerators

Dissertation zur Erlangung des akademischen Grades

Doctor rerum naturalium (Dr. rer. nat.)

vorgelegt dem Rat der Physikalisch-Astronomischen Fakultät
der Friedrich-Schiller-Universität Jena

von Dipl.-Phys. Hans-Peter Schlenvoigt,
geboren am 14. 01. 1981 in Jena

Gutachter

1. Prof. Dr. Malte C. Kaluza
   Institut für Optik und Quantenelektronik
   Friedrich-Schiller-Universität Jena

2. Prof. Dr. Luis O. Silva
   Instituto de Plasmas e Fusão Nuclear
   Instituto Superior Técnico
   Lissabon – Portugal

3. Prof. Dr. Roland Sauerbrey
   Forschungszentrum Dresden-Rossendorf und TU Dresden

Tag der Disputation: 10. 02. 2009

Zusammenfassung

Diese Arbeit stellt eine neues Verfahren zur Erzeugung von Synchrotronstrahlung vor. Ein Laser-Plasma-Beschleuniger erzeugt hoch-relativistische Elektronenstrahlen, die beim anschließenden Durchgang durch einen Undulator Synchrotronstrahlung erzeugen. Dieses Verfahren wurde zum ersten Mal experimentell umgesetzt, vorerst im sichtbaren Spektralbereich.

Laser-Plasma-Beschleuniger beruhen auf der Wechselwirkung von hochintensiven Laserpulsen mit Plasmen. Dabei werden Plasmawellen, die elektrische Felder bis zu TV/m haben können, erzeugt und zur Teilchenbeschleunigung genutzt. Folglich reduziert sich die Beschleunigungsstrecke auf typischerweise einige Millimeter, was ein markanter Vorteil gegenüber den üblichen Hochfrequenzbeschleunigern ist. Allerdings ist die Wechselwirkung nichtlinear, wodurch die Eigenschaften der Elektronenpulse schwer zu kontrollieren sind. In Experimenten wurde der Prozess untersucht und verbessert.

Die Wechselwirkung wurde mit zeitaufgelösten optischen Methoden untersucht. Insbesondere wurden ringförmige Magnetfelder von einigen Mega-Gauss, die die Elektronenbeschleunigung begleiten, während des Prozesses detektiert. Dadurch gelang es zum ersten Mal, in den Beschleunigungsprozess mit hoher räumlicher und zeitlicher Auflösung hineinzublicken. Weitere Beobachtungsmöglichkeiten gestatteten ein kontrolliertes Einstellen der Wechselwirkungsparameter. Dadurch gelang es, die zur Erzeugung von Synchrotronstrahlung nötigen hochenergetischen und gebündelten Elektronenstrahlen mit hoher Stabilität und Wiederholbarkeit zu erzeugen und dafür zu nutzen.

Die vorgestellten Experimente beweisen zunächst das Prinzip der Methode. Die erzeugten Wellenlängen waren im wesentlichen durch die verfügbaren Elektronenenergien begrenzt. Jedoch gestatten gegenwärtige Entwicklungen im Gebiet der Laser-Teilchen-Beschleunigung in absehbarer Zukunft die Erzeugung kurzwelliger Synchrotronstrahlung. Darüber hinaus scheinen die ultrakurzen Elektronenpulse für den FEL-Betrieb geeignet zu sein, und die inhärente Synchronisierung mit einem Kurzpuls-Lasersystem wird genaueste zeitaufgelöste Untersuchungen gestatten. Insofern stellt das hier präsentierte Verfahren die Grundlage für einen neuen Typ Laser-basierter Strahlungsquellen dar.

Abstract

This thesis presents a novel experimental scheme of producing synchrotron radiation. A compact laser-plasma accelerator generates highly relativistic electron beams. Those are used to produce synchrotron radiation by passing through an undulator. By means of this unique setup, synchrotron radiation in the visible spectral range driven by laser-accelerated, multi-MeV electron beams was observed for the first time.

Laser-plasma accelerators rely on the interaction of an intense and ultra-short laser pulse with plasma. Plasma waves with electric fields on the order of TV/m are created and used for electron acceleration. Consequently, the acceleration length is reduced to a millimeter scale typically, which represent a significant improvement over conventional radio-frequency accelerators. However, the laser-plasma interaction is nonlinear and electron beam properties are difficult to control. In a series of dedicated experiments, the acceleration process was studied and improved.

The laser-plasma interaction was investigated with various non-invasive time-resolved optical methods. In particular, azimuthal Mega-Gauss magnetic fields which accompany the electron acceleration process were detected in-situ, providing insights into the acceleration process. Thereby, the acceleration process was observed with both high spatial and temporal resolution for the first time. Further online observation techniques warranted careful tuning of plasma parameters. Collimated high-energy electron beams with great stability and reproducibility were obtained and utilized to drive the subsequent undulator.

The described experiments serve as proof-of-principle. The present results are mainly limited by available electron energies. Novel target designs, able to reach GeV electron energies, promise straight realization of synchrotron radiation at shorter wavelengths in the near future. Further on, the ultra-short driving electron beam seems to be suited for operation in the FEL regime. In conjunction with the inherent synchronism with a short-pulse laser system, this promises unique high-resolution time-resolved pump-probe experiments to study matter. The setup presented in this thesis thus provides the basis for a new generation of laser-driven radiation sources.

Contents

1 Introduction

Research in physics is largely concerned with looking closely at things – or even into them – in order to understand certain phenomena. One very useful tool for this purpose are X-rays. Due to their short wavelengths, electron distributions on inter-atomic length scales [1] can be resolved. X-ray tubes were the first "light sources" for that purpose, and various techniques of X-ray diffraction were developed which allowed for measuring lattice parameters, Bravais lattices or electron and atom distribution in the unit cell [2]. However, for matter with a more complex structure than inorganic crystals like bio-molecules, more powerful X-ray sources were needed.

With the rise of accelerators and storage rings, basically intended for high-energy and particle physics, so-called first generation light sources were introduced [3]. Those utilized the bending magnet radiation of accelerator rings (which is an unavoidable energy loss) simply via gaps in the radiation shielding. The demand for increased brightness and enhanced control over the properties of the radiation led to facilities where electron beams are generated exclusively for the production of radiation. There, the particle beam is sent through "insertion devices" called undulators and wigglers. Intense and monochromatic radiation with tunable wavelength from mid-IR to X-ray range, arbitrary polarization and sub-nanosecond pulse duration is the result (second and third generation light sources) [4]. Another major step was undertaken with the development of free electron lasers (FEL), first in the IR and recently in the soft-X-ray range [5, 6] which produce spatially coherent radiation with further increased power. All of these light sources rely on conventional particle acceleration where the energy gain is limited by material breakdown to about $50\,\mathrm{MV/m}$. Hence, accelerators for $1\,\mathrm{GeV}$ final electron energy need at least $20\,\mathrm{m}$ acceleration length, for instance.

A new and groundbreaking approach of particle acceleration are laser-plasma accelerators [7]. A plasma cannot break down any further, hence it can sustain electric fields on the order of $\mathrm{TV/m}$. In turn, the acceleration length for $1\,\mathrm{GeV}$ is reduced to a millimeter scale. This acceleration regime became reality with the development of high-intensity short-pulse laser systems [8]. Laser pulses of so-called relativistic

intensity, $I \gtrsim 10^{18}\,\mathrm{W/cm^2}$, are inevitable for laser-plasma accelerators. In the last decade, laser-accelerated electron beams developed from uncollimated bunches with exponential, few-MeV-spectra to reproducible, collimated, stable beams with quasi-monoenergetic [9, 10, 11, 12], controllable [13], hundreds-of-MeV to GeV spectra [14, 15]. This rapid progress was on the one hand carried by further technological improvements of high-intensity laser systems [16] and stimulated by theoretical efforts and simulations [17, 18, 19], but on the other hand by the demand of tapping out the potential of much smaller and more efficient accelerators for applications [20]. Today, the field of laser-plasma accelerators is close to first applications, although progress in terms of complete and independent control of beam parameters like energy, bandwidth, pulse duration or bunch charge can still be made.
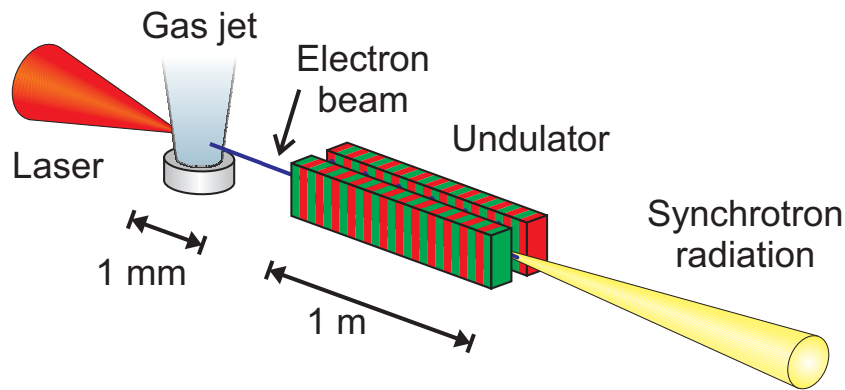
Figure 1.1: Overview of the novel experimental scheme to produce synchrotron radiation. A terawatt laser pulse is focused into a gas jet. By the laser-matter interaction at relativistic intensities, a bunch of relativistic electrons is generated within a distance on the order of one millimeter. The electron pulse traverses an undulator, and synchrotron radiation is produced. Electron beam diagnostics, radiation detection and further parts are not yet shown, please see Figures 4.1 and 5.1.

This thesis reports from experiments dedicated to explore the potential of laser-plasma accelerators for one specific application: the generation of synchrotron radiation from laser-produced electron beams as it is shown in Fig. 1.1. The laser-plasma accelerator is used in a similar manner as a conventional accelerator, effectively replacing the conventional one. The produced radiation was carefully detected and compared with simultaneously recorded electron spectra [21, 22].

Beforehand, the laser-plasma accelerator was developed from a previous stage of producing quasi-thermal spectra with a broad spatial distribution to a parameter regime closer to a conventional accelerator with monoenergetic and pencil-like beams by adapting and tuning the interaction parameters. During this optimization, various observation

techniques for online control were deployed. Passive imaging of the plasma enabled the measurement of Thomson-scattered light and wave-breaking radiation, which are indicators for strong laser-plasma interactions and electron acceleration. Probing techniques allowed for the detection of magnetic fields in the plasma which accompany electron acceleration. By that, the acceleration process was observed in-situ with high spatial and temporal resolution [23]. Electron beam profiles and energy spectra were recorded for online control and optimization of the interaction. The dependency of electron beam properties on various interaction parameters was studied.

The thesis is organized as follows. Chapter 2 introduces fundamental physical processes of the interaction of an intense laser pulse with plasma. Emphasis is put on the physical picture of electron acceleration. Effects which accompany and thereby indicate the acceleration of electrons by an intense laser are presented, too. Finally, a brief introduction to the production of synchrotron radiation is given. Chapter 3 describes experimental aspects of the studies. Diagnostic methods of the laser-plasma interaction and electron acceleration are presented as well as techniques for electron beam characterization and technical details of the undulator and the detection of synchrotron radiation. Chapter 4 presents results regarding the production of high-quality electron beams which was an essential prerequisite for the production of synchrotron radiation. From the laser-plasma diagnostics, insights into the acceleration process via magnetic fields are deduced and explained. Properties of the produced electron beams will be shown and compared to those of conventional accelerators. The production and detection of synchrotron radiation is depicted in detail in Chapter 5. The characteristics of the radiation, its discrimination from other possible sources and a comparison to conventional synchrotron sources are presented. Finally, Chapter 6 summarizes the results and discusses several issues how the present work can be continued in the future, addressing foreseeable improvements of laser-plasma accelerators and possible applications.

2 Theory of laser-plasma interaction and synchrotron radiation

This chapter will provide in its first 3 Sections an overview about the physics of electron acceleration from laser-plasma interactions. At first, the interplay of such intense laser pulses with single free electrons is discussed. Fundamental and optical properties of plasmas are revisited and extended for intense laser fields. Then in Sec. 2.2, different electron acceleration regimes are described. Sec. 2.3 completes the electron acceleration part with the description of effects which accompany electron acceleration and can thereby be used as indicators or to study the acceleration process. Lastly, the generation of synchrotron radiation with electron beams is outlined in Sec. 2.4.

2.1 Relativistic optics

2.1.1 Motion of a single electron

Any electromagnetic field acts on electrons via the Lorentz force

$$\mathbf{F}_{\mathrm{L}}(\mathbf{r}) = -e_0\big(\mathbf{E}(\mathbf{r}) + \dot{\mathbf{r}} \times \mathbf{B}(\mathbf{r})\big) \tag{2.1}$$

which depends upon the electric and magnetic fields $\mathbf{E}(\mathbf{r}, t)$ and $\mathbf{B}(\mathbf{r}, t)$ at the electron's actual place $\mathbf{r}(t)$ and the electron's velocity $\dot{\mathbf{r}}(t)$. Here, $e_0 \approx 1.602 \cdot 10^{-19}\,\mathrm{C}$ is the elementary charge. The motion of the electron is determined via Newton's law

$$\frac{\mathrm{d}\mathbf{p}}{\mathrm{d}t} = \mathbf{F}_{\mathrm{L}} \tag{2.2}$$

where $\mathbf{p}(t) = \gamma \, m_\mathrm{e} \, \dot{\mathbf{r}}(t)$ is the electron's momentum, $m_\mathrm{e} \approx 9.109 \cdot 10^{-31}\,\mathrm{kg}$ the electron rest mass and γ the relativistic factor

$$\gamma = \left(\sqrt{1 - \frac{\dot{\mathbf{r}}^2}{c^2}} \right)^{-1} . \tag{2.3}$$

The equation of motion may be solved for appropriate initial conditions $\mathbf{p}(t_0), \mathbf{r}(t_0)$.

In the case of an infinite plane, linearly in the x-z-plane polarized electromagnetic wave propagating in z-direction,

$$\mathbf{E}(\mathbf{r}, t) = \hat{\mathbf{x}} \, E_0 \, \sin(kz - \omega t) , \tag{2.4}$$

the motion may be described analytically [24, 25, 26]. For that, a normalization of momentum to $m_\mathrm{e} c$ and velocity to c is essential. Electric and magnetic field of the wave are expressed in terms of the vector potential $\mathbf{A}$ which is also normalized to

$$\mathbf{a} = \hat{\mathbf{x}} \, a = \hat{\mathbf{x}} \, \frac{e_0 \, A}{m_\mathrm{e} \, c} = \hat{\mathbf{x}} \, \frac{e_0 \, E}{m_\mathrm{e} \, \omega \, c} . \tag{2.5}$$

A related quantity is the amplitude of the normalized vector potential,

$$a_0 = \frac{e_0 \, E_0}{m_\mathrm{e} \, \omega \, c} \approx 0.85 \times \frac{\lambda}{\mu\mathrm{m}} \times \sqrt{\frac{I}{10^{18}\,\mathrm{W/cm^2}}} , \tag{2.6}$$

which is commonly referred to as normalized vector potential, too. Here, I is the intensity and λ the wavelength of the electromagnetic wave.

In the calculation for the solution of Eq. (2.2), a change of variable $\tau = t - z(t)/c$ is performed which not only describes the phase of the wave but is also the proper time t/γ of the electron [26]. Hence, for a cosine-like normalized vector potential $\mathbf{a} = \hat{\mathbf{x}} \, a = \hat{\mathbf{x}} \, a_0 \, \cos \omega \tau$, the parametric solution is

$$x(\tau) = \frac{c \, a_0}{\omega} \sin(\omega \tau) \tag{2.7a}$$

$$y(\tau) = 0 \tag{2.7b}$$

$$z(\tau) = \frac{c \, a_0^2}{4} \left(\tau + \frac{1}{2\omega} \sin(2\omega \tau) \right) . \tag{2.7c}$$

To the first order of the electric field amplitude, the electron oscillates with ω along the polarization of the electromagnetic wave, x. But to second order, there is an oscillation

with double frequency 2ω combined with a drift motion along the propagation direction of the wave, z. This part of the motion becomes significant for $a_0 \gtrsim 1$, which can be transformed to the so-called relativistic intensity given by Eq. (2.6) for a certain wavelength. For $\lambda \approx 800\,\text{nm}$, the threshold intensity is $I \approx 2 \cdot 10^{18}\,\text{W/cm}^2$.
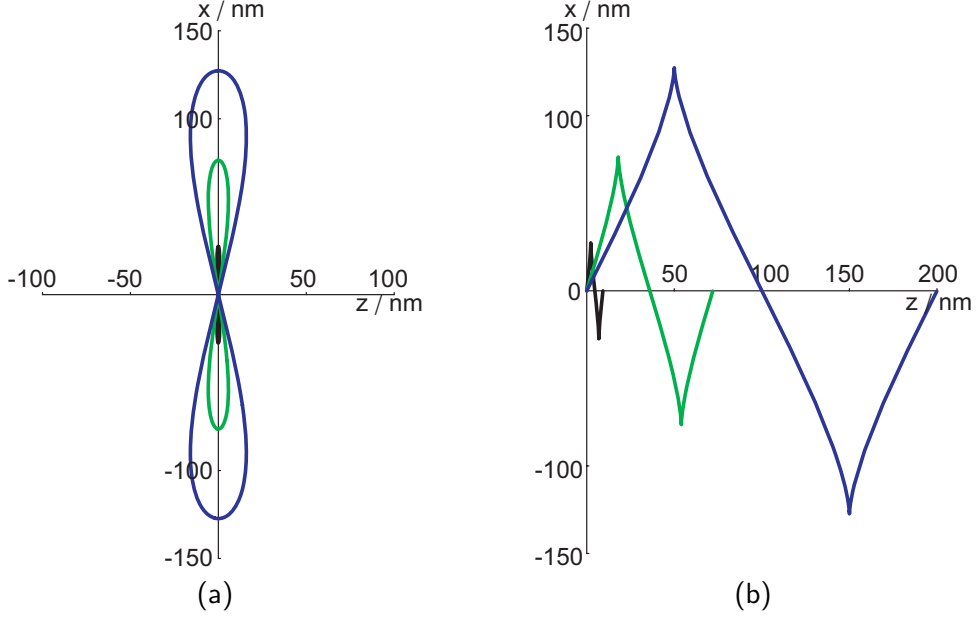
Figure 2.1: Electron trajectories in the average rest frame (a) and the laboratory frame (b) for $I = 10^{17}\,\text{W/cm}^2$ (black), $I = 0.8 \cdot 10^{18}\,\text{W/cm}^2$ (green) and $I = 2 \cdot 10^{18}\,\text{W/cm}^2$ (blue) at $\lambda = 800\,\text{nm}$ during one laser period experienced by the electron.

Figure 2.1 shows trajectories according to Eq. (2.7) for an electron in (a) a frame co-moving with the electron's drift velocity $c\,a_0^2/(4 + a_0^2)$ and (b) the lab frame, for three different intensities (or vector potential amplitudes a_0). The black curve is for $a_0 = 0.215$ which corresponds at $\lambda = 800\,\text{nm}$ to an intensity of $I = 10^{17}\,\text{W/cm}^2$. This is almost a classical linear oscillation. At higher intensities, $a_0 = 0.6$ (green) and $a_0 = 0.96$ (blue), the motion in the co-moving frame becomes a figure-of-8, and the drift motion along laser propagation is more pronounced. Note that for $a_0 \approx 1$ (blue curve), the drift distance during one laser oscillation in the electron's frame (τ) is already a quarter of the laser wavelength.

For focused laser pulses with transverse and longitudinal dimensions and if the oscillation is disregarded via temporally averaging, the Lorentz force transfers to the

ponderomotive force [27],

$$
\begin{aligned}
\left\langle \frac{d\mathbf{p}}{dt} \right\rangle &= -\frac{e_0^2}{2\,m_e\,\omega^2} \nabla \langle E^2 \rangle \\
&= -\frac{e_0^2}{2\,\varepsilon_0\,m_e\,\omega^2\,c} \nabla I(\mathbf{r}) = \mathbf{F}_{\mathrm{Pond}} \ ,
\end{aligned}
\tag{2.8}
$$

where ε_0 is the permittivity of free space.

For precision, Eq. (2.8) is the non-relativistic form of the ponderomotive force. Since the oscillation of electrons becomes relativistic for $a_0 \gtrsim 1$ (cf. (2.7a)), one could suppose to write $\langle \gamma \rangle m_e$ instead of m_e in Eq. (2.8). It was shown [28, 29] that this is the case for the assumptions that the intensity gradient is not too steep and the electrons initially non-relativistic. The relativistic ponderomotive force reads as

$$
\mathbf{F}_{\mathrm{Pond}} = -\frac{e_0^2}{2\,\varepsilon_0\,\langle \gamma \rangle\,m_e\,\omega^2\,c} \nabla I(\mathbf{r}) \ .
\tag{2.9}
$$

(a) (b)
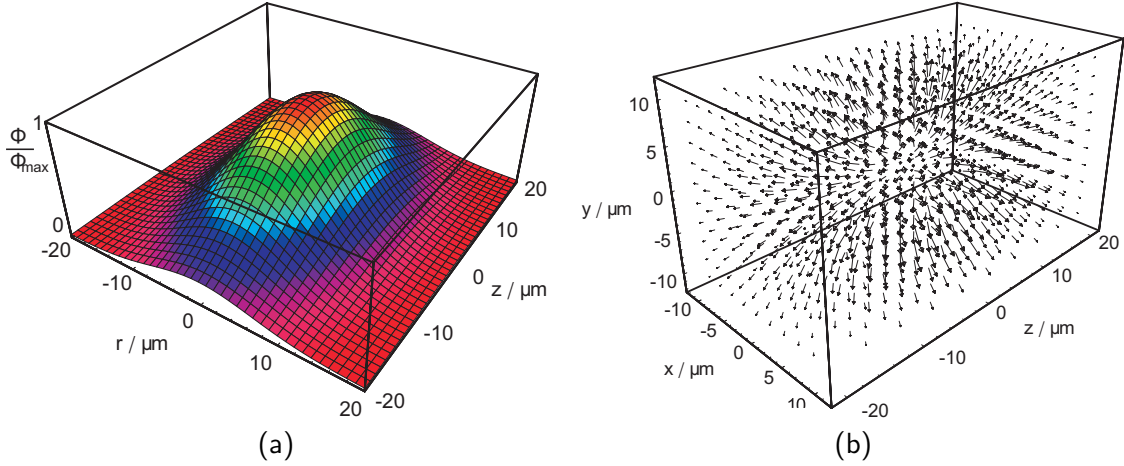
Figure 2.2: Ponderomotive potential (a) and ponderomotive force (b) for a laser pulse of $16\,\mu$m FWHM diameter and $87\,$fs FWHM pulse duration like the JETI laser had in the experiments (see Sec. 4.1.1). The potential is drawn for a cut through the axis and shows therefore the radial dependency.

Figure 2.2 shows the ponderomotive potential (a) and the ponderomotive force (b) as vector field of a laser with $16\,\mu$m FWHM diameter and $87\,$fs FWHM pulse duration. The ponderomotive potential is effectively the intensity envelope of the focused laser pulse. It is clearly visible that in this case the laser pulse is "cigar-shaped", it is longer than wide.

2.1.2 Fundamental plasma properties

A fully ionized plasma consists of quasi-free electrons and ions but no residual atoms. It is quasi-neutral but can easily react to electromagnetic fields. Ions are much heavier than electrons and respond much slower to electromagnetic fields. For timescales of optical radiation, ions are usually regarded as immobile, positively charged, homogeneous background.

A fundamental parameter for the description is the electron density

$$n_{\mathrm{e}} = \frac{\text{number of electrons}}{\text{unit volume}} \; . \tag{2.10}$$

In equilibrium, the electron density is homogeneous and equal to the ion charge density. If the steady-state is disturbed, electrons experience restoring forces from the ion background and start to oscillate around their average position. This is determined by a second fundamental parameter, the plasma frequency

$$\omega_{\mathrm{p}} = \sqrt{\frac{e_0^2 \, n_{\mathrm{e}}}{\varepsilon_0 \, m_{\mathrm{e}}}} \; . \tag{2.11}$$

As we will see later, the plasma frequency is usually smaller than the laser frequency. For sufficiently intense lasers, we must consider the relativistic case in which electrons oscillate with velocities v close to the speed of light c and hence experience a relativistic mass increase determined by the relativistic factor (2.3). Since the plasma oscillation is slow compared to the optical oscillation, we can use again the cycle-average of the relativistic factor, $\langle \gamma \rangle$. Hence, the plasma frequency is altered as follows:

$$\omega_{\mathrm{p,rel}} = \sqrt{\frac{e_0^2 \, n_{\mathrm{e}}}{\langle \gamma \rangle \, \varepsilon_0 \, m_{\mathrm{e}}}} \; . \tag{2.12}$$

In the following, the non-relativistic case $\langle \gamma \rangle = 1$ will be discussed. The consideration of relativistic effects is presented in Section 2.1.3.

The propagation of electromagnetic waves is determined by the dispersion relation

$$\omega^2 = \omega_{\mathrm{p}}^2 + k^2 c^2 \; . \tag{2.13}$$

Obviously, for frequencies $\omega \leq \omega_{\mathrm{p}}$, electromagnetic waves cannot propagate in the plasma. For a given plasma density, there is a certain wavelength where the plasma

becomes transparent for shorter wavelengths. Vice versa, for a given wavelength like the laser wavelength λ_L, there is the so-called critical density

$$n_\mathrm{c} = \frac{\varepsilon_0\, m_\mathrm{e}\, \omega_\mathrm{L}^2}{e_0^2} = \frac{\varepsilon_0\, m_\mathrm{e}\, 4\pi^2\, c^2}{e_0^2\, \lambda_\mathrm{L}^2} \tag{2.14}$$

which should not be exceeded if light propagation in the plasma is desired. Hence, plasmas with electron densities $n_\mathrm{e} < n_\mathrm{c}$ are called underdense plasmas. For $\lambda_\mathrm{L} \approx 800\,\mathrm{nm}$, the critical density is $n_\mathrm{c} \approx 1.7 \cdot 10^{21}\,\mathrm{cm}^{-3}$. Please note that the critical density depends in principle also on the laser intensity via the average oscillation velocity of electrons.

Due to the dispersion relation (2.13), the plasma has an index of refraction η given by

$$\eta = \sqrt{1 - \frac{\omega_\mathrm{p}^2}{\omega^2}} = \sqrt{1 - \frac{n_\mathrm{e}}{n_\mathrm{c}}} < 1 \;. \tag{2.15}$$

For plasma densities $n_\mathrm{e} << n_\mathrm{c}$ (like $n_\mathrm{e} = 10^{17} \ldots 10^{19}\,\mathrm{cm}^{-3} \Rightarrow n_\mathrm{c}/n_\mathrm{e} \approx 10^2 \ldots 10^4$), Eq. (2.15) may be approximated by

$$\eta \approx 1 - \frac{1}{2}\frac{n_\mathrm{e}}{n_\mathrm{c}} \;. \tag{2.16}$$

2.1.3 Effects at relativistic intensities

Up to now, the light propagation did not affect the index of refraction. In all formulas, the plasma frequency given by Eq. (2.11) had to be plugged in. However, as discussed as reasoning for Eq. (2.12), the plasma frequency and subsequently the critical density and the refractive index may change and then depend on the local intensity of the laser pulse. In advance of a discussion of those feedback effects, the relativistically correct index of refraction, phase velocity and group velocity are given [30]:

$$\eta \approx \underbrace{1 - \frac{1}{2}\frac{\omega_\mathrm{p}^2}{\omega_\mathrm{L}^2}}_{(2.16)} \left(1 + \underbrace{\frac{\delta n_\mathrm{e}}{n_\mathrm{e}}}_{A} - \underbrace{\frac{\langle a \rangle}{2}}_{B} - \underbrace{2\frac{\delta\omega_\mathrm{L}}{\omega_\mathrm{L}}}_{C}\right) \tag{2.17}$$

Term A represents a change of electron density, term B a variation of the plasma frequency due to relativistic mass increase and term C alterations of the laser frequency.

The phase velocity v_{ph} is given by

$$v_{\mathrm{ph}} = \frac{c}{\eta} \approx c\left(1 + \frac{1}{2}\frac{\omega_{\mathrm{p}}^2}{\omega_{\mathrm{L}}^2}\left(1 + \frac{\delta n_{\mathrm{e}}}{n_{\mathrm{e}}} - \frac{\langle a \rangle}{2} - 2\frac{\delta\omega_{\mathrm{L}}}{\omega_{\mathrm{L}}}\right)\right) \tag{2.18}$$

and the group velocity v_{gr} by [30, 31]

$$v_{\mathrm{gr}} \approx c\left(1 - \frac{1}{2}\frac{\omega_{\mathrm{p}}^2}{\omega_{\mathrm{L}}^2}\left(1 + \frac{\delta n_{\mathrm{e}}}{n_{\mathrm{e}}} - \frac{\langle a \rangle}{4} - 2\frac{\delta\omega_{\mathrm{L}}}{\omega_{\mathrm{L}}}\right)\right). \tag{2.19}$$

A variety of nonlinear effects can take place, which are, above all, entangled like a Gordian knot. The laser pulse may change locally the optical properties (2.18) and (2.19) via its intensity profile $\langle a \rangle$. The laser pulse envelope in turn may be altered by changes of the optical properties since some variations may be instantaneous and co-propagate with the laser pulse.

Transverse changes of the phase velocity lead to curvatures of wavefronts which result in self-focusing or defocusing. Longitudinal changes of v_{ph} lead to bunching of wavefronts which is called "photon acceleration" – the wavelength of the laser changes –, and longitudinal changes of v_{gr} lead to bunching of the pulse envelope, that is, self-modulation and pulse compression.

A very important effect for experiments is self-focusing since it counteracts diffraction and thereby prolongs the interaction length. Self-focusing may be accomplished as mentioned above via local changes of the plasma frequency caused by either relativistic mass increase of electrons via term B in Eq. (2.17). This is called relativistic self-focusing (RSF). The mass increase depends on the local intensity in the focus. For a Gaussian laser beam, the intensity on axis is higher, and therefore the index variation is higher on axis. The phase velocity on axis becomes slower than at outer regions at lower intensities, and a focusing index profile is generated.

Simultaneously, the ponderomotive force (2.9) pushes electrons away from regions of high intensity and reduces by that the electron density on axis. This also changes the refractive index transversely with a similar result. This is referred to as ponderomotive self-focusing (PSF). This density variation is then compensated by plasma oscillations as described for Eq. (2.12) and may therefore last longer than the laser pulse.

Regardless how the transverse variation of refractive index is achieved, a focusing index profile is generated. Counteracting to focusing is diffraction, and an equilibrium of the laser pulse waist between focusing and diffraction will be obtained. Self-focusing

occurs if the laser pulse power P exceeds [32]

$$P > P_{\mathrm{SF}} \approx \frac{n_{\mathrm{c}}}{n_{\mathrm{e}}} \cdot 16.2 \, \mathrm{GW} \; . \tag{2.20}$$

Then, the laser is focused to a diameter of the order of the plasma wavelength. For a laser power of $P = 10 \, \mathrm{TW}$ at a wavelength of $\lambda_{\mathrm{L}} \approx 800 \, \mathrm{nm}$, electron densities of $n_{\mathrm{e}} > 3 \cdot 10^{18} \, \mathrm{cm}^{-3}$ are required for self-focusing.

Most of those feedback effects increase the vector potential and become enhanced further. Generally speaking, laser-induced perturbations of the index of refraction modulate the laser pulse to such an extent that the perturbations grow. These are called modulation instabilities. However, instabilities with detrimental effects can occur too. Those are filamentation of the laser pulse due to coupling of defocusing index and transverse intensity modulations, and hosing.

2.2 Electron acceleration regimes

2.2.1 Laser Wakefield Acceleration

Laser wakefield acceleration (LWFA) is the standard picture of electron acceleration with plasma waves. It was so-to-speak "invented" by Tajima and Dawson [7] in 1979, at a time when lasers with sufficient intensity were not available. The model is quite simple:

- An intense laser pulse drives via the ponderomotive force a plasma wave, like a boat on the sea its wake.

- If electrons are injected at the top of the wake, they can gain energy from the space charge electric field of the wave in the same way a surfer from an ocean wave.

Plasma wave excitation

The ponderomotive force, Eq. (2.9), is directed anti-parallel to the intensity gradient (cf. Fig. 2.2). Hence, plasma electrons are pushed away from intense laser pulses. Since they are initially almost at rest but the laser pulse propagates almost with speed of light, they are at first pushed forward and/or sidewards. Ions stay at rest, and a density perturbation is formed. The variation of electron density depends mainly on the laser

intensity. Space charge forces start to pull the electrons back. The laser overtakes the electrons at some time which subsequently experience a kick backwards again from the ponderomotive force. The laser pulse has moved on, and the density depression becomes compensated. Electrons stream back to the depression. The time scale of streaming back is given by the plasma frequency which implicitly regards the inertia of electrons. The inertia, in turn, leads to an overshoot of the density. Electrons are again pushed away, but now by space charge effects. At this position, a plasma oscillation has been excited by the laser pulse. Since the laser pulse moves through the plasma and excites oscillations all along its path with a certain phase relation between each oscillation, the oscillations form a plasma wave. The phase velocity of this plasma wave equals the group velocity of the laser pulse v_{gr}. Thus, the plasma wavelength is

$$\lambda_{\mathrm{p}} = \frac{2\pi\, v_{\mathrm{gr}}}{\omega_{\mathrm{p}}} \approx \frac{2\pi\, c}{\omega_{\mathrm{p}}} \ . \tag{2.21}$$

For an electron density of $n_{\mathrm{e}} = 10^{18}\,\mathrm{cm}^{-3}$, the plasma period is $\lambda_{\mathrm{p}} \approx 33\,\mu\mathrm{m}$, and it scales with $(n_{\mathrm{e}})^{-1/2}$.

The effectiveness of the plasma wave excitation depends on the laser intensity but also on the pulse length. For a resonant excitation, the laser pulse length, given by the FWHM pulse duration τ_{L}, must fit in the first half-period of the plasma wave [7], which results in

$$\omega_{\mathrm{p}} \cdot \tau_{\mathrm{L}} = \pi \ . \tag{2.22}$$

Equation (2.22) is a delicate condition, as it relates the laser pulse duration to the electron density via Eq. (2.11). For instance, if a 10 TW laser operates at $\lambda_{\mathrm{L}} \approx 800\,\mathrm{nm}$, a minimum density of $n_{\mathrm{e}} \approx 3 \cdot 10^{18}\,\mathrm{cm}^{-3}$ for self-focusing was calculated in Sec. 2.1.3. For such densities, the pulse duration must by shorter than $\tau_{\mathrm{L}} \approx 30\,\mathrm{fs}$ which is a pulse with about 12 cycles. This is already close to the limit of validity of several previous expressions like Eq. (2.9).

Conversely, for a given laser system with a pulse duration of say $\tau_{\mathrm{L}} \approx 100\,\mathrm{fs}$, the electron density must be $n_{\mathrm{e}} \approx 3 \cdot 10^{17}\,\mathrm{cm}^{-3}$ in order to fulfill the LWFA condition (2.22). This density is quite low and adverse for effects like self-focusing or a high wave-breaking limit which is presented in the following.

Furthermore it must be noted that the following description of the LWFA regime considers plane plasma waves which corresponds to a 1-dimensional (1D) approach where only the propagation direction is of interest. This simplifies the physical picture since transverse dependencies can be disregarded, e.g. the plasma wave amplitude varies with

the radial distance due to the transverse intensity profile of the laser pulse. However, those transverse effects play an important role in reality and will be regarded later in Sec. 2.2.3.

Nonlinear plasma waves

Up to now (Sec. 2.1.3), only minute variations of electron density were considered, leading to small amplitude electric fields. For efficient particle acceleration, much stronger space charge electric fields are required.

Let's now assume the variation of electron density to be massive, $\frac{\delta n_e}{n_e} \sim 1$. This will lead to ultra-high space charge fields in the plasma. Hence, inside the plasma wave the electron velocity becomes relativistic and alters the plasma frequency during the oscillation. This is now different from Eq. (2.12) since the mass increase inherently changes during the plasma oscillation and cannot be taken as average over a faster optical oscillation. Therefore, the former sinusoidal wave becomes nonlinear, as shown in Figure 2.3. Electrons become bunched at some kind of spikes. Hence, due to space-charge effects, strong electric fields perpendicularly to the wave fronts are present. These electric fields are harnessed for particle acceleration as we will soon see.
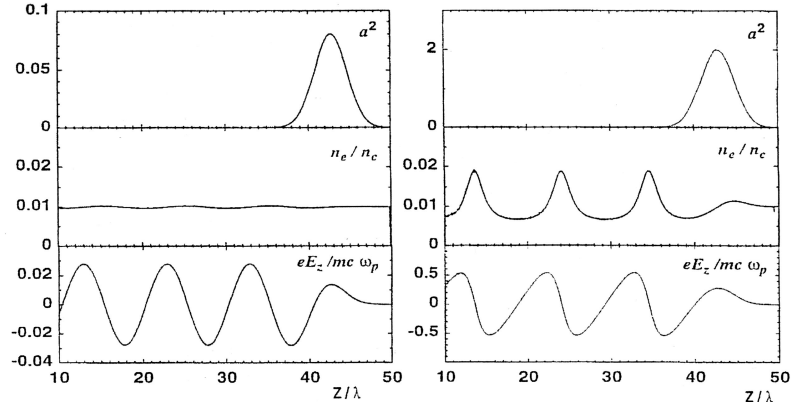
Figure 2.3: Laser pulse intensity envelope a^2, electron density modulation and longitudinal electric field for a weakly relativistic laser pulse with $a_0 = 0.2$ (left) and a relativistically intense pulse (right, $a_0 = 1$). The electron density modulation (plasma wave) is given in units of the critical density and scaled equally for both cases for comparison. This, however, prevents the comparison of the shapes: The plasma wave for low intensity is approximately sine-shaped, similar to the electric field. Taken from [33].

Wave-breaking and injection

As prerequisite for acceleration, electrons have to be injected in such an electric field. That is, they must have at least the phase velocity of the wave in order to be initially at rest in a frame co-moving with the wave. Since the phase velocity of the wake is the group velocity of the laser pulse which is close to the speed of light, electrons must start with significant velocities. This can be accomplished from an external electron gun, from a beatwave [17, 13] or via wave-breaking. However, injection should not occur at arbitrary phase. Electrons shall be injected at a minimum of the electric field (due to their negative charge), that is, a little in front of an electron density spike.

Wave-breaking happens when the particle velocities inside the wave reach the phase velocity of the wave. Particles slip out of the wave, similar to whitecaps at the ocean's surge. So it happens at the right position of the wake and with the correct velocity for injection. For this reasons, wave-breaking is called self-trapping of electrons. Furthermore, wave-breaking requires large-amplitude nonlinear plasma waves, which in turn are ideal for efficient particle acceleration.

Assuming a cold plasma with linear, non-relativistic waves, the wave-breaking limit can be expressed as [34]

$$E_{\mathrm{wb}} = \frac{c\,m_{\mathrm{e}}\,\omega_{\mathrm{p}}}{e_0} \;.$$ (2.23)

If the relativistic oscillation of the plasma electrons is included (with further constraints such as plane plasma waves [17]), this limit is shifted to

$$E_{\mathrm{wb,rel}} = \sqrt{2(\gamma_{\mathrm{p}} - 1)}E_{\mathrm{wb}}$$ (2.24)

where γ_{p} is the relativistic factor related to the phase velocity of the wake and may be approximated to $\gamma_{\mathrm{p}} \approx \omega_{\mathrm{L}}/\omega_{\mathrm{p}} = \sqrt{n_{\mathrm{c}}/n_{\mathrm{e}}}$. For example, for a plasma density of $n_{\mathrm{e}} = 10^{18}\,\mathrm{cm}^{-3}$, the cold plasma, non-relativistic wave-breaking threshold is $E_{\mathrm{wb}} \approx 100\,\mathrm{GV/m}$, and with relativistic effects $E_{\mathrm{wb,rel}} \approx 1\,\mathrm{TV/m}$. This shows clearly the advantage of plasma-based acceleration schemes against RF accelerators. The maximum accelerating fields exceed the ones of the best conventional accelerators ($\approx 10-40\,\mathrm{MV/m}$ [35]) by more than 4 orders of magnitude.

Those ultra-high electric fields are attained via the plasma-wave excitation of the ponderomotive force. The longitudinal electric field amplitude of the wake depends

mainly on the laser intensity a_0^2 and may be expressed by [17, 26, 36, 37]

$$E_{\mathrm{p}} \approx \frac{a_0^2/2}{\sqrt{1 + a_0^2/2}} \, c \, m_{\mathrm{e}} \, \omega_{\mathrm{p}}/e_0 = \frac{a_0^2/2}{\sqrt{1 + a_0^2/2}} \, E_{\mathrm{wb}} \ . \tag{2.25}$$

Hence, in order to reach the wave-breaking limit, $E_{\mathrm{p}} \geq E_{\mathrm{wb,rel}}$, the laser pulse amplitude must significantly exceed the relativistic limit, $a_0^2 >> 1$:

$$\underbrace{\frac{a_0^2/2}{\sqrt{1 + a_0^2/2}}}_{\approx a_0/\sqrt{2}} \geq \sqrt{2(\sqrt{n_{\mathrm{c}}/n_{\mathrm{e}}} - 1)} \tag{2.26}$$

In addition it must be mentioned that wave-breaking sets also a limit of the plasma wave amplitude or the electric fields inside the wave, similar to the breakdown limit in RF accelerators. Furthermore, injection of electrons reduces the longitudinal electric fields and inhibits further wave-breaking. This is called beam loading [38], which leads to an inherent control of the charge of the accelerated electron beam. Furthermore, wave-breaking consumes laser energy, heats the plasma and interrupts the modulation instabilities.

Energy gain considerations

So far, with short powerful lasers, large-amplitude plasma waves can be excited and electrons can be correctly injected via wave-breaking. The wave-breaking also sets the upper limit of field strength the plasma can sustain. Hence it is the upper limit of the accelerating field. But how long can electrons be accelerated, since focused laser pulses are used what means that energy is coupled in only once and is maintained at high intensity for a limited length? Or, more crucial, can the much higher accelerating electric fields in the plasma be sufficiently harnessed that electron energies can compete with conventionally accelerated electrons?

Just to give the idea of limitations, in the following the case of plane waves (1D) and weakly relativistic excitation is presented. At first, if we assume infinite interaction, a "pump depletion" will occur since only finite energy is available from the laser pulse. The maximum length can be estimated by equating the initial laser pulse energy to the energy left behind in the plasma wave and is [17, 26]

$$L_{\mathrm{pd}} \sim \frac{n_{\mathrm{c}}}{n_{\mathrm{e}}} \frac{\lambda_{\mathrm{p}}}{a_0^2} \ . \tag{2.27}$$

A further limit is the dephasing limit. Electrons are injected at the top of the wave and are accelerated. Even though they move relativistically and therefore most of the energy gain is relativistic mass increase, they also become faster. Thus, they move faster than the wave and may reach its bottom. If they move forward any further with respect to the wave, they experience a deceleration. In a frame co-moving with the wave, electrons may move half a plasma wavelength at most. Approximating the electron's velocity with c, assuming the weakly relativistic case and considering the plasma wave phase velocity to equal the laser pulse's group velocity, the dephasing length reads as

$$L_{\mathrm{d}} \sim \frac{n_{\mathrm{c}}}{n_{\mathrm{e}}} \lambda_{\mathrm{p}} \ . \tag{2.28}$$

The maximum energy gain is ruled by the dephasing length and the maximum electric field and may be estimated to E_{p} to

$$\gamma_{\max} \sim a_0^2 \frac{n_{\mathrm{c}}}{n_{\mathrm{e}}} \ . \tag{2.29}$$

Eq. (2.29) is indeed the maximum achievable energy. Firstly, the acceleration length has to be long enough. In order to reach the LWFA regime, the laser pulse must be either quite short or the electron density has to be comparatively low. The question is, whether the pulse power is high enough in order to reach the self-focusing limit (2.20). If not, the laser pulse reaches its high intensity only along the Rayleigh length of the focusing optic. This may be overcome by an external preparation of the plasma in terms of creating a parabolic transverse density gradient which guides the laser pulse [10, 14].

Secondly, the actual distribution of energies, i.e. the electron energy spectrum, depends on the injection process and the actual accelerating fields for different electrons. For instance, it depends on how long electrons can be accelerated which in turn depends on the duration of injection. If this is just a short instance, those few electrons will be accelerated rather uniform. Furthermore, the accelerating field may vary in transverse direction since the laser pulse is focused. Thus, electrons injected at different places experience different accelerating fields which ends up in different energies.

Finally, the expressions above are valid for a regime of linear plasma waves and thereby for low intensities, $a_0 \ll 1$. They can be extended to high intensities [17, 26] but still rely on assumptions and approximations. Another approach relies on computer simulations. The Bubble regime introduced in Sec. 2.2.3 will provide a set of relations which are derived from particle-in-cell (PIC) simulations. Those simulations include 3D-effects and arbitrary intensities.

Example

In order to depict the influence of the several parameters, let's consider the following example. A Ti:Sapphire laser system shall be used for electron acceleration. The wavelength is $\lambda_L = 800\,\text{nm}$ and the pulse duration $\tau_L = 100\,\text{fs}$. The laser pulse energy may be chosen freely as well as the focusing optic.

1. Via Equation (2.14), the critical density is $n_c \approx 1.7 \cdot 10^{21}\,\text{cm}^{-3}$ and via Eq. (2.22) the electron density for resonant plasma wave excitation $n_e \approx 3.1 \cdot 10^{17}\,\text{cm}^{-3}$. The ratio is $n_c/n_e \approx 5 \cdot 10^3$ and the plasma period $\lambda_p \approx 60\,\mu\text{m}$.

2. Now, the wave-breaking limit may be calculated from Equations (2.23) and (2.24) to $E_{wb} \approx 50\,\text{GV/m}$, or under consideration of relativistic effects to $E_{wb,rel} \approx 600\,\text{GV/m}$, respectively.

3. From Equation (2.20) follows that if the laser pulse power exceeds $P_L \approx 90\,\text{TW}$, self-focusing occurs. This in turn requires a laser pulse energy of $E_L \gtrsim 9\,\text{J}$. Such laser pulse energy may be achieved nowadays but still demands careful operation of the laser system.

4. The maximum acceleration length is given by the dephasing length which is at those high intensities on the order of 10 cm.

5. In order to reach wave-breaking and self-trapping of electrons, the normalized vector potential has to be larger than $a_0 \gtrsim 16.7$, according to Eq. (2.26). From Eq. (2.6), the laser intensity must reach a value $I_L \approx 6 \cdot 10^{20}\,\text{W/cm}^2$. Hereby, pulse energy and spot size are coupled. If the energy suffices for self-focusing, the waist is on the order of the plasma wavelength. Hence, about one kilojoule of laser energy is necessary.

6. If we now consider a laser slightly below the self-focusing power limit (e.g. 8 J), it must be focused to a waist of $w_L \approx 2\,\mu\text{m}$. The maximum acceleration length is determined by the Rayleigh length $z_R = \pi w_L^2/\lambda_L \approx 15\,\mu\text{m}$.

7. In this case, the maximum output electron energy is about $E_{max} \approx 10\,\text{MeV}$.

Discussion

The LWFA regime depicts very descriptively the underlying physics. However, it is rather a picture than a precise model. The limitations of analytical descriptions of

the nonlinear processes were already mentioned as well as the use of computer simulations. The latter is nowadays a widely used standard method. The Bubble regime (see Sec. 2.2.3) was discovered and studied with such PIC simulations and is in principle the successor of the LWFA regime.

A second issue which should be addressed emerges from a practical point. Common CPA multi-terawatt laser systems produce pulses longer than 25 fs with energies up to a few Joules. They may be focused to spot diameters of a few microns in order to obtain the highest possible intensities. Hence, the laser pulse is in the focus rather cigar-shaped (cf. Fig. 2.2) and transverse plasma dynamics play a significant role. It would be better to use laser pulses where the length is equal or shorter than the diameter. But then, in order to maintain the intensity, the waist and consequently the pulse energy would have to be increased.

Furthermore, pulses longer than 25 fs require for resonant plasma wave excitation plasma densities thinner than $10^{18}\,\mathrm{cm}^{-3}$, what is in principle beneficial for high electron energies (cf. Eq. (2.29)). But this just relies on a low wave-breaking limit combined with a long dephasing length. In order to exploit the maximum energy, the interaction length has to be long enough. This is also experimentally difficult to realize. Long Rayleigh lengths require long focal lengths. The waist would be increased further which must again be compensated with increased pulse energy.

The practical issues can be easily overcome with higher gas densities. Self-modulation shortens the laser pulse and self-focusing prolongs the interaction length. This is discussed in the following.

2.2.2 Self-Modulated Laser Wakefield Acceleration

In the self-modulated LWFA (SM-LWFA) regime, a long laser pulse is considered, not fulfilling condition (2.22). In this case, the laser pulse still excites a plasma wave. But now, the laser pulse overlaps with the excited wave which represents a co-moving density perturbation. This density modulation affects the laser pulse via Eqs. (2.17), (2.18) and (2.19). Parts of the laser pulse at positions with reduced electron density propagate faster than parts at positions with increased density. This leads to bunching of the laser pulse, the laser pulse envelope becomes modulated by the plasma wavelength. The modulated envelope can excite the plasma wave more resonantly. The density modulation grows, which in turn amplifies the laser pulse modulation. Thus, the pulse splits into pulselets, each separated by the plasma wavelength and fulfilling the LWFA condition. Then, the modulated pulse may drive a plasma wave resonantly like in the

LWFA regime. The effectiveness of that splitting depends on numerous parameters. In general it is necessary that the pulse power suffices for self-focusing, see Eq. (2.20).

In principle, the SM-LWFA regime is easier to implement than the LWFA regime and may produce higher electron energies for a given laser system[17]. A dense plasma may be used and a relatively long laser pulse which may be tightly focused. The interaction length is prolonged by the laser pulse itself via self-focusing, and higher longitudinal electric fields are used for acceleration. However, the whole process is strongly nonlinear and therefore difficult to control. Mostly, exponential electron spectra are obtained [39] due to plasma heating from various instabilities and altered injection conditions for hot plasmas.

2.2.3 Bubble Acceleration

The Bubble acceleration was discovered via computer simulations carried out by Pukhov and Meyer-ter-Vehn [19]. The simulations include 3D-effects of the plasma wave formation like a tightly focused laser pulse or large transverse oscillations of the electrons. This regime uses intense ($a_0 > 1$) but pancake-shaped very short ($\tau_L < 7\,\mathrm{fs}$) laser pulses which propagate through dense plasma ($n_e \sim 10^{19}\mathrm{cm}^{-3}$). The simulations show the formation of a bubble-like void behind the laser pulse with strong electric fields pointing toward the bubble's center. Electrons are injected and concentrate at a small position. This leads to a uniform acceleration and hence monoenergetic spectra. From simulations with longer pulses, several bubbles may be created [11]. Insofar, a strict discrimination to LWFA is difficult. An intermediate regime is sometimes called "Forced Laser Wakefield Acceleration" [40, 41] which shows already the reduction of the plasma wave to a single oscillation and collimated electron beams, but still broad exponential spectra are obtained.

Extended numerical studies [42, 43, 44] revealed the following properties of the Bubble regime under the condition that the laser beam waist matches the plasma wavelength and is significantly larger than the pulse length.

- A few cavities free from background electrons are formed instead of a periodic wave.

- Self-Trapping: A very dense bunch of electrons is self-generated.

- Self-Focusing: In a homogeneous plasma, the laser pulse and the bubble propagate many Rayleigh lengths.

- Scalability: A similarity parameter $\mathcal{S} = n_{\mathrm{e}}/(a_0 n_{\mathrm{c}})$ was found. For constant $\mathcal{S}$, i.e. increasing the intensity and density, the bubble behaves the same.

- Universality: Simulations were executed covering a wide parameter range. It seems that the bubble formation is an attractor.

The last issue is supported by several experiments [45, 46]. To date, no experiment has been carried out with laser systems which access the Bubble regime directly. Mostly the laser pulses are longer ($\tau_{\mathrm{L}} > 20\,\mathrm{fs}$), or few-cycle systems have not the required pulse energy. In the experiments reported by Hidding *et al.* [46], the JETI laser was operated under conditions of tight focusing where the spot size was a few microns but the initial pulse length still 30 microns. The initial normalized vector potential was $a_0 \approx 5$. Under those conditions, the self-modulated wakefield or direct laser acceleration regime can be expected. However, monoenergetic spectra were observed. Simulations carried out by Michael Geissler for the actual experimental conditions show a strong self-modulation of the laser pulse which ends up in the formation of a few-cycle pulselet driving a single bubble. Similar simulation results are found for several other experiments, but may differ regarding the number of bubbles and the general manifestation of nonlinear wakefield as bubble-like structures [40, 11].

From numerical studies, simple analytic expressions for the electron bunch were derived. The electron energy is determined by

$$\gamma_{\mathrm{max}} \approx 0.65 \sqrt{\frac{P}{P_{\mathrm{rel}}}} \frac{c\,\tau_{\mathrm{L}}}{\lambda_{\mathrm{L}}} \ . \tag{2.30}$$

Here, $P_{\mathrm{rel}} \approx 8.5\,\mathrm{GW}$ is the relativistic power unit. The bunch charge is

$$N \approx 0.28 \frac{\lambda_{\mathrm{L}}}{r_{\mathrm{e}}} \sqrt{\frac{P}{P_{\mathrm{rel}}}} \ , \tag{2.31}$$

where $r_{\mathrm{e}} = e^2/(4\pi\varepsilon_0 m_{\mathrm{e}} c^2) \approx 2.8\,\mathrm{fm}$ is the classical electron radius. For a laser with $P = 5\,\mathrm{TW}$, $\lambda_{\mathrm{L}} = 800\,\mathrm{nm}$ and $\tau_{\mathrm{L}} = 80\,\mathrm{fs}$ the maximum electron energy is 240 MeV and the bunch charge 0.3 nC.

2.2.4 Direct Laser Acceleration

Besides acceleration mechanisms which rely on electric fields of plasma waves, there is also a direct mechanism of energy transfer from the laser pulse to particles. Direct laser acceleration (DLA) was first proposed by Pukhov [18] and subsequently observed by

Gahn *et al.* [47]. The ponderomotive force of a very intense laser pulse expels electrons from the laser axis and creates a positively charged channel. The ponderomotive force also leads to particle velocities in laser propagation direction. This forward current generates a magnetic field. This magnetic field superimposes with the electric field of the ion channel. Both build up a potential well. Electrons with an additional initial transverse velocity may oscillate therein with a betatron frequency. If those oscillations are in phase with the Doppler-shifted electric field of the laser, a direct energy transfer from the laser's electric field to electrons is possible, which coined the name of that complex mechanism. The obtained spectra show a quasi-thermal exponential decay which is in agreement with simulations. It was found that the effective electron temperature depends on the laser intensity and scales like $T_{\mathrm{eff}} \approx 1.5\,\mathrm{MeV} \cdot \sqrt{I_{\mathrm{L}}/10^{18}\,\mathrm{W/cm^2}}$.

2.3 Concomitant effects of electron acceleration

2.3.1 Nonlinear Thomson scattering

Thomson scattering is scattering of light from free electrons. In the linear regime, electrons just oscillate linearly via the Lorentz force (2.1) (cf. Eq. (2.7) for low intensities where $a_0^2 << a_0$). The electron builds an oscillating dipole and radiates. Hence, incident and scattered frequency and polarization are equal.

Nonlinear Thomson scattering [48] is similar, but now at relativistic intensities where the electron's motion is more complex. Eq. (2.7c) and Fig. 2.1 show that the electron oscillates with double excitation frequency and along laser propagation direction. Furthermore, the relativistic drift motion and a dependency on the initial phase [25, 49] lead spectral broadening of the scattered light. A certain harmonic number emits a wide frequency interval which overlaps with other harmonics.

Thomson-scattered light is emitted from the plasma at regions of relativistic intensity. This is predominantly the region of self-focusing where the laser pulse propagates collimated over long distance. This is called plasma channel or relativistic channel. At not too high intensities, Thomson-scattering occurs at discrete harmonics close to the laser frequency and its harmonics. Thereby the plasma channel can be imaged onto a camera.

2.3.2 Wave-breaking radiation

If the laser intensity is high enough for wave-breaking, electrons are injected into the wake and become accelerated, which is a quite violent process. By that, electrons radiate broadband emission. This was described first by Thomas *et al.* [50]. Experiments were carried out with a laser system similar to the JETI. Besides Thomson scattered light at the laser frequency and second harmonic originating from the relativistic channel, they observed in laser propagation direction first a gap without any emission and then after a certain distance of about $100\,\mu$m a point-like broadband emission, which was correlated with electron beam generation. Thus, this is an indicator for electron acceleration which is easy to identify.

2.3.3 Azimuthal magnetic fields

Origins for magnetic fields

Azimuthal magnetic fields, i.e. magnetic fields which have a curl ($\nabla \times \mathbf{B} \neq 0$), may be generated by real currents $\mathbf{j}$ and displacement currents $\dot{\mathbf{D}}$, as Maxwell's equations state. The strong interaction of the laser with plasma electrons can lead to both kinds. Real electron currents may be currents of trapped electrons, which is the initial state of the later electron beam, but also wake currents. Those are currents which take place at the leading edge of the laser pulse, where electrons are pushed away by the ponderomotive force and stream around the laser pulse or the bubble.

The displacement currents arise from temporally varying electric fields and are therefore "virtual" currents. Strong electric fields are present in wakefield structures or a plasma bubble and move with speed of light. At a fixed position in the plasma, the electric field changes with time which corresponds to a displacement current.

Faraday rotation

Magnetic fields can change the polarization of light by both the Faraday effect and the Cotton-Mouton effect [51]. Figure 2.4 depicts how a probe beam passes through a plasma where azimuthal magnetic fields are present.

The Faraday effect is induced by magnetic field components parallel to the probe beam propagation, $B_\parallel$. The rotation of the polarization plane $\mathrm{d}\phi$ while propagating a path $\mathrm{d}s$ depends on both the magnetic field $\mathbf{B}(\mathbf{r})$ and electron density $n_\mathrm{e}(\mathbf{r})$ along the path and is sensitive to the orientation of the probe beam propagation direction (given
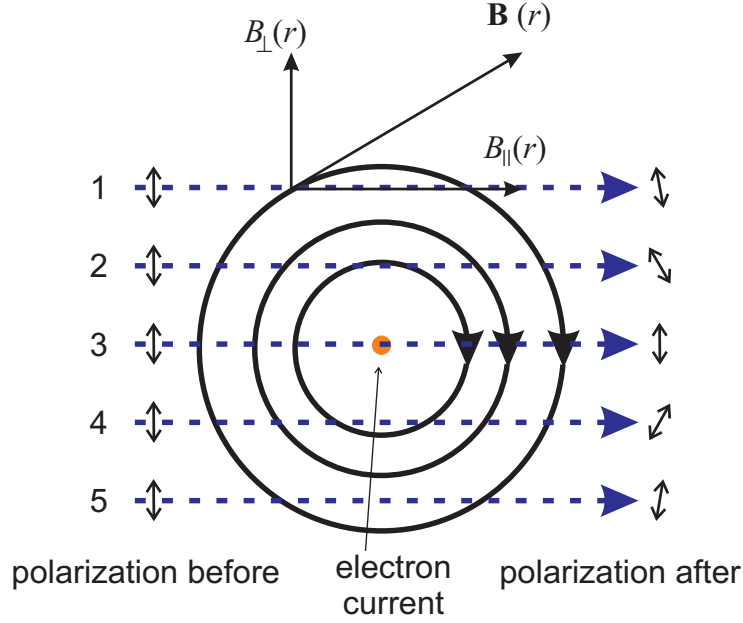
Figure 2.4: Scheme of the Faraday rotation in a plasma.

by its wave vector $\mathbf{k}$) with respect to the magnetic field. The total angle of rotation after propagation through the plasma is given by [51]

$$\phi_{\text{rot}} = \frac{e_0}{2\,c\,m_{\text{e}}} \int \frac{n_{\text{e}}(\mathbf{r})}{n_{\text{c}}} \mathbf{B}(\mathbf{r}) \cdot \frac{\mathbf{k}}{|\mathbf{k}|} \, \mathrm{d}s \, . \tag{2.32}$$

The dependence on the local electron density arises from the fact that the amount of magnetically induced birefringence depends on the refractive index which in turn depends on the plasma density as given by Eq. (2.15).

The Cotton-Mouton effect arises from components of the magnetic field which are perpendicular to the probe beam wave vector, $B_\perp$, and induces an ellipticity of the probe beam.

Figure 2.4 shows azimuthal magnetic fields induced by a current. The fields show circular symmetry. Further, a homogeneous plasma is assumed.

Probe beam ray 1 propagates through the outer regions where the fields are weak and becomes only slightly rotated. Ray 5 propagates through the same field strengths, but the effective field component is inversely oriented and therefore the sign of rotation is inverse to ray 1. Ray 2 and 4 propagate through stronger field regions and experience more rotation. The central ray 3 propagates through the highest fields, but there is always only a perpendicular component of the magnetic field present and no rotation is

accumulated. It can be further seen that the perpendicular magnetic fields are oriented upwards in the first half of the passage and downwards in the second half but with same strength. Therefore, the integral of the perpendicular field component is zero and the Cotton-Mouton effect suppressed.

2.4 Principles of synchrotron radiation

Synchrotron radiation, in a general sense, is electromagnetic radiation produced by charged particles deflected off magnetic fields. Similar is bremsstrahlung, which is produced by deflection in electric fields.

However, we will refer by the term "synchrotron radiation" to electromagnetic radiation which is produced by electrons traversing an undulator or a wiggler, without significant interaction between radiation and electron beam. By that, we distinguish this term from the bending magnet radiation, which historically was produced by synchrotrons and therefore could be understood as synchrotron radiation, too. Furthermore, we want to exclude free electron laser radiation from that term.

An undulator or a wiggler is an highly engineered assembly of permanent magnets or coils which produces a periodic transverse magnetic field. Highly relativistic electrons are injected, trail a sinusoidal trace via the Lorentz force and subsequently emit radiation. Due to the relativistic motion, a cm-scaled period of the magnetic field is translated to nm-scale radiation and a nicely collimated beam.

2.4.1 Theory for single electrons

Motion in a periodic magnetic field

Let's assume a periodic magnetic field with amplitude B_0 and period length λ_u which is polarized in the x-z-plane:

$$\mathbf{B}_u(z) = \hat{\mathbf{x}}\, B_0\, \sin(2\pi\, z/\lambda_u)\ . \tag{2.33}$$

The effect of finite number of periods N_{u} will be discussed later, edge effects at injection and exit of electrons are disregarded. A free relativistic electron with energy $E = \gamma\, m_{\mathrm{e}}\, c^2$ which would in absence of the field propagate in the z-direction,

$$z(t) = \beta\, c\, t\ , \tag{2.34}$$

with normalized velocity $\beta = v/c = \sqrt{1 - 1/\gamma^2}$, is now injected. The motion in the magnetic field $\mathbf{B}_u(z)$ is determined via the Lorentz force (Eq. (2.1)) which reads in that particular case as

$$\gamma \, m_\mathrm{e} \, \ddot{\mathbf{r}}(t) = \mathbf{F}_\mathrm{L}^u = -e_0 \, B_0 \, \sin(2\pi \, z/\lambda_u) \, \dot{\mathbf{r}}(t) \times \hat{\mathbf{x}} \; . \tag{2.35}$$

The electron's motion is somehow similar to nonlinear Thomson scattering, Eq. (2.7). The integration my be approximated in a perturbative way. In first order, the oscillation along y is calculated, assuming that the changes of the z-velocity are negligible for the time-independent trajectory,

$$y(z) \approx \underbrace{\frac{\lambda_\mathrm{u} \, e_0 \, B_0}{2\pi \, m_\mathrm{e} \, c}}_{K} \frac{\lambda_\mathrm{u}}{2\pi \, \gamma} \sin\left(\frac{2\pi \, z}{\lambda_\mathrm{u}}\right) . \tag{2.36}$$

K is the dimensionless undulator parameter. The maximum angle of this sine trajectory with respect to the initial direction is

$$\Theta_\mathrm{u} = \frac{K}{\gamma} \; . \tag{2.37}$$

Now to second order it must be considered that the magnetic field conserves the velocity, hence a transverse oscillation will affect changes in the longitudinal velocity. Under the assumptions that the transverse velocity is much smaller than c and the kinetic energy is highly relativistic, the average longitudinal velocity is

$$\bar{\dot{z}} \approx c \left[1 - \frac{1}{2\,\gamma}\left(1 + \frac{K^2}{2}\right) \right] \tag{2.38}$$

and in an co-moving average rest frame the transverse and longitudinal oscillations

$$y^*(t) = \frac{K}{k_\mathrm{u}\gamma} \sin(\omega_\mathrm{u} t) \tag{2.39a}$$

$$z^*(t) = \frac{K^2}{8\,k_\mathrm{u}\gamma^2} \sin(2\,\omega_\mathrm{u} t) \; . \tag{2.39b}$$

Here, $k_\mathrm{u} = 2\pi/\lambda_\mathrm{u}$ is the undulator wavenumber and $\omega_\mathrm{u} = \beta \, c \, k_\mathrm{u}$ the oscillation frequency. The average velocity is reduced from the initial value of βc by a fraction of $K^2/2$. In the co-moving frame, the electrons perform a figure-of-8 motion similar to Fig. 2.1 (a). Hence, besides the fundamental oscillation in the transverse direction, there will be

always a second harmonic. For strong deflection K, the transverse velocity increases and higher orders of the perturbation must be regarded. Then, further harmonics will be significant.

Emitted radiation

In the average rest frame, dipole radiation is emitted with fundamental frequency ω_u according to Eqs. (2.39). The radiation, however, is detected in the lab frame, and therefore a Lorentz transformation has to be carried out. By that, the usually cm-scaled wavelength is transformed to the sub-micrometer range, and an angular dependency comes into play with the angle of observation θ_o with respect to the initial electron propagation direction z. The observed wavelength is [3]

$$\lambda = \frac{\lambda_\mathrm{u}}{2\,\gamma^2\,n} \cdot \left(1 + \frac{K^2}{2} + \gamma^2\theta_\mathrm{o}^2\right) , \tag{2.40}$$

where n is the harmonic order of the emission. Hence, the observed wavelength of a certain harmonic depends not only on the electron energy (γ) and the undulator (λ_u, K) but also on the angle of observation. The natural linewidth of fundamental radiation is $\Delta\lambda/\lambda = 1/N_\mathrm{u}$ since the electron performs N_u oscillations.

Considering the fundamental ($n = 1$), the so-called central radiation cone is defined with opening angle θ_cen such that the relative wavelength change at this angle equals the natural spectral bandwidth:

$$\theta_\mathrm{cen} = \frac{\sqrt{1 + K^2/2}}{\gamma\sqrt{N_\mathrm{u}}} . \tag{2.41}$$

The central radiation cone is mainly determined by $1/\gamma$. For the radiation emitted along one period λ_u and in comparison with Eq. (2.37), we see that for $K < 1$ the emitted radiation lies within the angular excursion of the electron trajectory, whereas for $K > 1$ the trajectory covers a larger range of angles. This is crucial for whether radiation of a single electron can self-interfere or not. Therefore, one distinguishes undulators and wigglers, since the emitted radiation of both kinds is quite different:

$$K \begin{cases} < 1 & \text{undulator: discrete harmonics} \\ > 1 & \text{wiggler: continuous spectrum .} \end{cases} \tag{2.42}$$

The average power radiated by a single electron in the central cone and therefore per

relative bandwidth $\Delta\lambda/\lambda = 1/N_{\mathrm{u}}$ may be expressed by [3]

$$P_{\mathrm{cen,e}} = \frac{\pi\,e_0^2\,c\,\gamma^2}{\varepsilon_0\,\lambda_{\mathrm{u}}^2\,N_{\mathrm{u}}}\frac{K^2\,f(K)}{(1+K^2/2)^2} \tag{2.43}$$

where $f(K)$ corrects for reduced power due to higher harmonics for high K (which was omitted so far, [3]) and ε_0 is the permittivity of free space. Power and energy emitted into arbitrary frequency intervals and solid angles may be calculated as well, but depend on the actual conditions. The total radiated power of a single electron, i.e. now radiated in all directions, is [3]

$$P_{\mathrm{tot,e}} = \frac{\pi\,e_0^2\,c\,\gamma^2}{3\,\varepsilon_0\,\lambda_{\mathrm{u}}^2}\frac{K^2\,f(K)}{(1+K^2/2)^2}\ . \tag{2.44}$$

The energy emitted by a single electron may be calculated with help of the duration of the emission $t \approx N_{\mathrm{u}}\lambda_{\mathrm{u}}/c$. This yields for the total emitted energy $W_{\mathrm{tot,e}}$ from a single electron for fundamental undulator radiation

$$E_{\mathrm{tot,e}} = \frac{\pi\,e_0^2}{3\,\varepsilon_0}\frac{N_{\mathrm{u}}\,\gamma^2\,K^2\,f(K)}{\lambda_{\mathrm{u}}\,(1+K^2/2)^2} \tag{2.45}$$

and for the energy in the central radiation cone

$$W_{\mathrm{cen,e}} = \frac{\pi\,e_0^2}{\varepsilon_0}\frac{\gamma^2\,K^2\,f(K)}{\lambda_{\mathrm{u}}\,(1+K^2/2)^2}\ . \tag{2.46}$$

As a rough estimate, the number of emitted photons per electron is

$$N_{\mathrm{ph}} = W/W_{\mathrm{ph}} \tag{2.47}$$

with the photon energy $W_{\mathrm{ph}} = hc/\lambda$ and (2.40). Substituting constants with the fine structure constant $\alpha \approx 1/137$, the total number of photons is

$$N_{\mathrm{tot,e}} = \alpha\frac{\pi}{3}N_{\mathrm{u}}\frac{K^2\,f(K)}{(1+K^2/2)^2} \tag{2.48}$$

and in the central radiation cone

$$N_{\mathrm{cen,e}} = \alpha\,\pi\,\frac{K^2\,f(K)}{(1+K^2/2)^2}\ . \tag{2.49}$$

The radiation is usually expressed as spectral brilliance. This quantity measures the number of photons emitted per time interval (either per second, average brilliance, or

per pulse length, peak brilliance), per unit area, unit solid angle and spectral bandwidth. The unit is photons/(s mm^2 mrad^2 0.1% BW). This is due to the standard use of synchrotron radiation. Commonly the radiation is filtered via Bragg reflection for X-Ray diffraction experiments and focused onto a target. Therefore, a relative bandwidth of $10^{-3} = 0.1\%$ is a typical order of magnitude, and the product of source size and source divergence determines the focus. The product of source size and source divergence is identical to the transverse emittance, Eq. (3.3) in Sec. 3.4.1, of the generating electron beam.

2.4.2 Effects for electron bunches

For the radiation from an electron bunch, several effects may occur. In the simplest case, the radiation superimposes incoherently if the electrons in the bunch are uncorrelated. Then, the power emitted by the bunch is the sum of all electrons. Eqs. (2.43) - (2.46) are multiplied just with the number of electrons. However, if the electron bunch is quite divergent, the spectrum will be affected due to θ_o in Eq. (2.40). This may also happen if the bunch is quite wide and the undulator field is not constant. Usually, the field strength increases toward the poles (x) and has finite transverse extent (y). This may be regarded best via simulations, i.e. SPECTRA [52].

The opposite case is a coherent superposition of the waves emitted by the single electrons. For that, all electrons must by allocated within a volume smaller than the emitted wavelength, or must have a corresponding spatial modulation. Then, the radiated power scales quadratically with the bunch charge. This is fulfilled for wavelengths which exceed the electron bunch length. For laser-accelerated electrons, the bunch length upper limit is $50\,\text{fs} - 100\,\text{fs}$ [53, 54, 55, 56]; simulations suggest much shorter durations [19]. A 3 fs electron pulse would act as a coherent source for wavelengths larger than $1\,\mu\text{m}$. Such bunch could easily produce intense IR radiation. Therefore, measuring the synchrotron radiation spectrum and identifying coherent radiation could be used as an electron bunch duration measurement.

Coherent emission at sub-micron wavelengths, i.e. EUV and soft X-Ray radiation, is difficult to obtain with short-bunched electron pulses. This can be overcome with a so-called free electron laser (FEL). There, the interaction of the generated radiation field with the driving electron pulse is used to modulate the electron bunch with the radiation wavelength [57]. After modulation, coherent emission from this bunch is observed. This interaction is similar to the self-modulation of long laser pulses with the plasma wavelength (Sec. 2.2.2).

This process may be accomplished in two regimes. If appropriate mirrors are available, a resonator may be set up where the radiation field is preserved. Electron bunches are modulated by this field and amplify it further. This is the common approach for FELs in the infrared range.

For shorter wavelengths, resonators cannot be built due to a lack of appropriate mirrors. Then, very long undulators (or series of undulators) are used where initially incoherent radiation modulates the bunch. Then, partially coherent radiation is emitted, which enhances the modulation of the electron bunch. Finally, electrons become micro-bunched and emit coherent radiation. Those FELs are called SASE-FELs in analogy to optical lasing media where the gain is high enough to Self-Amplify Spontaneous Emission. Here, the "lasing medium" is a bunch of energetic electrons in an undulator.

Those SASE-FEL require precisely engineered undulators and high-quality electron beams with both low transverse and longitudinal emittance (see Sec. 3.4.1). Otherwise, the initial radiation would have a too large bandwidth, inhibiting micro-bunching. Micro-bunching is described by the Pierce parameter ρ [57, 58, 59],

$$\rho = \frac{1}{\gamma} \left[\left(\frac{\lambda_{\mathrm{u}}^2 K^2}{4\pi} \right)^2 \frac{I}{\sigma_x \, \sigma_y \, I_{\mathrm{A}}} \right]^{1/3} , \tag{2.50}$$

where $I_{\mathrm{A}} \approx 17,3\,\mathrm{kA}$ is the Alfven current and $\sigma_x \, \sigma_y$ the electron beam size (cf. Sec. 3.4.1). The gain length L, where any initial power e-folds, is

$$L = \frac{\lambda_{\mathrm{u}}}{4\pi \sqrt{3} \, \rho} \; . \tag{2.51}$$

Hence, for high gain and short interaction lengths, the Pierce parameter should be large and consequently the current density $Q/(\sigma_x \, \sigma_y \, \tau_{\mathrm{bunch}})$ too. A saturation of the process occurs after about 10 gain lengths which is consequently the ideal undulator length for a SASE-FEL.

3 Experimental methods

This chapter covers various experimental aspects. At first, the JETI laser system will be introduced briefly. The laser-plasma accelerator – the crux of the experiment – is then presented in detail because it is experimentally accessible and has the "adjustment knobs" for electron beam properties. The last 3 sections describe diagnostic methods for the laser-plasma interaction, electron beams and synchrotron radiation.

3.1 The JETI laser system

All experiments presented in this thesis were carried out with the JETI laser system. This is a 10 TW class CPA laser system based on Titanium:Sapphire, see Figure 3.1. A short pulse oscillator generates 45 fs pulses (FWHM) with about 10 nJ energy at a
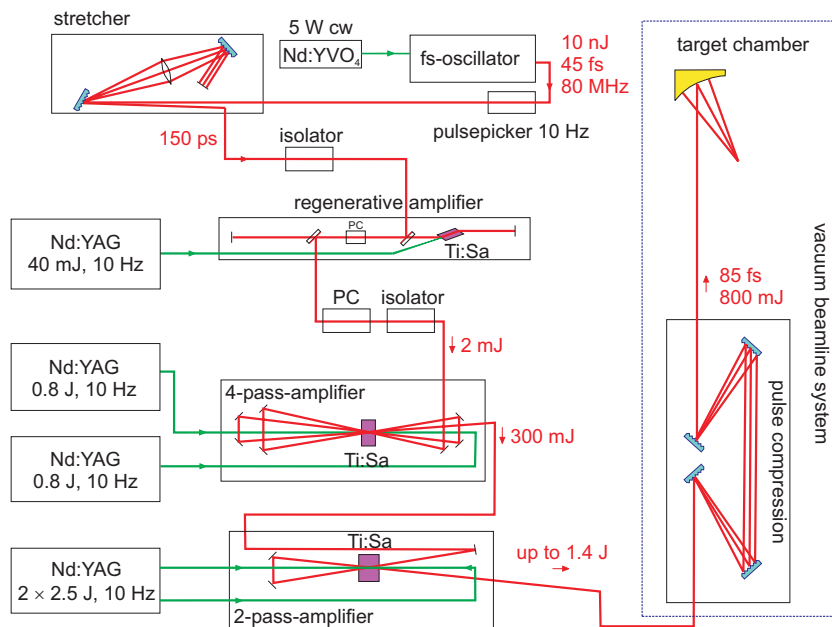
Figure 3.1: Schematics of the JETI laser system.

repetition rate of about 80 MHz. The spectrum is centered at 795 nm with a bandwidth

(FWHM) of 20 nm. A pulse picker reduces the repetition rate to 10 Hz. The pulses are stretched by a factor of 3000. A regenerative amplifier pushes the pulse energy to about 3.5 mJ within 20 roundtrips. A fast pockels cell is deployed for ASE contrast enhancement, but reduces the pulse energy to 2 mJ. The beam diameter is then increased by a telescope, and two multipass amplification stages boost the pulse energy to the Joule level (max. 1.4 J). The beam diameter is increased once more to 5 cm diameter, and the pulses are compressed to a duration of 85 fs FWHM with an efficiency of 60%. Hence, the system can produce pulses of 10 TW power. The system runs very reliable, usally 5 days a week for about 8 hours a day. Switch-on prodcedures are partially automated, and only 30 min of user operation are necessary. During the day, pulse energy and pointing may change slightly which can be compensated immediatly since various monitoring devices are installed. On a longer time scale like months, the system performance like pulse duration, pulse energy or beam profile is constant. This is an important fact since the experiments described in this thesis were distributed to several campaigns.

3.2 The laser-plasma accelerator

3.2.1 Setup of the laser-plasma accelerator

A laser-plasma accelerator for electrons relies on the interaction of an intense laser pulse with underdense plasma as described in Chapter 2. Since the laser propagates in vacuum in order to avoid any premature interactions, the plasma must be created locally at the laser focus. A very simple but robust and reliable setup deploys a pulsed gas nozzle in order to generate a gas jet, see Fig. 3.2. The gas is ionized by the leading edge of the laser pulse via multi-photon ionization, tunnel ionization and optical field ionization. This ionization takes place at intensities in the range of $10^{12}\,\mathrm{W/cm^2} < I < 10^{15}\,\mathrm{W/cm^2}$ which are reached several FWHM pulse durations τ_{L} ahead of the pulse peak. Helium is used in order to have inert chemical conditions and a fully ionized plasma when the pulse peak arrives. The fraction of laser energy consumed for ionization is negligible. Thus, the main part of the pulse always encounters a fully ionized plasma.

3.2.2 Gas jet target

The gas jet is usually circular symmetric. The radial profile may be shaped like a Gaussian or Super-Gaussian, depending on the nozzle design, that is, whether the gas flow is supersonic or subsonic. For a supersonic flow, tapered nozzles (Laval nozzles)
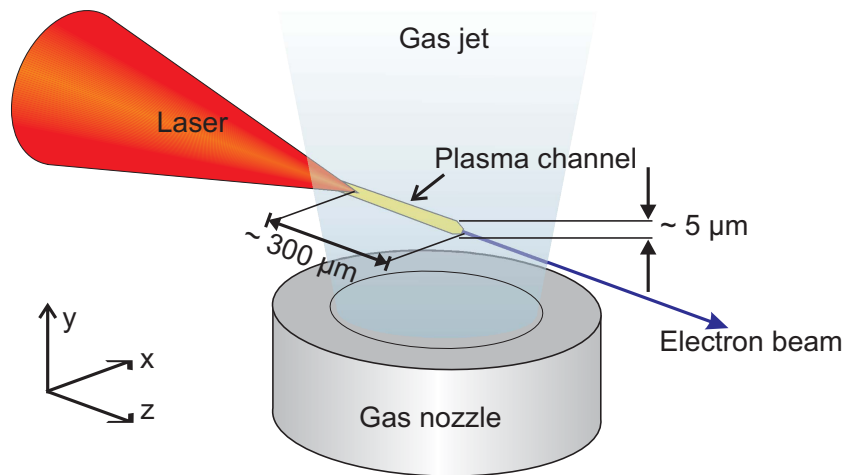
Figure 3.2: Schematics of the laser-plasma accelerator. An intense laser pulse is focused into a gas jet. Along the laser's path, the gas is ionized. Due to the interaction between laser and plasma at relativistic intensities, the laser pulse propagates in a self-formed channel. In the channel, the laser pulse generates strong plasma waves, wherein electrons can be accelerated. All interactions depend strongly on the initial gas density profile which may be controlled by different nozzle designs.

with a certain opening angle are used and the surface roughness is important [60]. A supersonic nozzle produces a radial profile with steeper edges and a rather constant plateau in the middle. Furthermore, the density drops along the flow direction (y) slower than for a subsonic nozzle.

The density profile which the laser pulse encounters depends on a multitude of parameters:

- the relative position of laser focus and nozzle,

- the time delay between nozzle opening and laser pulse arrival

- the opening time, and

- the backing pressure of the nozzle.

This allows for fine tuning of the plasma parameters during the experiment, but is complex due to plenty of parameters.

In the experiments described here, two different gas nozzles were used. From previous experiments at the JETI [49, 61, 62, 63, 64], subsonic nozzles were approved and available. However, supersonic nozzles were already under development and became available. In the experiments, both types were used and studied for electron acceleration.

Figure 3.3 shows electron density profiles which may be obtained from subsonic (solid lines) or supersonic (dashed line) nozzles. Shown are typical electron densities which can
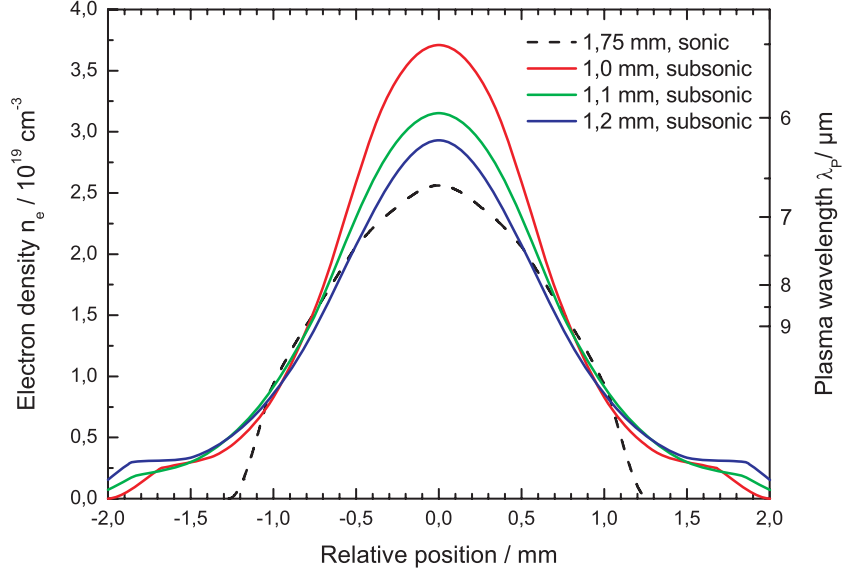
Figure 3.3: Electron densities of supersonic (dashed line) and subsonic (colored solid lines) gas jet targets for different distances between nozzle orifice and laser axis, measured with a Mach-Zehnder-interferometer in advance of laser-plasma interaction. On the right side, the density is converted to plasma wavelength according to Eq. (2.21) since the ratio of λ_p to the laser waist and pulse length co-rules the interaction.

be obtained via full ionization of the Helium gas (but prior to strong interactions which would change the density) with a laser pulse propagating centric over the nozzle. The subsonic nozzle was cylindrical with 1.2 mm inner diameter, 50 bar backing pressure, $700\,\mu$s opening time and a delay between opening and laser incidence of $850\,\mu$s. For this nozzle type, the distance between nozzle orifice and laser axis (y direction in Figure 3.2) plays an important role. Therefore there are 3 profiles for different distances given. The supersonic nozzle has a 2 mm wide orifice with a 10° Laval cone. It was operated again with 50 bar backing pressure, but the opening time was $1600\,\mu$s and the delay $1650\,\mu$s, respectively. As can be seen, peak gas density and FWHM diameter are similar for the different nozzles. However, the subsonic nozzle produces a soft wing with a density of about $10^{18}\,\mathrm{cm}^{-3}$ and $500\,\mu$m radial extent at the vacuum-gas boundary, whereas the supersonic nozzle produces a sharper edge. Since the ratio of the plasma wavelength to laser beam diameter and laser pulse length decides, among other parameters, the acceleration regime, the local plasma wavelength is also shown in Figure 3.3.

The impact of different nozzle types on electron acceleration is presented in Sec. 4.3. From a practical point of view, supersonic nozzles have the advantage that the distance

from the nozzle orifice to the plasma is a little larger than for subsonic nozzles. This enhances the life time of the nozzle as the abrasion of the nozzle material induced by the plasma is reduced. However, the life time is on the order of 10^3 shots for both types, and the subsonic nozzles may be refurbished which is not possible with the supersonic nozzles due to their Laval design. Disadvantages of the supersonic nozzle are the increased gas input into the vacuum chamber which demands improved vacuum pumping or a reduced repetition rate, and the higher standards of machining the nozzle with attention on the surface roughness.

3.3 Diagnostics of the laser-plasma interaction

Online observation of the electron beams and the laser-plasma interaction is indispensable, since there is a multitude of parameters one can adjust online and which may also change uncontrollable from shot-to-shot. Electron beam properties are the "target figure" for an optimization of the interaction, see Sec. 4.3. Plasma diagnostics can monitor the interaction and the acceleration regime, or serve as indicator to optimize the nozzle position in case when electrons are not yet accelerated. Further it can give insights into the acceleration mechanism and help to explain the properties of the electron beams.

A transverse observation of the interaction region, which is shown in several modifications in Figures 3.4 and 3.5, can accomplish all those demands. On the one hand, the plasma emits light depending on the interaction, and on the other hand, a backlighting technique with a second ultra-short pulse may be deployed which makes various time-resolved detection schemes possible.

3.3.1 Plasma imaging

A fully ionized plasma at a pressure of about one atmosphere is a very bright light source. Due to collisions and recombination, a wide continuum is emitted. Further emissions typical for electron acceleration were introduced in Sec. 2.3, which are nonlinear Thomson-scattering and wave-breaking radiation.

Figure 3.4 (a) shows a sketch of the setup in order to image the self-emitted light onto a camera. This is a basic setup which may be modified and extended. Not shown are the camera and additional filters. Neutral filters can adjust the intensity to the camera's sensitivity, interference filters can identify and distinguish different emission processes.
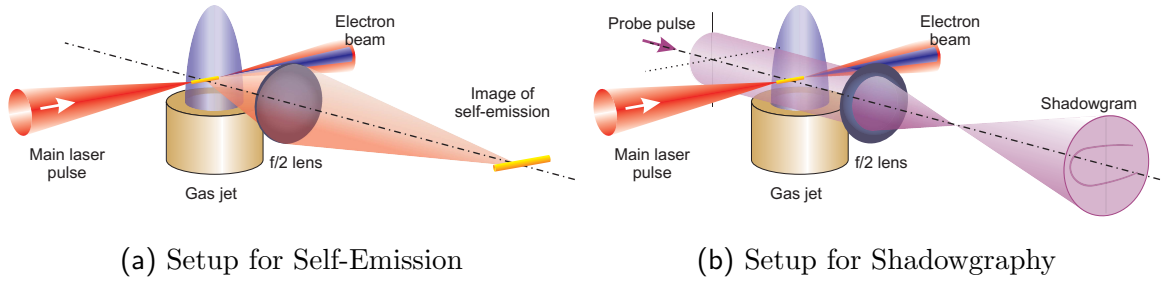
(a) Setup for Self-Emission   (b) Setup for Shadowgraphy

Figure 3.4: Setups for transverse plasma observation. a) Pure imaging of the interaction region onto a camera yields time-integrated images of the Thomson-scattered light and further emissions by the plasma. b) Combining this imaging with an ultra-short probe beam gives time-resolved images due to deflection of certain probe beam rays at gradients of the refractive index. Usually, the ionization front of the main laser pulse can be easily recognized via its characteristic horse-shoe shape as indicated. For clarity, the self-emitted light which is also imaged onto the camera is not shown.

The plasma recombines after the interaction and emits broadband radiation. Nonlinear Thomson-scattering, however, occurs at harmonics of the laser. In the experiments, small frequency intervals were observed with the help of interference filters for the laser frequency ($\lambda \approx 800\,\mathrm{nm}$) or second harmonic ($\lambda \approx 400\,\mathrm{nm}$). In the present work, only position and length of the emission were of interest, in contrast to earlier work [62, 49] where precise intensity profile measurements were made. The edge of the emission indicates the position of laser focus with respect to the gas jet position; length, profile and brightness of the emission enable to estimate the interaction process like channel formation, self-focusing or filamentation.

3.3.2 Optical probing techniques

If a transverse observation of the interaction region is set up and a short-pulse laser system is available, it can easily be combined to a transverse time-resolved probing. Therefore, a fraction of the main laser pulse is taken, passed over a variable delay line and then sent as a stroboscopic backlight along the transverse observation.

This ultra-short probe beam is a very versatile tool. At first, but disregarding its time resolution capabilities, it can be used to uncover the nozzle via its shadow. This is important to set up the interaction geometry. Secondly, many time-resolved techniques can be carried out. The effective time resolution is a little bit longer than the laser pulse duration due to group velocity dispersion in optical components the probe beam's path, transit time smear-out and convolution with the main laser pulse. However, it is still

on the order of the laser pulse duration.

If the setup is equipped with a shutter and appropriate filters, it can serve as both transverse observation and probing using the same imaging system by just switching the shutter. Furthermore, the probe beam may be frequency-doubled which is a further wavelength compatible with interference filters for nonlinear Thomson-scattering. This also enables for probing the same laser shot at two delay times [65]. In addition, the probe beam and the imaging setup may be equipped with polarizers and waveplates.

Shadowgraphy

The most straightforward usage of the probe beam is shadowgraphy of the plasma. This is caused by differences of the the refractive index of the plasma and the surrounding gas. The index of refraction of a plasma is given by Eq. (2.16), which is less than unity. The index of the gas is a little larger than unity, depending on the gas and the pressure. At index gradients, the probe beam is deflected which leads to intensity modulations of the probe beam at the image plane. This is shown in Figure 3.4-b). This technique is useful to study the propagation of the laser beam into the gas. Depending on the delay, the ionization front is at a certain position. Its propagation velocity may be determined, and filamentation of the laser pulse at the end of the gas jet may be detected [64].

Furthermore, the nozzle is always visible via its shadow. This helps to measure the distance between the relativistic channel (via Thomson-scattered light, therefore without probe beam) and the gas nozzle (with probe beam). This is a very important measure in order to set up the nozzle at the correct distance from the laser focus.

Interferometry

The probe beam may be also used for interferometry, that is, measuring the electron density distribution created by the laser. This is possible due to the dependence of of the index of refraction on the electron density, as given by Eq. (2.16). For instance, the formation and relaxation of a ponderomotive self-focusing channel may be observed [66].

For interferometry, the simplest setup uses a Nomarski interferometer [67], see Figure 3.5-a). It consists of a Wollaston prism and a polarizer. Additionally, another polarizer or a waveplate may be needed in order to generate linearly polarized light with a well-defined plane of polarization. The initial plane of polarization is set such that the outgoing o and e beams of the Wollaston prism have equal intensities. Then, the polarizer (not shown in Fig. 3.5-a)) lets both beams interfere at a region where
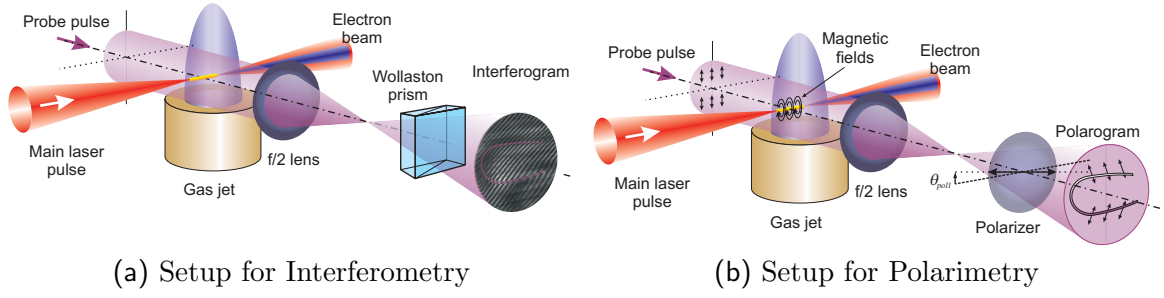
(a) Setup for Interferometry   (b) Setup for Polarimetry

Figure 3.5: Setups for transverse plasma probing. a) Interferometry of the plasma electron distribution with a linearly polarized probe pulse, a Wollaston prism and a polarizer (not shown). b) Polarography of the interaction region with a linearly polarized probe pulse and a polarizer. The plane of polarization may change due to magnetic fields from electron currents. If the polarizer is slightly detuned from highest extinction, regions may appear brighter or darker, depending on the sign of rotation.

they still overlap and are not yet separated. At the image plane, the part of one beam where a phase shift occurred is overlapped with a complementary part of the other beam which propagated undisturbed. Hence, for correct interferometry, the probe beam has to be large enough in order to pass not only through the interaction region but also through an undisturbed region in the vicinity since the very same beam serves as probe and reference. In addition, the separation angle of the Wollaston prism must be chosen correctly. The main advantage of this setup is that the existing probe beam setup can be used. Only little space is necessary for inserting the polarizer and the Wollaston prism, and the camera has to be shifted slightly due to the Wollaston prism. In contrast to a Mach-Zehnder interferometer, no beam splitters and beam combiners are needed, and no path length balancing with micrometer accuracy for temporal adjustment of sample and reference beam has to be done. However, the probe beam must have high spatial coherence.

Polarimetry

With a polarizer in front of the camera, the polarization state of the emitted radiation as well as changes of the polarization of the probe beam can be measured due to the extinction of the polarizer. This is given by Malus's law:

$$\frac{I}{I_0} = 1 - \beta_{\text{pol}} \sin^2(90° + \phi_{\text{rot}} - \theta_{\text{pol}}) \,, \tag{3.1}$$

where β_{pol} is the extinction coefficient for the polarizer, ϕ_{rot} the orientation of the plane of polarization of the light and θ_{pol} is the angle of the polarizer. The extinction

coefficient takes into account the degree of polarization of the probe beam and the contrast ratio of the polarizer. The angle's zero is defined for maximum extinction, that is perpendicular to the plane of polarization, since measuring the maximum extinction is more sensitive than maximum transmission. Hence, the polarizer should be set such that the undisturbed probe beam is blocked.

A setup scheme is shown in Fig. 3.5 (b). The captured image, called polarogram, is in principle a shadowgram. At certain positions where the plane of polarization has been rotated, the intensity of the probe beam at those positions will change, depending on the relative orientation of the polarizer to the initial plane of polarization as well as the rotation angle of the polarization plane in the plasma. If the polarizer is a little bit detuned from the angle of highest extinction, parts of the image where the polarization is change can occur both darker or brighter than unrotated parts, depending on the signs of ϕ_{rot} and θ_{pol}. This allows for the detection of the direction of rotation.

3.3.3 Deducing magnetic fields from electron acceleration

The plane of polarization of the probe beam may change in the plasma due to magnetic or electric fields created by the laser-plasma interaction. Those effects are the Faraday effect, the Cotton-Mouton effect and the Kerr effect. The Pockels effect occurs only in non-centrosymmetric media. Both electro-optic effects are not known for plasma [51]. The rotation due to Faraday effect and Cotton-Mouton effect were presented in Sec. 2.3.3.

For recapitulation, with circular symmetry of azimuthal magnetic fields and transverse probing, only the Faraday effect is operative, the Cotton-Mouton effect cancels out, and both the magnetic field distribution as well as the electron density distribution contribute to the rotation. Thus, only from the combination of a polarogram and an interferogram the magnetic field distribution can be deduced. This requires the acquisition of polarograms and interferograms for the same shot or, at least, for identical experimental conditions.

Under experimental conditions, the measurement is complicated by the superposition of the polarogram with the shadowgram. In order to determine the sign of rotation (clockwise or counterclockwise) and to discriminate bright and dark regions caused by Faraday rotation against other intensity modulations (e.g. the probe beam profile or the ionization front), the beam must be split and a second image must be taken as reference. This works best if a second polarizer and a second camera are deployed and

the polarizers are detuned from maximum extinction in an oppositional way:

$$I_{\mathrm{pol1}} = I_0 \left[1 - \beta_{\mathrm{pol1}} \sin^2(90° + \phi_{\mathrm{rot}} - \theta_{\mathrm{pol1}}) \right]$$

$$I_{\mathrm{pol2}} = I_0 \left[1 - \beta_{\mathrm{pol2}} \sin^2(90° + \phi_{\mathrm{rot}} - \theta_{\mathrm{pol2}}) \right]$$

(3.2)

where $\theta_{\mathrm{pol1}} \approx -\theta_{\mathrm{pol2}}$. Then, the background signals occur with equal intensities, but rays where the plane of polarization was rotated occur for one camera brighter but for the other darker.

The next step of evaluation is a pixel-wise division of the images and deducing the angle of rotation ϕ_{rot} for known values of $\beta_{\mathrm{pol1}}, \beta_{\mathrm{pol2}}, \theta_{\mathrm{pol1}}, \theta_{\mathrm{pol2}}$. Therefore, the extinction behavior for the polarizers must be measured with the same setup in order to include the finite degree of polarization of the probe beam, other optical components of the setup and wavelength effects.

Before the rotation map ϕ_{rot} may be converted into a magnetic field distribution, the electron density distribution must be known. This can be accomplished via interferometry. For both cases, a radial distribution has to be derived from a projection of this distribution onto an image plane. For that, a circular symmetry of both the magnetic field distribution and the electron density distribution has to be assumed. Otherwise, a more complex tomography setup would have to be deployed.

Finally, from the map of ϕ_{rot} and the electron density distribution $n_{\mathrm{e}}(r, z)$, the radial magnetic field distribution is derived from an Abel inversion of Eq. (2.32). Alternatively, simulations may be carried out based on the laser parameters and the density distribution, and a rotation map ϕ_{rot} may be computed and compared with the measurement.

This technique is a very useful method to investigate the electron acceleration process in the plasma in a non-invasive, in-situ manner. It is comparable to Thomson-Backscattering [63, 49] or wakefield holography [68]. However, in contrast to those methods, a high spatial and temporal resolution is possible due to the transverse geometry. The time resolution is limited both by the probe pulse duration and the transit time of the probe pulse through the plasma, and is comparable the the temporal resolution of Thomson-Backscattering (wakefield holography is time-integrated). The spatial resolution of this scheme may be unprecedentedly high ($\sim \mu$m).

3.4 Electron beam characterization

Since in the course of the present work electron beams were generated in order to produce synchrotron radiation, they must be characterized in a comparable way as in conventional accelerator facilities. There, the beams are of course very well known and a couple of figures of merit have been introduced historically.

3.4.1 Nomenclature at conventional accelerators

Transverse domain

A single electron has a well-defined charge, mass, position and velocity (energy), if quantum effects are not of interest. For electron beams, the situation is more complex. The individual electron trajectories are ignored, just an envelope is considered. However, like for laser beams, the electrons are not sharply confined, the envelope accounts for the $1/e$-surface. The beam itself is usually approximated by a Gaussian transverse profile. Within the beam profile, electrons may move around and do not stay at a fixed position. Beam diameter and divergence are coupled due to beam focusing, in analogy to the beam parameter product in optics. They are summarized in the transverse emittance $\varepsilon_\perp$ of the electron beam. Usually in accelerator science, the emittance is distinguished for both transverse directions x and y. Thus we have

$$\varepsilon_x = \sigma_x \sigma'_x \tag{3.3a}$$

$$\varepsilon_y = \sigma_y \sigma'_y \tag{3.3b}$$

$$\varepsilon_\perp = \sigma_x \sigma_y \tag{3.3c}$$

where σ is the beam $1/e$ radius and σ' the beam divergence. The unit is mm^{2}mrad^2. Usually for synchrotron radiation facilities, the emittance should be small in order to focus the beam very narrow but collimated over a long distance.

Longitudinal domain

In conventional accelerators, the electron beam is usually pulsed but quasi-cw with a certain repetition rate f_accel. Hence, the beam current may be measured as average current or as peak current. The temporal structure of a single electron bunch of the beam is again usually assumed as Gaussian with pulse duration τ_bunch. Therefore we

have

$$I_{\text{avg}} = Q_{\text{bunch}} \cdot f_{\text{accel}} \tag{3.4a}$$

$$I_{\text{peak}} = Q_{\text{bunch}} / \tau_{\text{bunch}} \tag{3.4b}$$

where Q_{bunch} is the charge of a single bunch.

Conventional accelerators produce highly monoenergetic electron beams with central energy E_{bunch} and energy spread ΔE_{bunch}, where $\Delta E_{\text{bunch}} << E_{\text{bunch}}$. Due to the long life time of an electron bunch in a conventional accelerator (due to its length), time-of-flight dispersion of the electron bunch must be considered. The energy spread is therefore coupled with the pulse duration, and the longitudinal emittance

$$\varepsilon_{||} = \Delta E_{\text{bunch}} \cdot \tau_{\text{bunch}} \tag{3.5}$$

is introduced in close analogy to the time-bandwidth product of short laser pulses.

Remarks

In contrast to laser pulses, an electron pulse may interact with itself due to space-charge effects and increase both transverse and longitudinal emittance. Those space-charge effects are investigated thoroughly in accelerator science, since they are dominant at the electron source (gun) of conventional accelerators where the electrons are very slow. Furthermore, especially for storage rings, the interaction of the magnetic guiding structure ("lattice") with the electron beam is also of interest since the guiding magnets may filter the beam and the long circulation of the beam leads to a lower limit of the emittance. From the guiding structure which transfers the beam, a guiding matrix may be calculated. It contains the so-called Twiss parameters [58] which determine the exchange between beam size and divergence and the dispersion, since usually the emittances are constant. Thus, it is possible to characterize the electron beam only with the machine parameters, e.g. the emittance (characteristic of the electron gun) and the Twiss parameters. In contrast, laser-accelerated electron beams can only be characterized by divergence or size. But for a further use of the electron beam, the emittance is very important quantity.

3.4.2 Scintillating screens

Electron beam profiles were determined with camera-observed scintillating screen Konica KR which uses $Gd_2O_2S{:}Tb$ as scintillator. Thereby, immediate access to the electron beam profiles is provided which is an essential feedback for online control of the plasma parameters and optimizing the acceleration conditions.
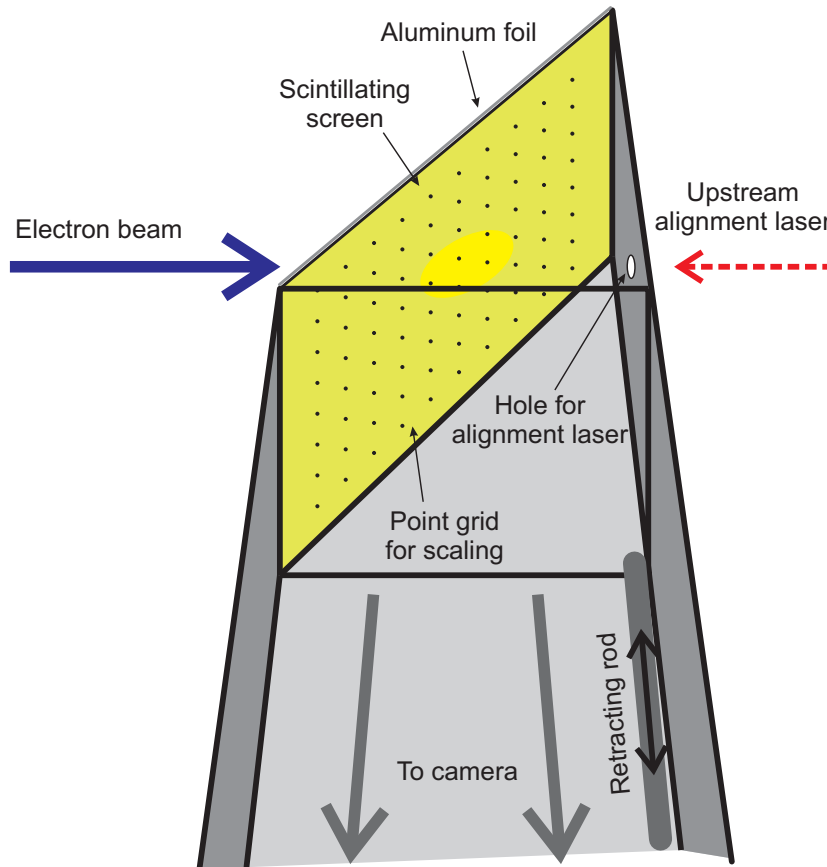
Figure 3.6: Scheme of the scintillating screen devices used for measuring the electron beam profiles. Shown is a view from above the camera without light screening on the top and without vacuum tubes. The brighter oval spot on the screen indicates the scintillation of the material due to electrons.

A scheme of the screen setup is shown in Figure 3.6. The screen is hit by the electrons under 45° and is observed perpendicular to the electron beam direction. This arrangement provides almost undistorted images and the screen is retractable out of the electron beam path without breaking the vacuum. The screen has a size of $9 \times 12\,\mathrm{cm}^2$ in order to fit into ISO-K 160 vacuum tubes. The effective area is $9 \times 9\,\mathrm{cm}^2$. The solid angle depends on the distance to the source (gas nozzle) which can be chosen arbitrary. In the experiments, the screen center was placed 31 cm away from the gas

nozzle. This corresponds to an effective full opening angle of 16° or 80 msr full solid angle, respectively. The distance to the electron source changes slightly with horizontal position on the screen. To the scintillating screen, a transparency foil with a $5 \times 5 \text{mm}^2$ point grid is attached in order to have a scale on each acquired image. This grid is also used for setting up sharp imaging. The camera is usually placed in a distance of about 40 cm away from the screen center. The spatial resolution depends on the imaging and was determined to 0.5 mm. This in turn corresponds to an angular resolution for electron beam profiles of 1.6 mrad.

The scintillating screen is housed in light-tight frame. Toward the electron beams it is shielded by $15\,\mu\text{m}$ thin aluminum foil, elsewhere with black cardboard, plastic foil or bellows. At the exit side of the frame, a hole is located which may be covered with aluminum foil. This hole allows for alignment of the camera. The electron beam path is aligned with two HeNe lasers propagating downstream and upstream. If the scintillating screen is inserted, it blocks the downstream laser but the upstream beam can irradiate the screen through the hole. By that, the position of the axis on the screen can be recorded. Finally, the hole is closed in order to complete laser light shielding.

Sensitivity and dynamic range of this beam monitoring depends on the imaging lenses, camera model, stray light protection and screen material. A precise determination of the sensitivity was not performed. However, the detection was sufficiently sensitive that the aperture of the camera objective was closed in order to avoid overexposed images which would prevent the determination of electron beam divergence.

The shortcomings of such a setup are:

- The screen material is primarily intended for converting X-rays to green light in order to expose standard orthochromatic film in medical applications. Hence, the radiation background of the laser-plasma interaction and bremsstrahlung from electron stopping in vacuum vessel walls can produce a variable but rather homogeneous background signal.

- No absolute calibration in terms of measuring charge per unit area is possible. Although imaging parameters like distance to the camera or aperture setting may be fixed, the scintillation signal depends on the electron energy since slow electrons ($E \lesssim 1\,\text{MeV}$, [69]) produce more bremsstrahlung in the screen than high-energy electrons. Hence, a calibration against an imaging plate as for the electron spectrometer (see Section 3.4.3) is not possible.

- No further use of the electron beams is possible due to energy-dependent scattering

in the screen. Hence, electron beam profile measurements cannot be executed simultaneously but only consecutively with other measurements using the electron beam.

3.4.3 Electron spectrometer

Electron energy spectra were measured with an electron spectrometer, see Fig. 3.7. It is based on permanent magnets inside an iron yoke. The input aperture is 2 cm, the magnetic field strength is 720 mT, extending 20 cm in length (z) and 10 cm in width (x), with a gap of 2 cm (y). Scintillating screen Konica KR in combination with a CCD camera is used for online electron detection, covering electron energies from 14 MeV to 85 MeV.
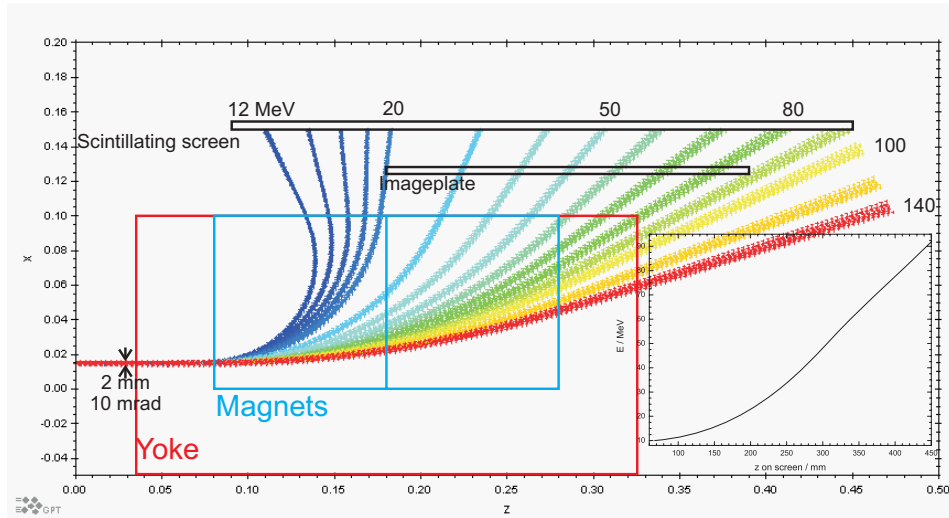
Figure 3.7: Scheme of the deflection of electron trajectories inside the electron spectrometer. The magnetic field was measured in 3D and a particle tracking simulation with GPT [70] was carried out. Electron beams with different energies but uniform input emittance were tracked through. The focusing effect for low energy beams can be seen from the width at the screen of beams with different energies. The inset shows the electron energy calibration graph. The dispersion is for energies above 30 MeV approximately linear.

For the simultaneous detection of electron spectra and undulator radiation spectra (cf. Chapter 5), the spectrometer was calibrated in terms of measuring charge very carefully against an imaging plate Fuji BAS-MS2025. This imaging plate can be inserted 15 mm in front of the scintillating screen. Data for the response of the imaging plate and the scintillating screen are taken from [71, 69], respectively. The dispersion was determined by particle tracking based on measurements of the magnetic field including edge effects.

As can be seen from the inset in Fig. 3.7, the dispersion (deviation per energy) is approximately linear for energies above 30 MeV. The sensitivity was determined to be better than 0.5 pC/MeV, which depends on imaging, camera type, stray light protection and imaging plate processing. The sensitivity already regards the actual setup since it is primarily charge per area. The area is converted to an energy interval considering dispersion and imaging.

The large input aperture ensures electron detection with the spectrometer even for uncollimated and spatially fluctuating electron beams, but input position and injection angle of the electrons are not well-defined. Due to scattering, a scintillating screen in front of the input (see Section 3.4.2) is not an option to measure the input position and beam divergence. Both uncertainties lead to different effects on the electron spectra:

- A divergence in horizontal direction (x) of an electron beam will pretend a broadening of the spectrum. Assuming a strictly monoenergetic electron beam but with a certain divergence (cf. Sec. 3.4), the initially very small beam will have a certain diameter after propagation. This size will be seen on the screen of the spectrometer and cannot be discriminated rigorously from the actual energy spread. A reasonable practice is to determine the divergence from the beam size in the non-dispersing direction of the screen (y), and assuming that the divergence in x is the same. This requires beam profile measurements with a scintillating screen in advance in order to substantiate this assumption.

- If the beam enters the spectrometer with a certain x-offset from the axis, the point of arrival at the screen will move and appear like from a beam with different energy. This offset depends on the deflection and therefore on the electron energy.

- If the beam enters with a certain vertical (y) offset or divergence, those electrons experience a stronger deflection since the magnetic field strength increases vertically toward the magnets. Therefore, electron beams can occur C-shaped, and must either be disregarded or deconvolved with a 2D energy calibration which includes the y-dependency.

- The particle tracking simulations show a focusing effect for electron beams with low energies. Due to the slightly longer path of the outer tracks, the deviation is slightly stronger and therefore the horizontal divergence is reduced. In fact, the plane of the scintillating screen was chosen under consideration of this effect. This leads to a slight decrease of the relative energy resolution toward low energies. However, the energy resolution is limited by the input position uncertainty.

3.5 Detection of synchrotron radiation

3.5.1 Construction of the undulator

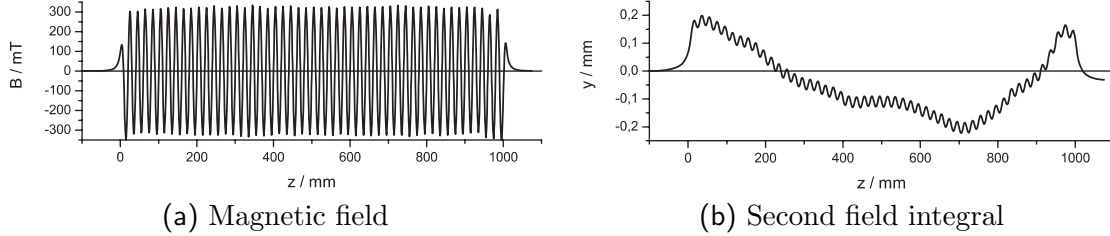(a) Magnetic field   (b) Second field integral

Figure 3.8: a) Magnetic field along x direction on axis as function of z. b) Trajectory of an electron with $\gamma = 100$, injected on axis. The electron exits parallel to the axis with a negligible offset of 30 microns.

The undulator was designed by K. Haupt especially for this experiment. The demand was to generated synchrotron radiation from electron beams which occur reasonably frequent in a spectral range where sensitive spectrometers are available. The relation between electron energy and wavelength of the produced radiation is given by Eq. (2.40). Therefore, the undulator produces radiation in the near-infrared and visible spectral range from electron energies of 55 MeV to 75 MeV.

The undulator is built from permanent magnets in hybrid structure with a period of $\lambda_u = 2$ cm and a length of 1 m ($N_u = 50$ periods). The gap between the magnets was set to 10 mm, the maximum magnetic field strength on axis was $B_0 = 330$ mT. The undulator parameter amounts to $K = 0.6$ and the correction factor $f(K = 0.6) \approx 0.93$[3]. The first and last 3 periods of the undulator were equipped with ferromagnetic screws allowing fine adjustment of the magnetic field for on axis injection and on axis exiting of the electrons. Figure 3.8 displays the measured B-field on axis and the path of the electron, Eq. (2.36), for $\gamma = 100$ through the undulator, injected on axis. Both the excursion of up to 200 microns and the deviation of 30 μm from the axis at the exit are negligible for electron beams with diameters larger than 1 mm. On-axis exiting is a requirement for subsequent determination of electron energy in the permanent magnet spectrometer and was therefore taken into consideration at this point.

3.5.2 Optical detection system

The synchrotron radiation from the undulator was collected by an AR-coated plano-convex lens of 47 mm diameter and 105 mm focal length, and focused into the entrance

slit plane the optical spectrometer. This was a symmetrical 200 mm Czerny-Turner spectrometer, equipped with a thermoelectrically cooled CCD camera (Andor DO-420 BN). The camera was shielded with lead against X-rays from electron stopping in the vacuum vessel walls. The 26.6×6.7 mm^2 CCD chip (1024×256 pixels) was operated in hardware binning mode, merging arrays of 8×12 pixels together to superpixels. This was useful since there was no need for high spectral resolution, and thermal noise as well as quantization errors are reduced in this mode. The spectral range was set to 560 nm - 990 nm. The wavelength calibration was accomplished with a Hg-vapor lamp. The spectrometer efficiency was carefully calibrated with a HeNe laser, a fast shutter and parallel exposure time measurements. Due to the intrinsically parallel photon detection within each CCD pixel saturation of the signal from the ultra-short pulses does not occur. To correct for the quantum efficiency of the detector, the manufacturer's data was used.

Raytracing simulations of the optical system, carried out with Zemax, showed that the collection angle for undulator radiation is just about 2 mrad which is significantly smaller than from geometrical estimation. The light source to be imaged by the lens into the slit plane is extended one meter in depth and therefore difficult to image onto the slit plane. With this simple lens, a significant loss of photon flux cannot be avoided. In the experiment, the longitudinal center of the undulator was imaged onto the slit plane.

3.5.3 Comparison of electron and radiation spectra

For the present work, accurate calculations of incoherent radiation spectra were carried out with a dedicated program based on [59] by A. Debus. For the measured magnetic field of the undulator (cf. Sec. 3.5.1), the trajectory and the Lienard-Wiechert-potentials [72] were calculated as function of the electron energy. Integrating over the solid angle of detection (see previous Section) and convolving with the measured electron spectrum (cf. Sec. 3.4.3), the radiation spectrum is obtained for arbitrary electron spectra. By that, precise comparison of measured radiation spectra with simulations based on measured electron spectra from the same shot was possible.

4 Electron acceleration with the JETI laser system

This chapter describes experiments for laser-based electron acceleration in view of producing synchrotron radiation, that is, generating well-collimated electron beams with monoenergetic spectra. Some results presented here were obtained from experiments dedicated to electron acceleration solely, and some other facts are from experiments at which the production of synchrotron radiation was the goal.
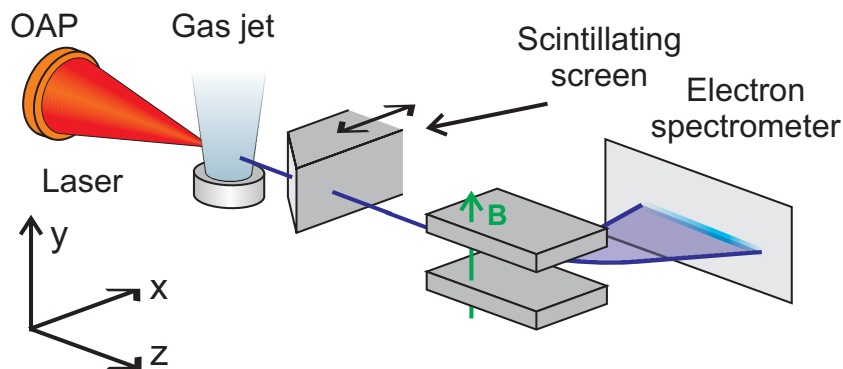
4.1 Experimental setup

Figure 4.1: Schematics of the setup for sole electron acceleration. Electrons are accelerated by focusing the JETI laser pulses into a Helium gas jet. The interaction region can be observed with various techniques as outlined in Sec. 3.3, see Figures 3.4 and 3.5. Electron beams can be analyzed with a scintillating screen for their spatial properties and with an electron spectrometer for their energy spectra.

Figure 4.1 shows the principle of the setup for electron acceleration experiments. The JETI laser pulses are focused into a Helium gas jet. Different parabolic mirrors and gas jet nozzle types can be deployed. The interaction region can be monitored via the multitude of techniques described in Sec. 3.3. The produced electron beams can be

analyzed regarding their spatial characteristics with a scintillating screen (Sec. 3.4.2) as well as their spectral properties with a magnet spectrometer (Sec. 3.4.3).

4.1.1 Focusing optics

The laser pulses were focused by either an $f = 30\,\text{cm}$, F/6, 30° or an $f = 50\,\text{cm}$, F/10, 15° off-axis parabolic mirror. Table 4.1 shows the focal spot sizes, focus diameters and Rayleigh lengths for both parabolic mirrors, assuming a Gaussian beam profile with a waist of 2.5 cm. In the bottom part of Table 4.1, the measured spot sizes for both FWHM and $1/e^2 \approx 0.135$ are given with their corresponding measured q-values which measure the energy within the spot size as a fraction of the total pulse energy. The theoretical q-value for the $1/e^2$ spot size is 0.95. In addition, Figure 4.2 shows images of the focal spots for both parabolic mirrors.

Focal length	30 cm	50 cm
Expected waist ($1/e^2$)	$3\,\mu\text{m}$	$5\,\mu\text{m}$
Expected spot size ($1/e^2$)	$30\,\mu\text{m}^2$	$80\,\mu\text{m}^2$
Expected Rayleigh length	$40\,\mu\text{m}$	$100\,\mu\text{m}$
Measured $1/e^2$ spot size and q-value	$410\,\mu\text{m}^2$ (0.72)	$1200\,\mu\text{m}^2$ (0.81)
Measured FWHM spot size and q-value	$95\,\mu\text{m}^2$ (0.33)	$288\,\mu\text{m}^2$ (0.38)
Measured FWHM waist	$5.5\,\mu\text{m}$	$9.6\,\mu\text{m}$

Table 4.1: Comparison of the two focusing parabolic mirrors.
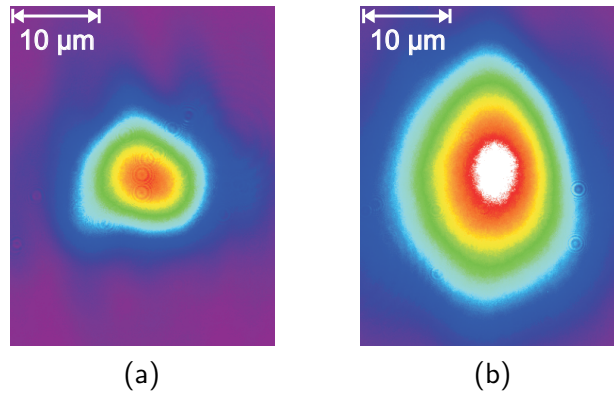
Figure 4.2: Focal spots for the a) $f = 30\,\text{cm}$ and b) $f = 50\,\text{cm}$ parabolic mirror. Note that different intensity scaling is due to different filtering. Both images show an area of $35 \times 45\,\mu\text{m}^2$.

Most obvious is the difference between theoretical and actual focus parameters. This is due to a mixture of the laser beam profile, probably the wave front, the machined

parabolic mirrors and focusing. During focusing (adjusting the parabolic mirror) it was tried to obtain a round focus which was not the smallest one.

The difference between theoretical spot size and measured spot size is about one order of magnitude. Furthermore, the actual spots contain less energy than they should. Therefore, the obtained intensities are significantly below theoretical estimates.

4.1.2 Expectations for electron acceleration

We can now estimate which regimes of electron acceleration (cf. Sec. 2.2) can be obtained. The plasma wavelength changes along the laser propagation and is in the range of $\lambda_\mathrm{p} = 6\,\mu\mathrm{m} - 20\,\mu\mathrm{m}$ (see Fig. 3.3). The total pulse energy on target is typically $\sim 500\,\mathrm{mJ}$, and the pulse duration is 85 fs. Therefore, the pulse length is $c\,\tau_\mathrm{L} \approx 25\,\mu\mathrm{m}$ which is for any position in the gas jet longer than the plasma wavelength. Only at small regions at the edges the pulse length fits the plasma wavelength and therefore the LWFA condition Eq. (2.22).

Focal length	30 cm	50 cm
I_FWHM	$2 \cdot 10^{18}\,\mathrm{W/cm^2}$	$0.8 \cdot 10^{18}\,\mathrm{W/cm^2}$
P_FWHM	2 TW	2.2 TW

Table 4.2: Values of intensity and power, averaged over the FWHM area of the foci, for the two parabolic mirrors.

Table 4.2 shows the values of the power and intensity in the focus of the corresponding parabolic mirror, averaged over the FWHM spot which slightly underestimates the following effects. In both cases, the average intensities do not exceed but approach the relativistic threshold, $a_0 \lesssim 1$. The power values are almost equal and are sufficient for self-focusing in densities above $1.4 \cdot 10^{19}\,\mathrm{cm^{-3}}$, cf. Eq. (2.20). Those densities are present in a wide range of the gas jet. Thus, self-focusing and subsequently self-modulation will take place. Considering self-focusing to a diameter equal to the plasma wavelength with constant power, e.g. 2 TW focused down to $5\,\mu\mathrm{m}$ diameter, the resulting intensity of $10^{19}\,\mathrm{W/cm^2}$ is relativistic ($a_0 \approx 2$) and almost suffices for wave-breaking.

The mechanism of self-modulation was identified in earlier experiments [46] to lead to the Bubble regime. We can estimate an upper limit for this regime with help of the simulations for the earlier experiments. It is a reasonable assumption that the power of the pulse remains constant whereas pulse energy and pulse duration decrease. Considering Eqs. (2.30) and (2.31), the maximum energy (from the initial pulse length) might be 155 MeV and the charge 200 pC.

A recent work [73] studied the influence of the focal spot size on the produced electron beams. It was found that for spot sizes larger than the plasma wavelength a single optical filament is formed and well-collimated monoenergetic electron beams can be produced, whereas for tight focusing broad spectra are obtained. This was explained with the help of simulations which showed a close relation between bubble-like wakefield structures and collimated electron beams. The generation of well-collimated electron beams depends pretty much on the self-interaction of the laser pulse with the plasma target which was already shown by Hidding *et al.* [46]. The focusing geometry (divergence, vacuum spot size and position relative to the target) seems to be more important than the mere vacuum spot size. For the experiments described here, the spot size is larger than in the earlier ones [46] and therefore better electron beams can be expected. However, this depends strongly on the self-interaction of the laser pulse with the plasma which cannot be controlled externally.

4.2 Plasma diagnostics

4.2.1 Plasma imaging

Figure 4.3 shows as example an image of the interaction region. The laser is incident from the left, the gas nozzle is visible as shadow at the bottom. The laser pulse undergoes self-focusing and forms a relativistic channel. This channel is partially visible from the nonlinear Thomson-scattered light at its beginning. After a small gap where the channel is not visible, wave-breaking radiation is visible. The large intense region is the plasma glow. The probe beam was attenuated in order to record both the self-emitted light and a shadowgram. The streaky structures are ionization traces.
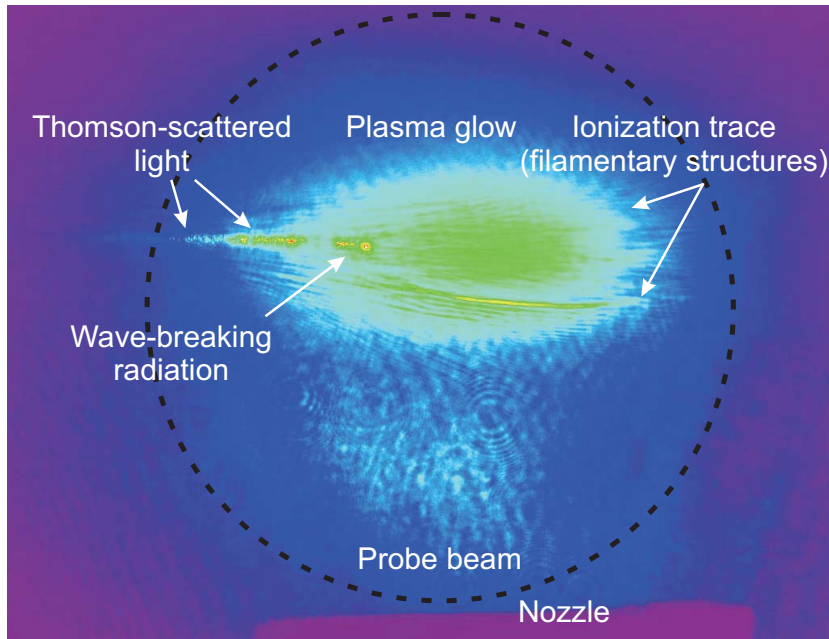
Figure 4.3: Exemplary image of the interaction region. This image was taken during setup of the nozzle with low plasma density. The probe beam (black circle) was activated in order to uncover the nozzle which is visible via its shadow at the bottom of the frame. The laser is incident from the left side. The relativistic channel can be partially seen via nonlinear Thomson-scattered light. Adjacent to the Thomson-scattered light there is a gap and then a bright region. This was identified as wave-breaking radiation, which is also part of the channel. Furthermore, the ionization of the gas is visible via shadowgraphy as approximately horizontal streaks. In the center of the gas jet (above the nozzle center) the plasma glow is visible.

With the help of interference filters, the origin of the emitting regions can be validated. This is shown in Figure 4.4. Each image shows the same region of the whole image for different interference filters. Each filter has a FWHM bandwidth of $10\,\text{nm}$. Shown are averages over ca. 20 consecutive shots in order to minimize shot-to-shot fluctuations. The images are slightly scaled to equal intensities of the plasma glow. From the wavelength of the second harmonic of the laser frequency, $\lambda = 400\,\text{nm}$, to $\lambda = 500\,\text{nm}$, the brightness of the relativistic channel decreases to a relative value of 2/3. Obviously, the nonlinear Thomson-scattered light is quite broad-band. However, the intensity of the wave-breaking radiation remains constant as well as the plasma glow. This behavior of the emitted light affirms the designations of the individual emission regions in Fig. 4.3.

(a) 410 nm

(b) 455 nm

(c) 500 nm
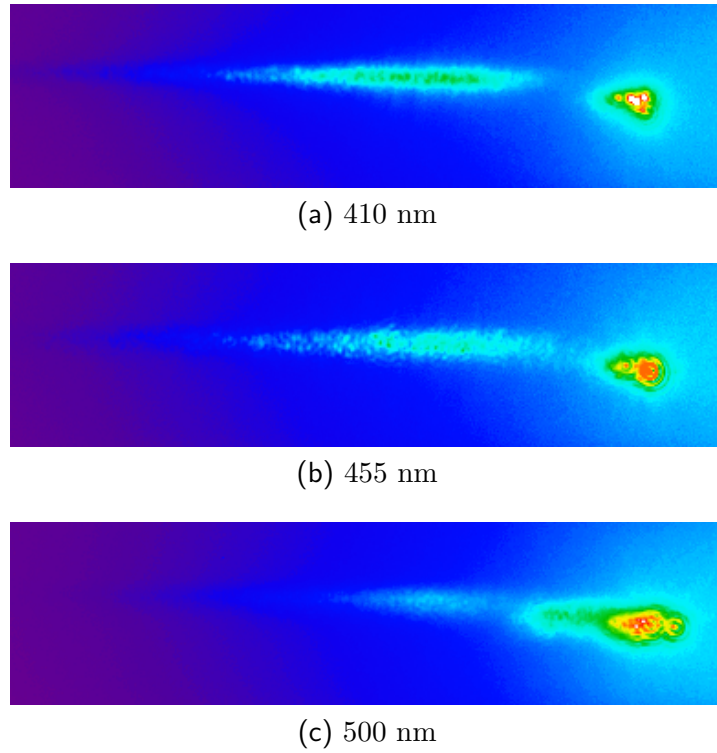
Figure 4.4: Detail of the plasma emission for 3 wavelength intervals. Each picture is an average over ca. 20 shots and was scaled for equal intensity of the plasma glow. The wave-breaking radiation remains bright whereas the intensity of the the nonlinear Thomson-scattering from the relativistic channel gets darker for increasing wavelength. Each frame is $900\,\mu$m $\times\,230\,\mu$m large.

4.2.2 Interferometry

With the interferometry setup, see Sec. 3.3.2, the electron density distribution of the plasma may be deduced with sufficient temporal resolution. Figure 4.5 shows an example interferogram and the deduced electron density distribution. The latter was derived from the interferogram and an reference interferogram via Abel's inversion and assuming cylindrical symmetry of the density distribution. Interferograms were recorded for identical delay settings of the probe pulse as were chosen for the polarograms, see next section, in order to deduce the time-dependency of azimuthal magnetic fields in the plasma.
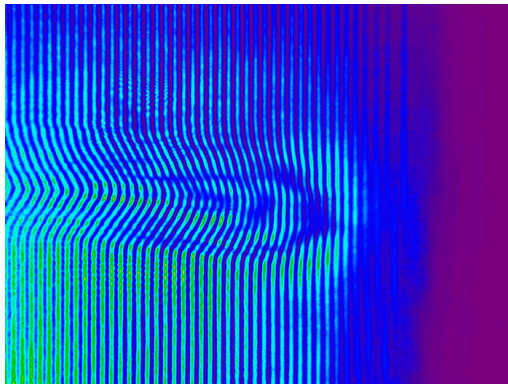
(a) Interferogram
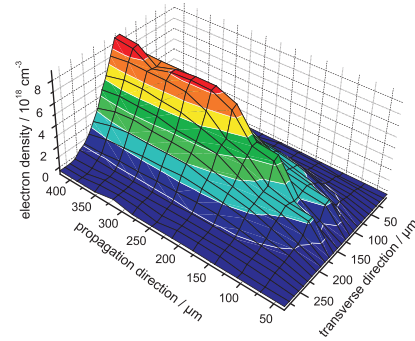
(b) Deduced density distribution

Figure 4.5: Interferometric time-resolved measurement of the electron density distribution of the laser-plasma. (a) shows an interferogram and (b) the deduced electron density distribution. The interference fringes of (a) end on the right side due to the probe beam size and the Nomarski interferometer setup. The length scales in (b) refer to an arbitrary origin.

4.2.3 Polarimetry

As described in Sec. 3.3.2, the polarization state of the observed radiation may be deduced with polarizers. Figure 4.6 shows in the top figures two polarograms (shadowgrams through a polarizer) for the same laser shot. The images were taken with help of a non-polarizing beam splitter and two polarizer-camera pairs where the polarizers were detuned from maximum extinction of the Thomson-scattered light (cf. Fig. 4.3) in an opposite way. As can be seen, it is difficult to distinguish intensity changes induced by the polarizer from further modulations.

This difficulty can be overcome by taking the ratio of the images, cf. Sec. 3.3.3. This is shown by the bottom image of Fig. 4.6. All intensity modulations which are not caused by polarization changes cancel out, only changes of the polarization remain (besides some noise). These are now easily to recognize as bright and dark regions in the center of the image. For known polarizer properties and settings, this image can be computed into a map of the angle of rotation (cf. Sec. 3.3.3).
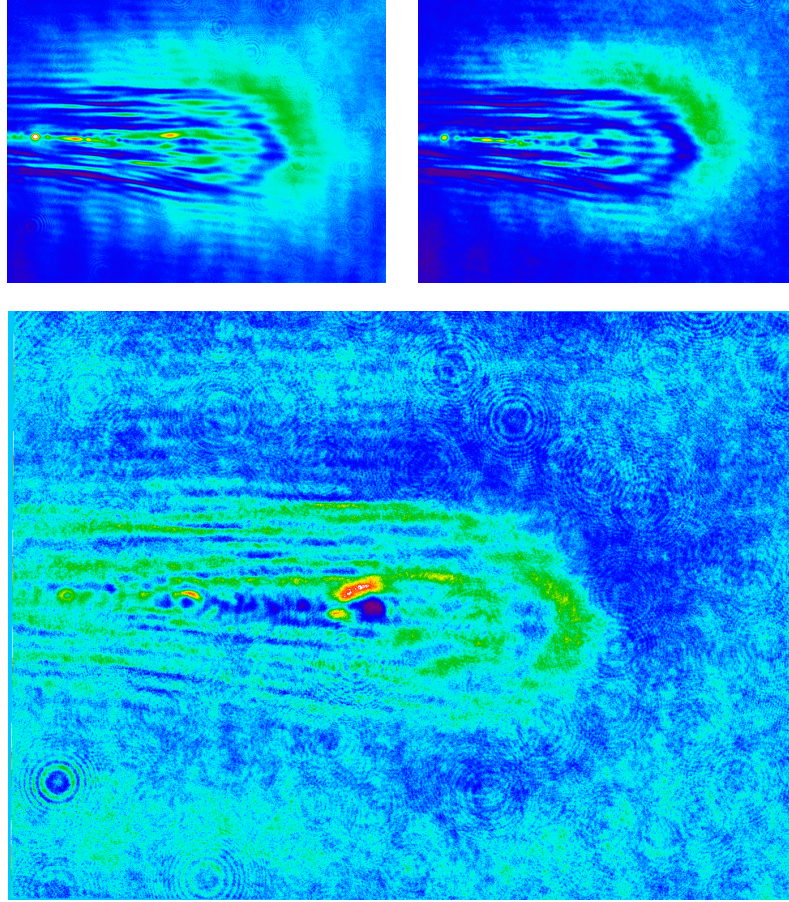
Figure 4.6: Top: Polarograms of the same laser shot with opposite polarizer settings. Bottom: Result of a pixel-by-pixel division of the raw polarograms.

4.2.4 Deduced magnetic fields

From the angle of rotation, in combination with the electron density distribution from interferometry, azimuthal magnetic fields in the plasma can be deduced (cf. Sec. 2.3.3 and 3.3.3). Results from such procedure are shown in Figure 4.7.

The first graph, (i) shows the intensity ratio of two polarograms along a vertical lineout through the most intense modulation in Fig. 4.6. As described in the previous section, from known polarizer settings and parameters, the angle of rotation of the initially linearly polarized probe beam may be derived. This is shown as blue line in (ii). As can be seen, the asymmetry of (i) is now reduced. This is due to the fact that a certain angle of rotation may yield an intensity ratio of $q : 1$ or $1 : q$, depending on the sense of rotation. Therefore, the intensity ratio of ≈ 1.8 in the left part of the graph is generated by roughly the same Faraday rotation as the ratio of ≈ 0.55 in the right

part ($1.8 \cdot 0.55 \approx 1$). Note that the shown angle of rotation function is suppressed at regions where the electron density is zero for numerical reasons. As can bee seen from the graph, the maximum angle of rotation amounts to $\approx 1°$ which is quite small. This can only be measured with the usage of two polarizer-camera pairs. The sensitivity is about $\approx 0.1°$.

The red line in (ii) shows the electron density distribution along the lineout. This is derived from interferometry, see Fig. 4.5 and Sec. 4.2.2. Attention must be drawn on identical settings, i.e. that the lineout is from the same position and the image take with the same time delay.

With both the angle of rotation and the electron density distributions, the magnetic field distribution may be deduced with the help of Abel's inversion and assuming circular symmetry of the electron density and field distribution [74]. The result is show as black line in (iii). In addition, a current distribution model may be taken and the induced magnetic field calculated for comparison. The red line is the magnetic field of a current of $2.8\,\mathrm{kA}$ and $6.5\,\mu\mathrm{m}$ radius, the gray dashed line of $3.2\,\mathrm{kA}$ and $8\,\mu\mathrm{m}$ radius, respectively. As can be seen, the peak magnetic field may be reproduced but the radial distribution cannot be explained by such simple model.

This procedure was carried out for several delays of the probe beam with respect to the main laser pulse in order to derive the temporal evolution of the magnetic fields. Those fields were observed for a period of 1 ps with a sudden increase in the center of the gas jet, see Fig. 4.9.

Furthermore, the position of the main laser pulse with respect to the gas jet center was determined. This was accomplished via ring-like interference structures, occurring if the probe beam had the same polarization and roughly same intensity as the self-scattered light and overlapped temporally and spatially with the nonlinear Thomson-scattered light.

Those additional measurements enabled PIC-simulations, carried out by S.P.D. Mangles with the OSIRIS code [75]. They were intended to explain both the radial distribution of the magnetic fields as well the time evolution and position in the gas jet. Results of those simulations are shown in Figure 4.8 and, combined with experimental results, in Fig. 4.9.
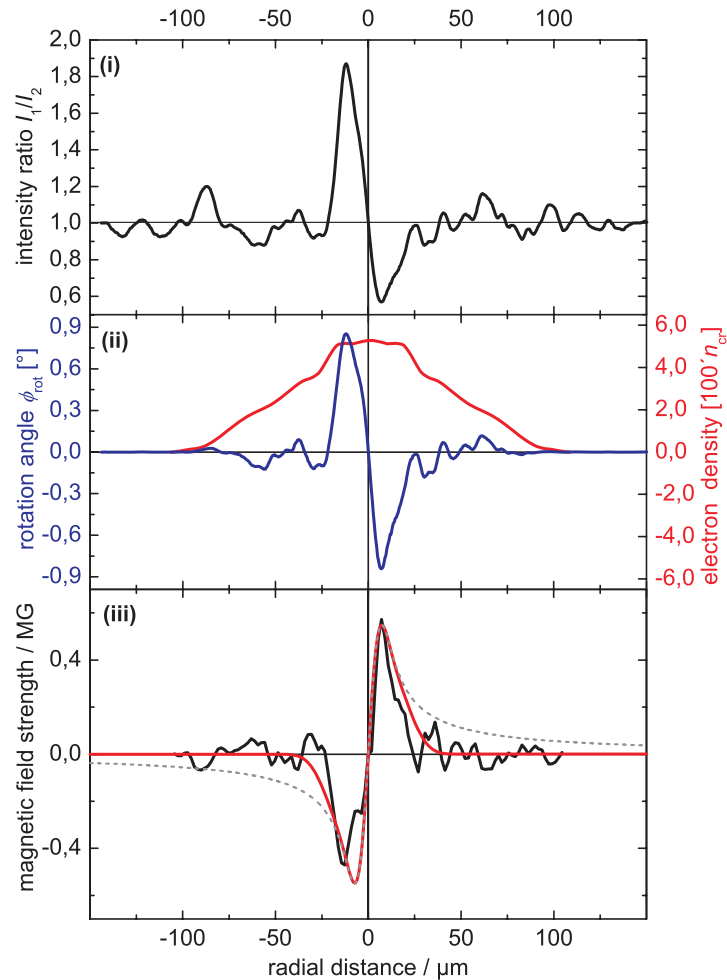
Figure 4.7: How to deduce magnetic fields from polarimetry and interferometry. (i) shows the intensity ratio along a vertical lineout from a polarogram (cf. Fig. 4.6). In (ii), the blue line is the angle of rotation of the probe beam along the lineout, derived from (i). The red line shows the electron density distribution along the lineout, derived from interferometry (cf. Fig. 4.5 and Sec. 4.2.2). (iii) shows as black solid line the magnetic field distribution, derived from (i) and (ii). The red and gray dashed line are calculated magnetic fields for certain current distribution models.

Figure 4.8 shows a snapshot of the simulation at the maximum of the magnetic fields. At this time the laser pulse is strongly self-modulated and split into parts, driving two bubble-like structures. Behind the second bubble, wave-breaking and plasma-heating prevent further wakefields. This can be seen in plot (a) where the electron density and laser intensity are shown.

Plot (b) shows the longitudinal current density where the forward electron current inside the second bubble is clearly visible as well as the snowplough effect at the front of each bubble and the backstreaming of electrons around the bubbles. Not shown is the transverse current density. In combination it could be seen that the wake currents form current loops around the bubbles.

Plot (c) shows the azimuthal magnetic fields associated with the currents. Two main contributions can be identified. Both bubbles create, since they are electron voids moving over an ion background [43], a displacement current due to the temporal change of the longitudinal electric field, $B_z \propto \dot{E}_x$ [76]. Furthermore, in the second bubble electrons are trapped which is forward current, generating an additional azimuthal magnetic field with the same orientation.

Plot (d) shows the subsequent Faraday rotation of a probe beam passing through the plasma. Note that the distribution of azimuthal magnetic field (c) and Faraday rotation (d) differ. This is due to the electron density distribution. Inside the second bubble, the highest magnetic fields are present, but the bubble is partially cavitated. For increasing radial distance, the magnetic field drops but the high density "wall" of the bubble allows for a maximum of Faraday rotation. Furthermore, the wake currents at the bubble wall shield the magnetic fields outsides.
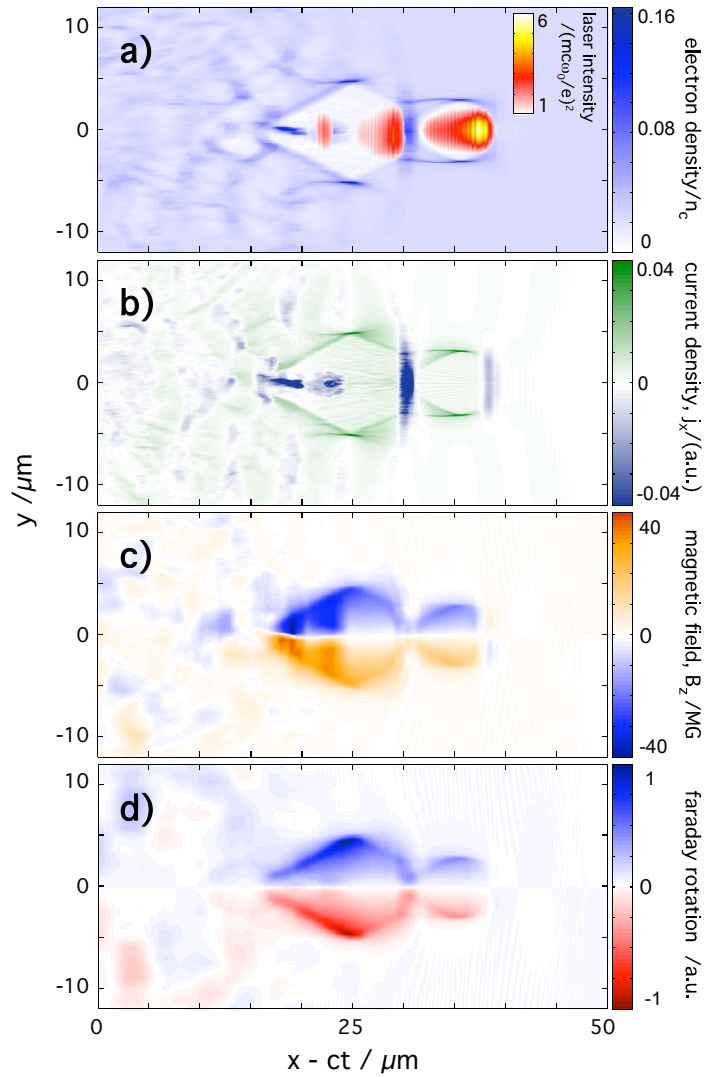
Figure 4.8: Results of the PIC simulation. Shown are following quantities for a snapshot of the simulation: (a) the electron density n_e (bluish) and laser intensity (red-yellow), (b) the longitudinal current density j_x, (c) the azimuthal magnetic field B_z and (d) the subsequent Faraday rotation. Image courtesy of S.P.D. Mangles.

Figure 4.9 shows the temporal evolution of the magnetic field, both from simulation and experiment, as function of the coordinate in the gas jet. The gas density profile is shown as dashed line. From the simulations, the total magnetic field is shown as solid line and the fraction generated by trapped electrons ($p_x > 7\,\mathrm{MeV/c}$) as circles. The experimentally determined values are shown as squares. The qualitative behavior of the measured time-dependency is well reproduced by the simulation. The temporal evolution, especially the steep onset, is strongly correlated with the current of trapped electrons. But both the electron current and the displacement current contribute to the magnetic field with comparable orders of magnitude.
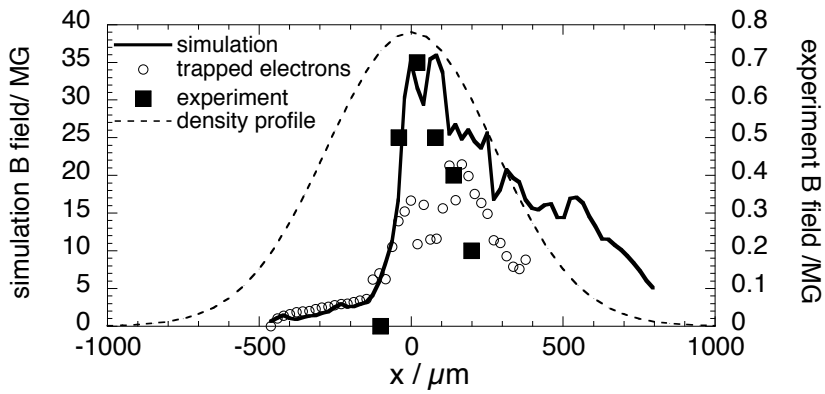
Figure 4.9: Temporal evolution of the magnetic field in total (thick solid line) and the contribution only by trapped electrons (circles) as result of the simulation. The gas density profile is shown as dashed line and the experimentally derived magnetic field (squares). Image courtesy of S.P.D. Mangles.

However, the amplitudes of the magnetic fields as well as their dimensions differ for simulation and experiment. This is mainly caused by different resolutions of the simulation and the experiment, but might be also caused by the 2D geometry of the simulation of a 3D experiment. From the simulations, a snapshot is used in order to calculate the magnetic field. In reality the probe beam and the main laser pulse move with speed of light perpendicular to each other. Furthermore, the spatial resolution of the setup was about $15\,\mu$m due to an aperture in front of the imaging lens in order to dim the intensity of the self-emission. If appropriate filters for motion blurring and spatial resolution are deployed, the simulation yields correct values and radial distributions. Hence, amplitude and spatial width of the magnetic field as shown in Figure 4.7 arise merely from the optical imaging resolution. It should be noted that these measurements represent the first direct observation of the acceleration process with high spatial and temporal resolution [23].

4.2.5 Conclusions

The results of plasma diagnostics, i.e. observation of nonlinear Thomson-scattering, of wave-breaking radiation and of azimuthal magnetic fields, draw a very coherent picture of the acceleration process. As supposed in Sec. 4.1.2, the laser pulse undergoes both self-focusing and self-modulation. The interaction is at least $500\,\mu$m long since this is the length of the region emitting Thomson-scattered light. This is much longer than the Rayleigh length of the focusing mirror, see Table 4.1. In the plasma channel, self-modulation takes place which shortens the laser pulse. Subsequently the intensity is high enough in order to drive plasma waves so strongly that wave-breaking occurs. Electrons are consequently accelerated, being accompanied by azimuthal magnetic fields. Both wave-breaking and azimuthal magnetic fields were observed in the experiments, and the self-modulation process was studied by PIC-simulations which reproduce the experimental results. This picture of electron acceleration – self-modulation ending up in the Bubble regime – is substantiated by the results from the electron beam diagnostics insofar as collimated electron beams with monoenergetic spectra were observed.

4.3 Electron beam properties

Laser-plasma interaction and electron acceleration are nonlinear processes. Single laser shots do not produce identical electron beams since fluctuations of the laser beam profile, energy and wavefront may occur and the gas jet exhibits a turbulent flow. Therefore, shot-to-shot fluctuations cannot be avoided and a statistical approach of data analysis is reasonable.

4.3.1 Spatial characteristics

Figure 4.10 shows electron beam profiles obtained with a scintillating screen from 16 consecutive laser shots. Those were produce when the $f = 50\,$cm parabolic mirror and the supersonic gas jet were used. The gas jet position and timing parameters were optimized for frequent occurrence of collimated beams. The relative frequency of occurrence for well-collimated beams like in the upper left corner picture is $9/16 = 0.56$. As can be seen, shots without significant charge or with a "cloudy" appearance may also occur as well as shots producing multiple collimated beams. In the following, such single electron beam profile images were averaged in order to reduce the shot-to-shot fluctuations.
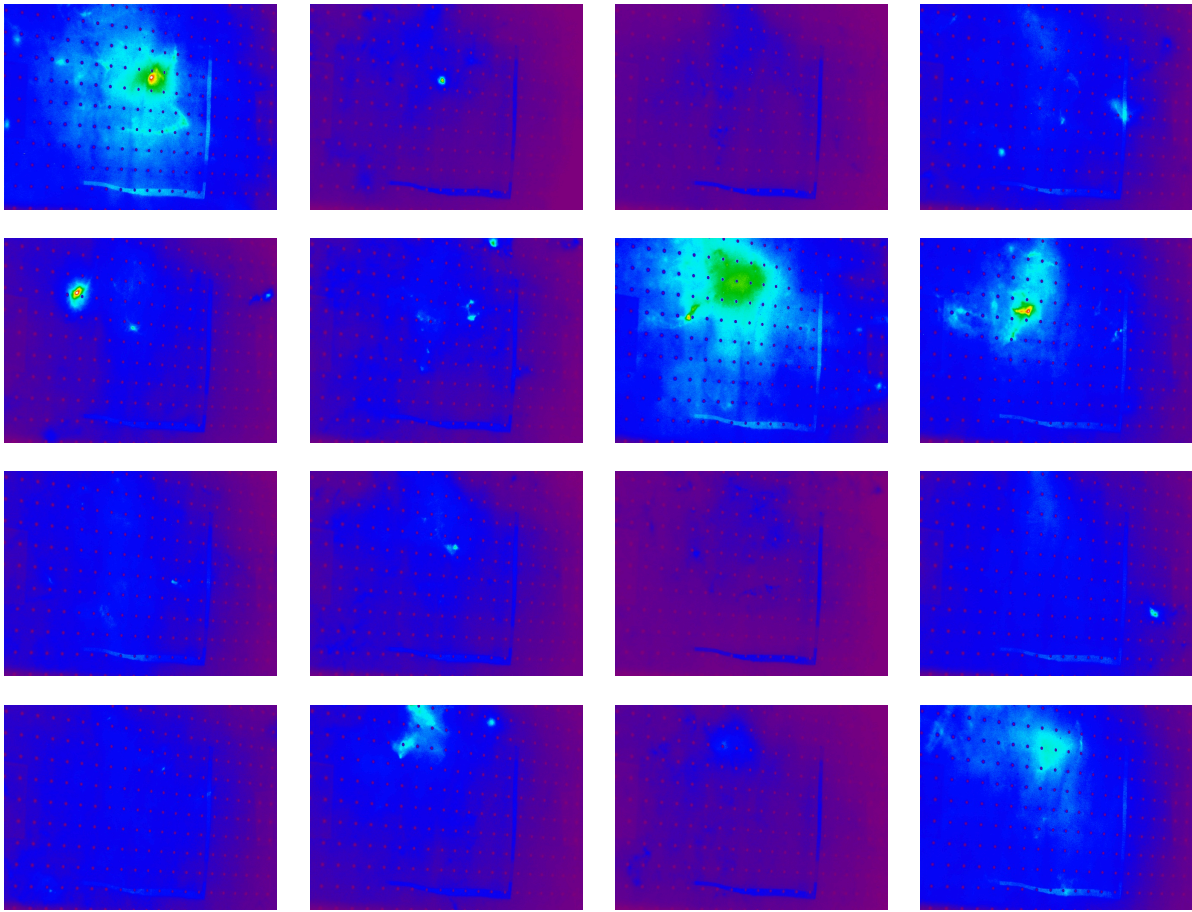
Figure 4.10: Example sequence of electron beam profiles. Shown are 16 consecutive shots for identical parameters at an optimized regime.

Dependence on gas jet position

Typically, the gas jet is hit centrally (X=0) by the laser at a certain longitudinal position Z and vertical distance Y. Then, scans in the z-direction are carried out for certain heights. Import for understanding and modeling the laser-plasma interaction is the absolute distance between gas jet and vacuum focus (focus without plasma). The vertical distance can be measured from shadowgrams where the nozzle is visible. The condition X=0 is usually set via the brightest emission of Thomson-scatterered light. This method has sufficient precision and was checked via an observation from above, similar to the transverse observation. The distance in laser propagation direction can only be determined in a separate experiment via a Hartmann aperture in the main beam. The accuracy of all those methods is about $50\,\mu$m.

A typical result of such scan is shown in Figure 4.11. Positive values for the z-position
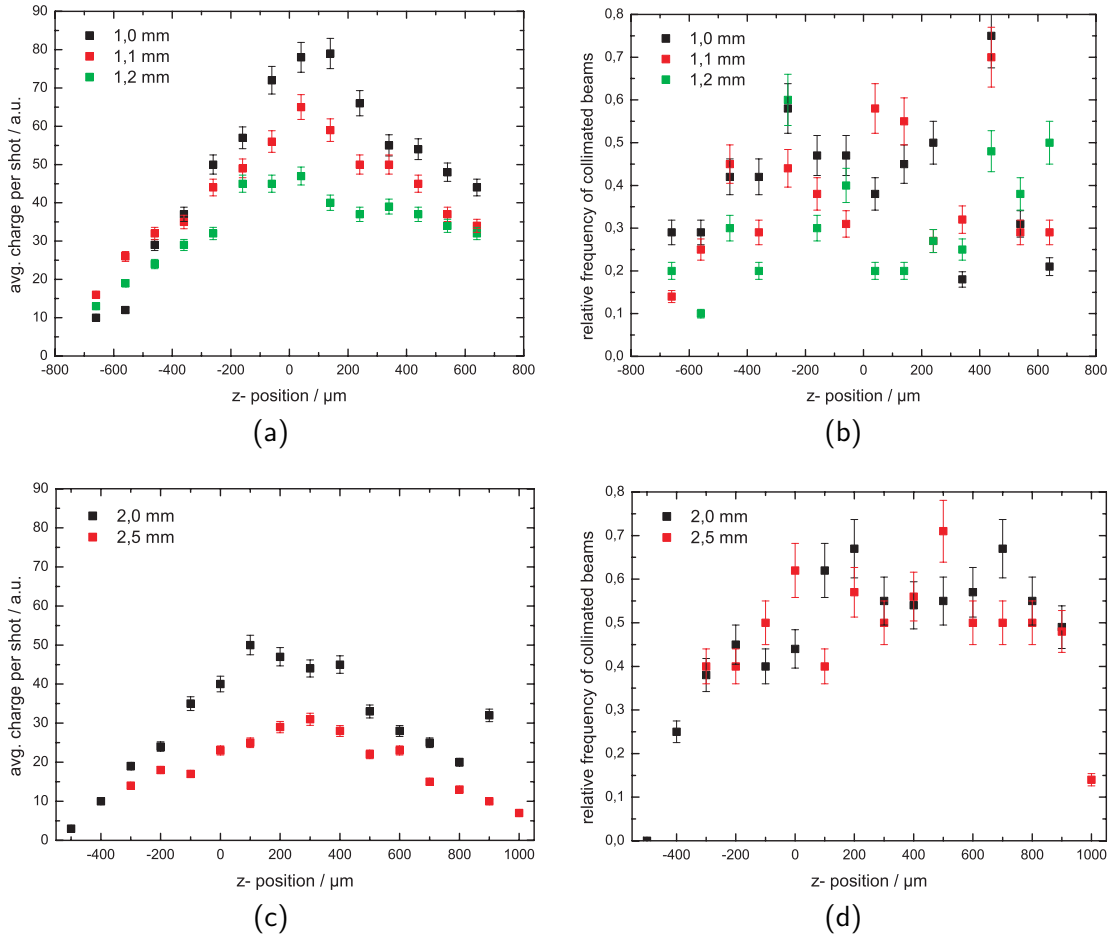
Figure 4.11: Optimizing the gas jet position. Shown are for given longitudinal (Z) and vertical (Y) distances the average charge per shot and the relative frequency for well-collimated beams for the subsonic nozzle, (a) and (b), and the supersonic nozzle, (c) and (d), respectively. The graphs are equally scaled for direct comparison of the nozzles. All data was taken with the $f = 50$ cm parabolic mirror.

indicate that the vacuum focus is behind the gas jet center. This facilitates reading the plots: One has to imagine the gas density profile (Fig. 3.3) superimposed with its center at z = 0. The laser is incident from the left and the vacuum focus is placed at the abscissa position of the corresponding data point. At each position, 10 to 20 shots were carried out and the aiming screen images were averaged. From such average image, the integral pixel count is a measure for the average charge per shot, and from the average distribution the mean direction of electrons can be inferred. The charge is plotted in Figure 4.11 (a) for the subsonic and (c) the supersonic nozzle. Furthermore, from the single aiming screen images of each position, the relative frequency of well-collimated beams can be counted and plotted in the same manner, see Figures 4.11 (b) and (d).

Then, the optimum position can be found, either for high average charge or frequent occurrence of well-collimated beams.

The general behavior of such scan is that a too small vertical distance (and therefore a high peak gas density, cf. Fig 3.3) leads to a higher charge but less frequently collimated beams. The increased charge is distributed in a considerably large cone of about 30 mrad full opening angle. In the longitudinal direction, an optimum can be found slightly behind the point where the vacuum focus coincides with the gas jet center. Hence, the laser has to propagate quite long through the plasma even before it is focused by the parabolic mirror.

As can be seen from Figure 4.11 (a) and (c), the subsonic nozzle produces in general a higher charge with roughly the same gas density. The occurrence of well-collimated beams is comparable but the supersonic nozzle (d) shows less "chaotic" dependencies on the z-position than the subsonic nozzle (b). All shown data is taken from shots with the $f = 50\,\mathrm{cm}$ parabolic mirror. Similar measurements with the shorter focal length exhibit similar behavior and are therefore not shown. Thus it is experimentally found that the impact of the gas jet type is much stronger onto the produced electron beams than the influence of different focal lengths.

Distribution of well-collimated beams

Besides the frequentness of well-collimated beams, they may also be characterized in terms of size and distribution. The pointing behavior is shown in Figure 4.12. Shown are the positions of well-collimated beams on the scintillating screen in a distance of 30 cm behind the nozzle for both the subsonic nozzle (a) and the supersonic gasjet (b). The nozzle positions corresponding to Fig. 4.11 are $1.2\,\mathrm{mm}$ and $640\,\mu\mathrm{m}$ for the subsonic nozzle and $2.5\,\mathrm{mm}$ and $400\,\mu\mathrm{m}$ for the supersonic nozzle. The origin indicates the on-axis direction. A deviation of 3 mm corresponds to an angle of 10 mrad. As can be seen, the beams propagate in average along the on-axis direction but with a mean deviation of about 20 - 40 mrad. The supersonic nozzle produces electron beams with less pointing jitter. However, the difference to the subsonic nozzle is small.

A more detailed analysis is presented in Figure 4.13 (a). The radial distribution of electron beams is shown there for intervals of 10 mrad. The number of beams per bin is normalized by the overall number of beams and the area of the annulus relative to the central circle area. Here it is more clear that the supersonic nozzle (A) produces beams propagating closer to the axis. In contrast, the beams produced with the subsonic nozzle (B) are distributed with a blind spot on axis. In Figure 4.13 (b) is additionally
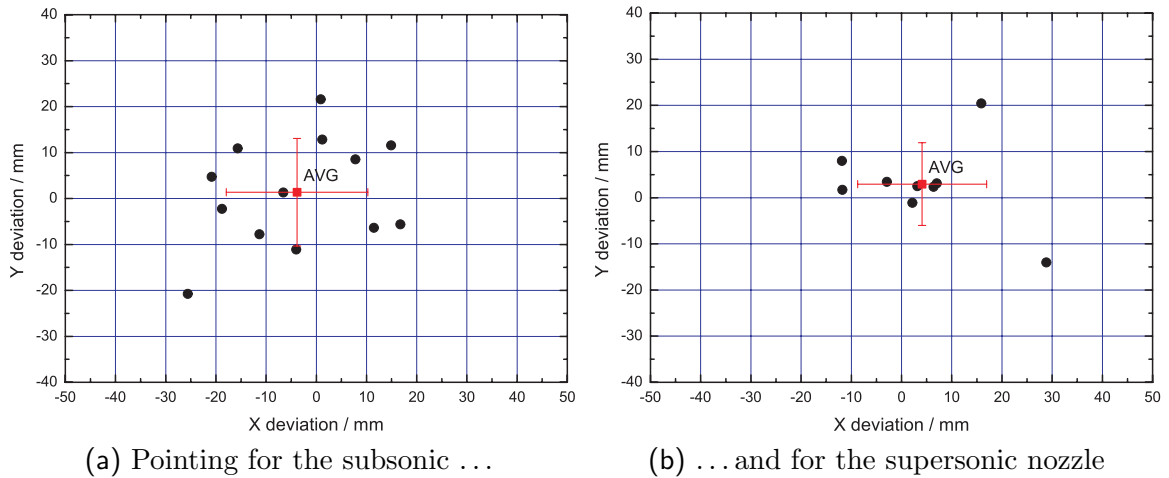
(a) Pointing for the subsonic ...   (b) ... and for the supersonic nozzle

Figure 4.12: Pointing of well-collimated electron beams produced with (a) the subsonic and (b) the supersonic nozzle. Shown are positions on the scintillating screen at optimized nozzle positions. The origin corresponds to the on-axis direction. Red is shown the average position with the standard deviation. 3 mm on the screen correspond to an angle of 10 mrad.

shown the pointing scheme when electron beams were produced in order to generate synchrotron radiation. At that time a supersonic nozzle was deployed in combination with the $f = 30$ cm parabolic mirror, and more data was taken. The radial distribution of that data set, (C), has a blind spot on axis like the one of the subsonic nozzle (B). But for a larger number of shots, the pointing was sufficient in order to produce beams propagating on axis. Thus, the blind spot visible in the distribution of about 20 shots is probably an illusion due to insufficient data for good statistical analysis.

(a) Radial distribution

(b) Pointing during undulator shots
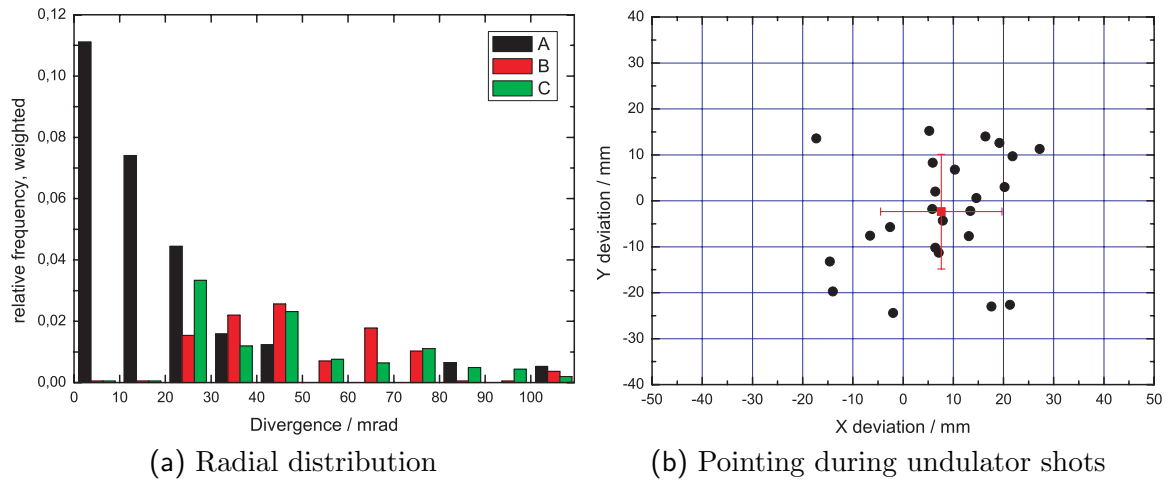
Figure 4.13: (a): Radial distribution of electron beams for the supersonic nozzle (A), subsonic nozzle (B) and during the synchrotron radiation campaign (C). The radial deviation of electron beams from (b) and Figure 4.12 is counted in classes of 10 mrad, normalized by the number of beams and weighted by the area of the corresponding annuli in units of the central circle. (b): Pointing of well-collimated beams during the synchrotron radiation campaign.

Divergence of well-collimated beams

Finally, single electron beams can be analyzed regarding their divergence. Figure 4.14 shows profiles through well-collimated beams produced with the subsonic (a) and supersonic nozzle (b). Obviously, electron beams produced with the supersonic gas jet show a smaller divergence and a better contrast to the background signal. The difference to the subsonic nozzle is small, however. The best collimated beam (the red curve in Figure (b)) has a divergence of 2 mrad. This is already close to the resolution of the scintillating screen. This is the smallest value from the observations, a typical value for typical beams is a factor of 3 larger.
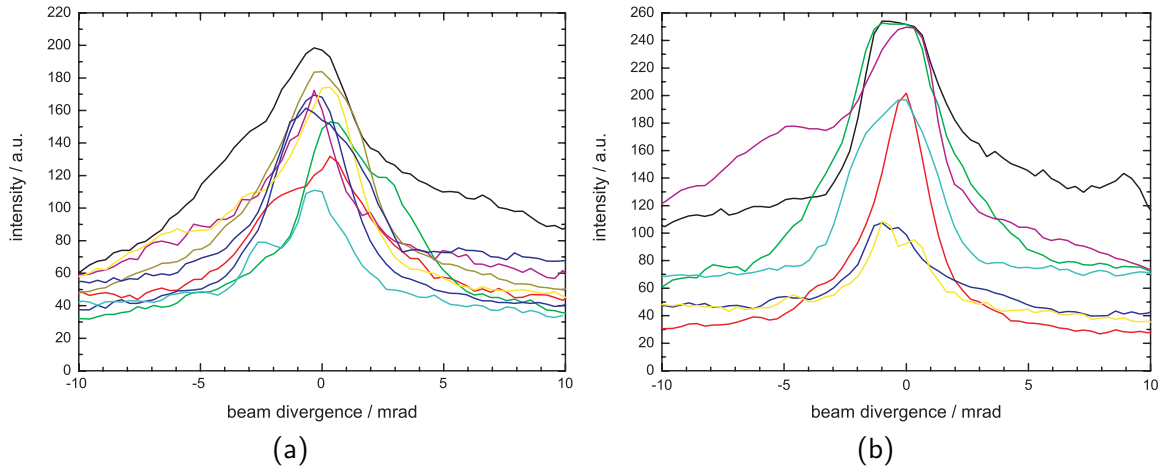
Figure 4.14: Divergence of electron beams for the subsonic (a) and the supersonic nozzle (b).

4.3.2 Spectral characteristics

Electron spectra were primarily recorded during shots through the undulator since it was essential to measure electron spectra for this particular experiment. The results of the previous section lead to the expectation that lots of laser shots ($\sim 100 - 1000$) are necessary to measure a proper number of spectra which in turn is desirable for significant conclusions. However, electron spectra were more often measured than expected from the spatial distribution of well-collimated beams. Thus, also electrons contributing to the cloudy background on the scintillating screens can be measured with the spectrometer. In addition, those electrons may also have monoenergetic features which was not anticipated.

Figure 4.15 shows typical electron spectra. Shown are raw images from the scintillating screen of the electron spectrometer and the corresponding calibrated spectra. Note that the shadow in the left part of each image is caused by the frame for the imaging plate. The energy range shown in the spectra corresponds to the part right of the shadow.

Shot (a) occurs as exponential spectrum, in this case quite intensive and therefore ranging to comparably high energies. However, the raw image reveals that the charge at energies below 20 MeV is less than for energies above 20 MeV. Shot (b) shows a typical monoenergetic spectrum at 50 MeV. The bandwidth shown in the spectrum is about 4 MeV FWHM. However, this value is a mixture of actual energy spread, actual horizontal beam size and focusing of the spectrometer. A look at the raw image shows that the horizontal beam size (which appears as energy spread) is roughly the same as the vertical beam size. From the beam profile measurements it is a reasonable assumption
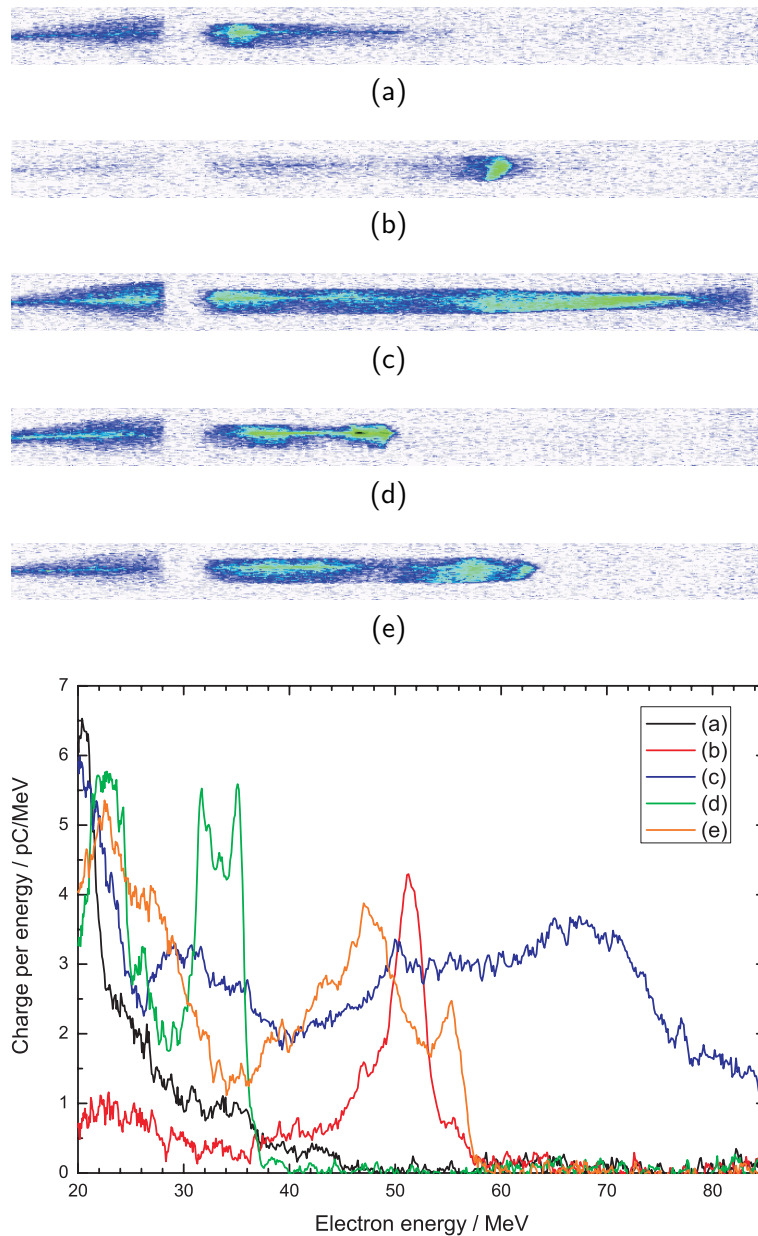
Figure 4.15: Typical electron spectra, as raw data from the scintillating screen of the spectrometer (a)-(e) and as calibrated spectra. The gap in the left part of each image is caused by the frame of the image plate which was used for absolute calibration and ranges from 16 MeV to 20 MeV. Energy is increasing toward the right side.

that the beam is at the entrance into the spectrometer circular symmetric. Hence, the actual energy spread is presumably much smaller than 4 MeV but cannot be determined more accurately. This set of problems was already discussed in Sec. 3.4.3 and is now illustrated. Spectrum (c) is very broad, which is a seldom event. In fact, it reaches the high-energy limit of the scintillating screen which is at 85 MeV. Shots (d) and (e) show

multiple monoenergetic contributions in single shots. This is also a typical behavior.

From shots through the undulator, numerous electron spectra were recorded. They were categorized into exponential, monoenergetic, empty and irregular (mixed) spectra. Out of a typical set of 200 laser shots, only 29 shots produced almost no electrons detectable by the spectrometer, either caused by insufficient charge at all or collimated beams propagating off axis. Other 33 shots showed exponential spectra which usually extended to 20 MeV - 25 MeV. 47 shots were dominated by monoenergetic features, and the residual 91 shots are irregular. Hence, about every fourth shot is monoenergetic, but with arbitrary charge and peak energy.
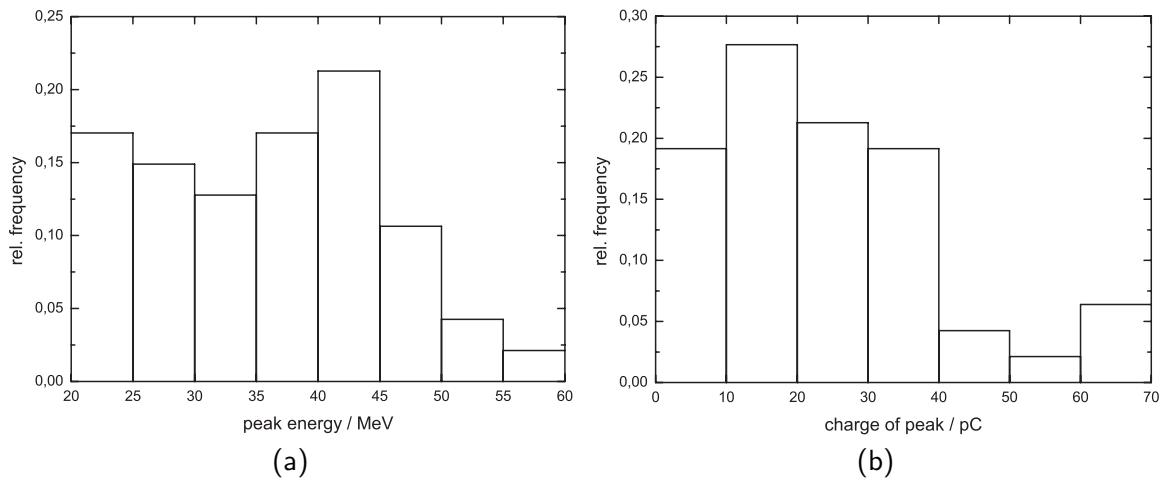
Figure 4.16: Distribution functions for monoenergetic electron spectra.

The monoenergetic spectra were analyzed further. Figure 4.16 shows the energy and charge distribution function of 47 shots producing monoenergetic spectra. The energy distribution, Fig. 4.16 (a), decreases for increasing energy but has a peak at the 40 MeV - 45 MeV range. However, the distribution from 20 MeV to 45 MeV is roughly constant. The charge distribution, Fig. 4.16 (b), is also roughly constant up to 40 pC. Higher charges of a monoenergetic peak are rare. Note that there is no correlation between charge and energy.

4.3.3 Comparison to conventional accelerators

Transverse emittance

The smallest measured beam divergence is 2 mrad (half opening angle, σ'). In order to determine the transverse emittance of laser-produced electron beams, the source size

must be known, too. This is difficult to measure and can to date only be estimated from simulations and theory. A reasonable dimension is the plasma wavelength which is an upper limit.

In the experiments, the plasma wavelength at maximum gas density is $\lambda_{\mathrm{p}} \approx 6\,\mu$m. A good estimate for the electron beam diameter is half the plasma wavelength, the beam radius might be $\sigma \sim 2\,\mu$m. Thus, the transverse emittance of the produced electron beams is $\varepsilon_\perp \geq 10^{-5}\,\mathrm{mm}^2\mathrm{mrad}^2$. This corresponds to a normalized transverse emittance of $\varepsilon_n = \gamma\beta\sqrt{\varepsilon_\perp} \sim 0.1\,\mu\mathrm{m} - 0.5\,\mu\mathrm{m}$ for the obtained electron energies of up to $\sim 70\,\mathrm{MeV}$.

In comparison with recent developments for low-emittance electron guns at conventional accelerators [77], the transverse emittance of laser-produced electron beams is one order of magnitude lower. The source size on the order of one micron is similar, but since the electrons are confined in the bubble and become rapidly accelerated, transverse space charge effects are effectively inhibited which usually limit the transverse emittance at conventional accelerators. This, however, comes into play for free propagation of laser-accelerated electron bunches.

Longitudinal emittance and peak current

The longitudinal emittance of electron beams can again only be estimated. The energy spread of electron beams is difficult to determine due to the energy resolution issues of the spectrometer (cf. Sec. 3.4.3). The narrowest-peaked electron spectra show a width of 2 MeV.

Bunch duration measurements are difficult to perform for laser-plasma accelerators [78]. The general findings are [54, 55, 56] that the bunch is shorter than 50 - 100 fs, and simulations suggest a bunch duration of a few femtoseconds [19]. Thus, a rough estimate of the longitudinal emittance is $\varepsilon_{||} \sim 10\,\mathrm{keVps}$.

With regard to a FEL driving accelerator, the peak current plays an important role besides the transverse emittance (cf. Eq. (2.50)). Arnold *et al.* describe the design of an electron gun for the use in FEL, obtaining a charge comparable to the one of the observed laser-generated electron beams. At FLASH in Hamburg, Germany, the bunch charge is 0.5 - 1 nC which is significantly higher [5]. Assuming bunch durations as predicted by simulations ($< 10\,\mathrm{fs}$), the current of a laser-plasma accelerator is comparable or higher than for conventional guns. If a short pulse duration is of interest, laser-accelerated electron bunches promise to be the first choice.

5 Synchrotron radiation from laser-accelerated electrons

This chapter reports on the detection of synchrotron radiation in the visible spectral range which was generated be laser-accelerated electrons. At first, the setup is presented in order to clarify the detection scheme, before the results are shown, explained and discussed.
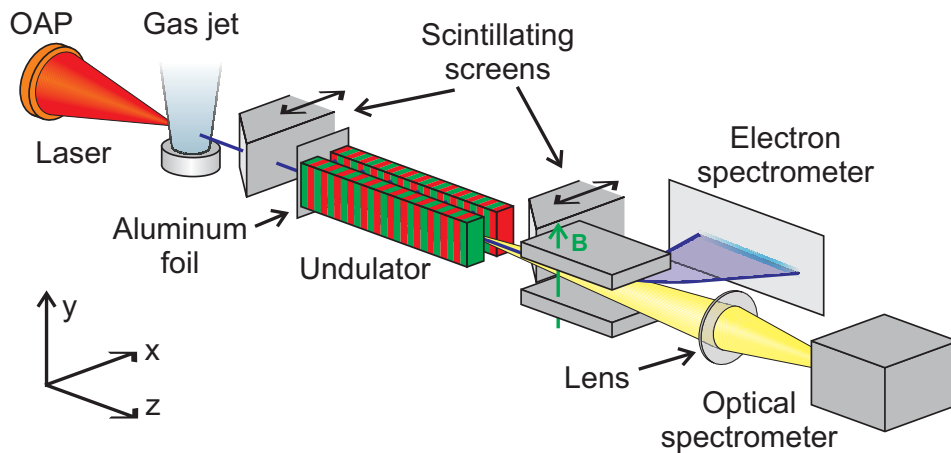
5.1 Experimental setup

Figure 5.1: Schematics of the setup of the full experiment. Electrons are accelerated by focusing the JETI laser pulses into a supersonic Helium gas jet. The relative occurrence and the directionality of electron beams can be monitored in front of the undulator in order to optimize the laser and plasma parameters. If the screen is removed, electrons pass a thin aluminum foil at the entrance of the undulator which screens the laser light. Inside the undulator, synchrotron radiation is produced, which is collected by a lens and detected by an optical spectrometer. Simultaneously, electron spectra can be measured with the electron spectrometer. Alternatively, the electron beams can be also monitored between undulator and spectrometers. The lead aperture in front of the undulator is not shown.

The setup of this experiment is shown in Figure 5.1. The JETI laser pulses were

focused by the $f = 30\,\mathrm{cm}$ off-axis parabolic mirror (OAP) into a supersonic Helium gas jet. Electrons were accelerated and, prior to shots through the undulator, monitored by the first scintillating screen placed 30 cm behind the gas jet. The laser-plasma interaction was optimized for frequent occurrence of well-collimated beams as outlined in Sec. 4.3.1. This was an essential requirement for the production of synchrotron radiation. In order to detect it with the optical spectrometer (560 nm - 990 nm, cf. Sec. 3.5.2), electron beams had to have energies in the range of 55 MeV to 75 MeV, according to Eq. (2.40). Additionally, they had to have sufficient charge in that interval preferably in a monoenergetic peak, but this could not be optimized in advance (cf. Sec. 4.3.2). The electrons then passed a $15\,\mu\mathrm{m}$ thin aluminum foil which screened the optical detection system against the intense laser light and further emission from the plasma. The undulator entrance was in a distance of 40 cm from the gas nozzle. A 1 cm thick lead aperture with 1 cm free diameter protected the magnets of the undulator against off-axis electrons. On-axis electrons passed through the 1 m long undulator, produced synchrotron radiation and were subsequently detected by the electron spectrometer whose entrance was 185 cm behind the gas jet. Simultaneously, the radiation was collected by an AR-coated plano-convex $f = 105\,\mathrm{mm}$, $f/2$ lens, placed 146 cm behind the undulator exit, and then detected by an optical spectrometer. Alternatively, the electron beams which passed the undulator could be monitored with a second scintillating screen. This action, however, blocked both spectrometers.

5.2 Properties of the produced synchrotron radiation

5.2.1 Correlation of electron and radiation spectra

Figure 5.2 shows 3 examples of pairs of electron spectra (a) and corresponding optical radiation spectra (b), i.e. simultaneously recorded spectra from the same laser shots. Identical colors of graphs indicate corresponding data. The gray vertical bars at the electron spectra indicate the energy range of 55 MeV to 75 MeV where undulator radiation would be expected within the spectral range of the optical spectrometer.

The electron spectrum of the red shot is monoenergetic with a peak at 64 MeV, right within the energy range of interest. In addition, it has almost no electrons at lower energies. With the optical spectrometer, a very strong peak at 740 nm was observed. The peak positions agree very well with Eq. 2.40.

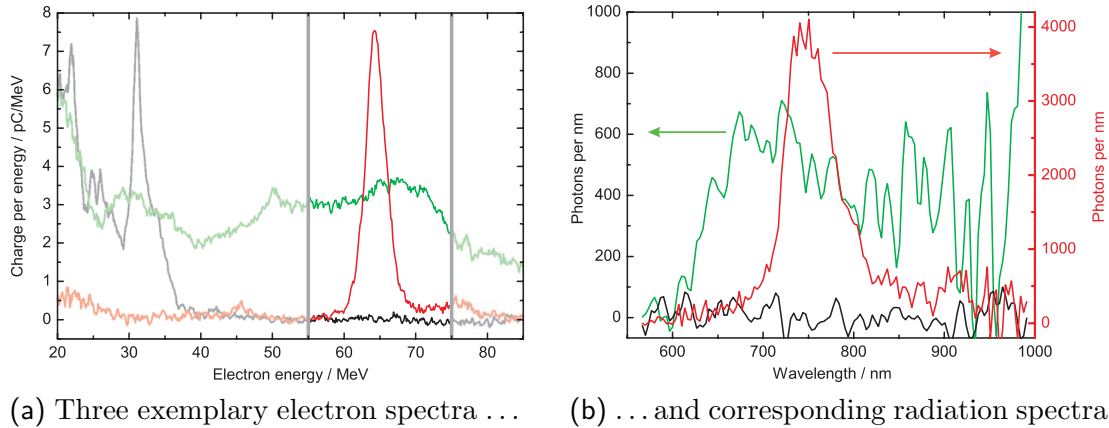The green shot's electron spectrum is broadband, however with a particular spectral

(a) Three exemplary electron spectra ...

(b) ... and corresponding radiation spectra

Figure 5.2: Electron spectra (a) and corresponding optical radiation spectra (b) for 3 exemplary shots. The vertical grey bars in graph (a) indicate the range of electron energies (55 MeV - 75 MeV) where undulator radiation would be within the range of the optical spectrometer (560 nm - 990 nm). The right-hand-side ordinate in graph (b) is for the red shot.

shape in the detection range: slowly increasing toward a peak at 67 MeV (slightly above the peak energy of the red shot) and then a steeper decrease. The corresponding optical spectrum shows a similar spectral shape with a corresponding peak position (at wavelengths slightly lower than for the red shot) is observed with the optical spectrometer. Note that the noisy part of the spectrum at wavelengths above 800 nm arises from the quantum efficiency correction of the spectral data.

The electron spectrum of the black shot shows a peak as strong as for the red shot but at 30 MeV electron energy but no electrons at other energies, especially not in the range of interest. Hence, according to Equation 2.40, synchrotron radiation is expected around $\lambda \approx 3\,\mu m$ which is far beyond the detection range of the optical spectrometer. Indeed, no optical radiation was detected for this shot.

A more precise data evaluation was carried out with the help of simulations as described in Sec. 3.5.3. Fig. 5.3 uses again the red displayed shot from Fig. 5.2. It shows as inset the electron spectrum, which is peaked at 64 MeV, has a width of 3.4 MeV (FWHM) and contains a charge of 10 pC. Optical radiation (red) is peaked at 740 nm and has a bandwidth of 55 nm. The total number of photons within the linewidth is about 280,000. Based on the electron spectrum, the undulator radiation spectrum was simulated according to Sec. 3.5.3 and is displayed as green line in Fig. 5.3. It shows an excellent agreement with the measured undulator radiation in terms of spectral distribution, width and photon numbers. The slight offset of the peak positions is negligible in consideration of the uncertainty for electron spectrum peak positions.
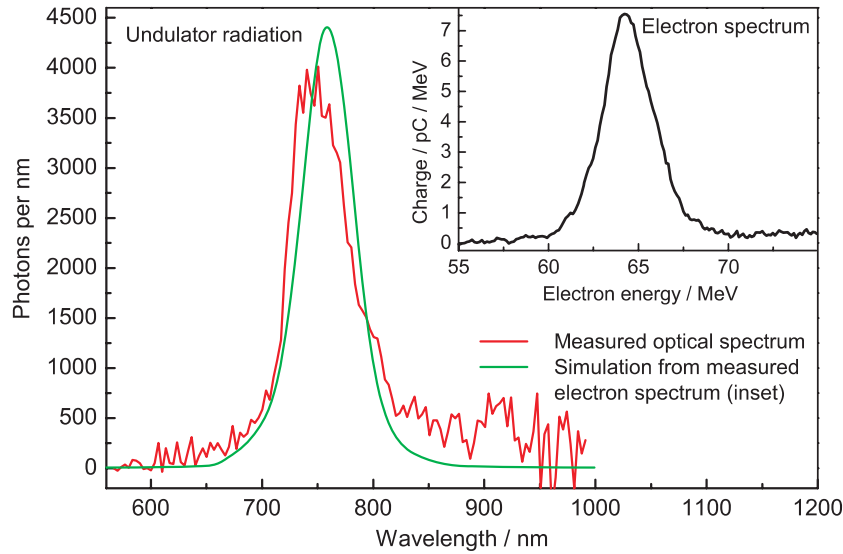
Figure 5.3: Measured optical radiation spectrum (red) and simulated undulator radiation spectrum (green) which was calculated from the corresponding electron spectrum (inset).

5.2.2 Second harmonic undulator radiation

Several of those shots were recorded, showing similar behavior of matching peak energies and wavelengths according to Eq. 2.40. All shots which exhibit a spectral charge density greater than 1 pC / MeV in the range of 55 MeV to 75 MeV, produced a signal on the optical spectrometer. Vice versa, each shot with a signal on the optical spectrometer shows a corresponding intense peak in that energy range, except a few shots which show a even higher charged peak in the range of 40 MeV - 50 MeV. Those shots produced second harmonic undulator radiation which is for those energies in the detection range of the optical spectrometer. For these shots, the electron spectral intensity had to be above 7 pC / MeV in order to produce a detectable optical signal which is a rare event. The recorded second harmonic spectra are indeed very faint with a typical signal-to-noise ratio SNR < 2 and are therefore not shown.

This behavior is consistent with simulations of undulator radiation with SPECTRA, based on the actual undulator parameters, which exhibit an intensity ratio of 10:1 for fundamental to second harmonic undulator radiation. This ratio can be seen in Figure 6.1. Hence, in order to produce a detectable second harmonic signal, the spectral charge density has to be 10 times larger than for fundamental radiation.

5.2.3 Wavelength scaling

Fig. 5.4 displays the correlation between electron spectrum peak energy and optical radiation peak wavelength for all shots which produced synchrotron radiation. All shots
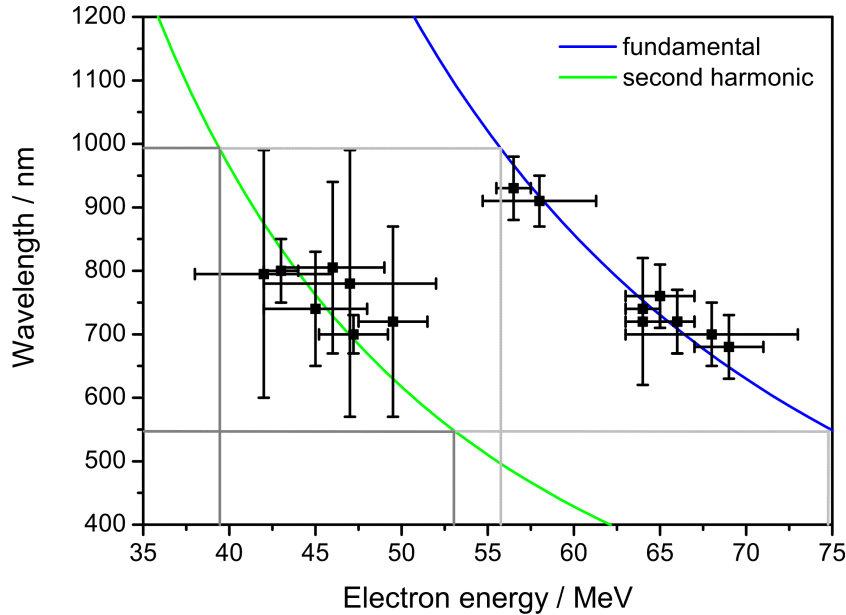
Figure 5.4: Correlation between measured electron spectra peak energies and undulator radiation spectra peak wavelengths. The solid lines display the theoretical relation between electron energy and undulator radiation wavelength according to Eq. 2.40 for the fundamental (blue, $n = 1$) and second harmonic (green, $n = 2$). The grey bars arise from the detection range for optical radiation (560 nm - 990 nm) and guide to ranges for electron energies where electrons should produce an optical signal. Note: The error bars do not show an error in the sense of an uncertainty but the width of the electron and optical spectrometer signal, respectively.

displayed in Fig. 5.4 fit well whether to fundamental undulator radiation (blue line) or second harmonic (green line). It must be noted that there were no shots with an optical signal but without a corresponding electron spectrum, and vice versa.

5.3 Discussion

5.3.1 Exclusion of other possible sources

Further sources of light which possibly could have been detected by the spectrometer are excluded as follows. Direct laser light, plasma emission and transition radiation from the plasma-vacuum boundary [79] are completely blocked by the aluminum foil in front

of the undulator. Furthermore, tiny leakages in the foil would easily be revealed by the laser light as the most intense fraction.

Only transition radiation being emitted when the electron beam exits the 15 μm aluminum foil used to block the spectrometer from optical light from the interaction region is a conceivable source of disturbing light. Transition radiation occurs if a electrons cross an interface where the dielectric function varies [72]. The interaction of the current with the boundary generates broadband radiation. However, for wavelengths longer than the bunch length, a coherent superposition results and increases the intensity for such wavelengths. For coherent transition radiation at wavelengths detectable by our spectrometer, the bunch duration would have to be shorter than 3 fs. Furthermore, if there is a periodical modulation on the longitudinal structure similar to micro-bunching in a FEL (cf. Sec. 2.4.2), such coherent transition radiation is produced as well, leading to increased intensities at wavelengths given by the periodicity. Recently, coherent transition radiation from laser-accelerated electrons at wavelengths from 400 nm to 1 micron was observed [80]. The laser pulse interacts with the laser-accelerated electrons during the acceleration process and imprints its periodicity. But this impression is washed out with increasing distance between laser-plasma accelerator due to space charge effects of the electron bunch. Referring to [80], in our case of 400 mm distance between acceleration region and aluminum foil, the imprint of the laser is faded.

Thus, in the wavelength range of our spectrometer, only incoherent broadband transition radiation may be produced, unable to explain neither the correlation between electron spectrum peak energies and optical spectrum peak wavelengths for various shots (Fig. 5.2 and Fig. 5.4) nor the agreement between simulated and measured spectrum (Fig. 5.3). In addition, in contrast to undulator radiation, transition radiation is emitted into lobes separated by an angle $\vartheta \sim 1/\gamma$ with zero intensity on axis. Hence, the lens collects transition radiation around its intensity minimum. Furthermore, the imaging of this source onto the entrance slit plane of the optical spectrometer is worse than for undulator radiation. Therefore, the overall signal would be very small.

5.3.2 Comparison to conventional facilities

The detected radiation may be also expressed as spectral peak brilliance according to Sec. 2.4. The most intense observed shot, see Fig. 5.3, contains 280,000 photons in a peak of 55 nm bandwidth (FWHM). The source is an electron beam of 4 mm size and 2 mrad divergence which is a reasonable estimate from the width on the electron spectrometer screen. The pulse duration of 10 fs must be assumed due to a lack of any

experimental indications. Then, this synchrotron radiation spectrum exhibits a spectral peak brilliance of the order of 10^{16} photons/(s mm^2 mrad^2 0.1% BW).

This order of magnitude is comparable to second generation synchrotron radiation facilities [3]. However, for shorter wavelengths, the radiation output usually increases, which could be accomplished in this case with a shorter undulator period or a different laser-plasma accelerator scheme (see Chapter 6). Furthermore, the electron beam was not focused into the undulator which is always performed at synchrotron radiation facilities. The beam could be focused with magnetic lenses (quadrupoles) at least to a diameter of $\sim 100\,\mu$m which would result in an increase of the spectral brilliance of 3 orders of magnitude. However, neither the undulator nor the electron beams were optimized for high spectral brilliance. The goal was to produce and detect synchrotron radiation from laser-accelerated electron beams for the first time. The visible spectral range was chosen due to the availability of sensitive spectrometers in this range. The undulator was especially designed for available electron energies which also come along with low significant pointing jitter. No further electron beam management like focusing can be deployed under those circumstances. Therefore, the result of a spectral peak brilliance comparable to second generation facilities is quite encouraging.

5.3.3 Estimated pulse duration

The observed radiation was in all cases incoherent synchrotron radiation. As discussed in Sec. 2.4.2, a coherent superposition of the radiation of all electrons can occur if the electron bunch is significantly shorter than the wavelength of the produced radiation, or if micro-bunching occurs. Therefore, the pulse was not short enough in order to produce coherent radiation. Simulations for different pulse lengths but with the measured electron spectra show that the electron pulse was longer than 3 fs. This is also the lower limit for bunch durations from laser-plasma simulations [19].

6 Summary and outlook

6.1 Summary

In the course of this work, a laser-plasma accelerator was set up which uses a 10 Hz, 85 fs, 10 TW table-top laser system and a gas jet as target. The plasma density profiles were optimized for the frequent generation of well-collimated, multi-MeV electron beams. The obtained high-quality electron beams were passed through an undulator where synchrotron radiation was produced for the first time with a laser-accelerated electron pulses. The optimization of the electron beams was obtained by careful moving the gas nozzle with respect to the laser focus and several online observation techniques which allowed for immediate control and feedback.

The region of the laser-plasma interaction was imaged onto a camera. Nonlinear Thomson-scattered light, which is an indicator for self-focusing and self-modulation of the laser pulse, and also wave-breaking radiation which is directly coupled to electron beam production (see Sec. 4.2.1) were observed. Furthermore, the interaction region was analyzed with an ultra-short transverse probe beam which allowed for time-resolved investigations. Interferograms (Sec. 4.2.2) and polarograms (Sec. 4.2.3) were recorded which show the electron density evolution and the occurrence of azimuthal magnetic fields which are associated with electron acceleration. Polarograms were detected with two polarizer-camera pairs which allowed for the detection of Faraday rotation of the probe beam polarization as small as 0.1°. The experimental results are confirmed by PIC-simulations (Fig. 4.8) which show the formation of two bubble-like wakefield structures due to strong self-modulation of the laser pulse, subsequent electron trapping and acceleration. The observed azimuthal magnetic fields, especially their characteristic temporal evolution (Fig. 4.9), are closely related to electron trapping and acceleration. Therefore, these results represent the first direct observation of bubble formation and electron acceleration with unprecedented high spatial and temporal resolution.

Electron beam images were recorded which allowed for online feedback to the gas jet position and further plasma parameters. The dependency of electron beam profiles and

their directionality on the plasma target parameters was studied (see Sec. 4.3.1). Electron beam profiles were optimized to frequent occurrence ($\sim 70\%$) of collimated beams (divergence < 5 mrad). The mean pointing jitter was about 30 mrad. The supersonic nozzle produced slightly better electron beams in terms of stability and divergence than a subsonic nozzle. No observable difference was found whether a $f = 30$ cm or a $f = 50$ cm parabolic mirror was used.

Electron energy spectra (see Sec 4.3.2) show monoenergetic features in 25% of the shots. Electron energies up to 80 MeV were observed with charges of serveral 10 pC and spectral bandwidths of 3 MeV - 10 MeV. No correlation between energy and charge was found.

The produced electron beams were passed through a 1 m long undulator where they produced incoherent synchrotron radiation. The radiation was in the visible spectral range due to electron energies, the undulator and the detection system. Radiation spectra and electron spectra were recorded simultaneously in order to identify the synchrotron radiation and exclude other possible sources. Synchrotron radiation was observed and unambiguously identified with help of simulations from the actual electron energy spectra. Since only incoherent radiation was detected, the electron pulses are longer than 3 fs which is in accordance with simulations.

Due to the acceleration regime of complex interaction between plasma and laser pulse, electron beams showed considerable fluctuations regarding their direction and energy spectrum. If the best observed properties are combined, the laser-produced electron beams have a smaller transverse emittance than conventionally accelerated electron beams. Furthermore, taking the ultra-short pulse durations as predicted by simulations, the peak current of laser-accelerated electron bunches is at least comparable to conventional accelerators. The pulse duration, however, is much shorter.

Hence, future applications of the described scheme of producing synchrotron radiation with laser-accelerated electrons are not too far away. Primarily, the beam production and pointing jitter must be reduced in order to produce radiation by every shot. Then, a beam focusing could be deployed which would increase the brilliance of the source drastically. Secondly, higher energies should be produced with high reproducibility and, furthermore, reduced energy bandwidth. This will lead to shorter wavelengths and stable and narrow spectra. An increase of the bunch charge would also be beneficial, however it could lead with the short pulse durations to increased beam divergence.

In the following, current developments in the field of electron acceleration with intense lasers are described. Different target designs and injection mechanisms are presented

but only those which have the potential of reduced pointing jitter and higher electron energies. Then, based on those recently achieved results of other groups, possible laser-based synchrotron radiation sources are discussed as well as aspects of such sources which are unique and could make them superior over conventional ones.

6.2 Ways to improved electron acceleration

The actually deployed laser-plasma accelerator relies on nonlinear interaction and feedback between laser pulse and plasma wave. The laser pulse a) guides itself (self-focusing), is meanwhile b) shortened by the plasma (self-modulation) and can then drive a plasma wave so strongly that c) injection via wave-breaking occurs.

Other groups in the field of laser particle acceleration proposed and demonstrated different experimental setups which produce electron beams more stable. A key feature of all setups is that the laser pulse and its interaction with the plasma are not solely used for all the 3 steps a) - c).

6.2.1 Shorter laser pulses

Many experiments have been carried out at laser facilities with shorter laser pulses, typically $\tau_L \sim 30\,\text{fs}$, where electron energies of a few 100 MeV were obtained from gas jet targets [9, 10, 11, 45]. With initially shorter pulses than at the JETI laser, less interaction length for self-modulation is necessary to shorten the pulse further. Moreover, those laser systems produce comparable pulse energies of $\sim 1\,\text{J}$, but due to the shorter pulse, the power is higher. Consequently, longer focal lengths can be used in order reach relativistic intensities. This was found to be beneficial for stable electron beam generation [73]. In the near future, the LWS10 laser system at MPQ Munich, Germany, will produce sub-10-fs laser pulses of relativistic intensity which can directly access, i.e. without self-modulation, the Bubble regime [81].

6.2.2 Guiding

In addition to self-focusing, external means can be used to counteract diffraction and thereby to prolong the interaction length. Recently, the use of capillary discharge waveguides [82] was successfully implemented [14, 83, 15, 84, 85]. Electron beams of up to 1 GeV electron energy within a beam of less than 2 mrad divergence and with negligible pointing jitter were obtained due to longer acceleration lengths.

This type of plasma waveguide relies on thermal equilibrium of a gas discharge in a narrow capillary. The discharge current ionizes and heats the plasma which is cooled on the walls. Thereby, the temperature in the center rises, the plasma density becomes thinner and a focusing density profile is formed. Via parameter studies [86, 87, 88] it is possible to adapt this concept to different laser systems. Recent studies at the JETI facility [89] show the feasibility but also the complexity of this approach. It should be noted that any external guiding structure is just an additional or assisting feature, since a relativistically intense laser pulse always exhibits self-focusing.

6.2.3 Homogeneous plasma

The above-mentioned guiding experiments use a capillary with two gas injection slots close to the entrance and exit of the capillary. In recent experiments, similar capillaries were used as gas cell [12], i.e. without gas discharge and therefore without external guiding. It was shown that very stable electron beams can be produced with 200 MeV electron energy, 2 mrad divergence and 1.4 mrad pointing jitter. This result is traced back to the plasma density. Between the gas injection slots, i.e. over most of the capillary length, the gas has prior to the interaction a very homogeneous density without any turbulences since there is no gas flow. In contrast, gas jets always exhibit a gas flow where turbulences may be present. Those weak density fluctuations may lead, regarding the nonlinear laser-plasma interaction, to less stable results and shot-to-shot fluctuations.

6.2.4 Triggered electron injection

If the injection of electrons is triggered externally, there is no need to drive the plasma wave so strongly that it reaches the nonlinear regime and the wave-breaking limit. This was shown by Faure *et al.* [13]. In addition to a strong laser pulse, a weak counter-propagating laser pulse is used which interferes with the strong one. A standing wave is formed at the edge of the intense pulse. There, electrons oscillate relativistically in laser propagation direction. A fraction of electrons obtains sufficient energy in order to co-propagate with the plasma wave driven by the strong laser pulse. It was shown that monoenergetic electron beams can be generated. The energy can be chosen by the delay and therefore by the overlap position of the two pulses. The longer the distance to the end of the plasma, the higher the energy.

6.3 Perspectives for laser-based synchrotron radiation sources

In the following, some possible schemes for synchrotron radiation sources based on laser-plasma accelerators are presented. Approaches like incoherent radiation, SASE-FEL or other designs are discussed. Emphasis is put on unique features and advantages over conventional facilities of laser-based approaches.

6.3.1 Incoherent synchrotron radiation

Based on recent results of other groups for electron beams, synchrotron radiation spectra which could nowadays be produced from laser-accelerated electron beams can be computed. Simulations with SPECTRA [52] were carried out, assuming electron bunches
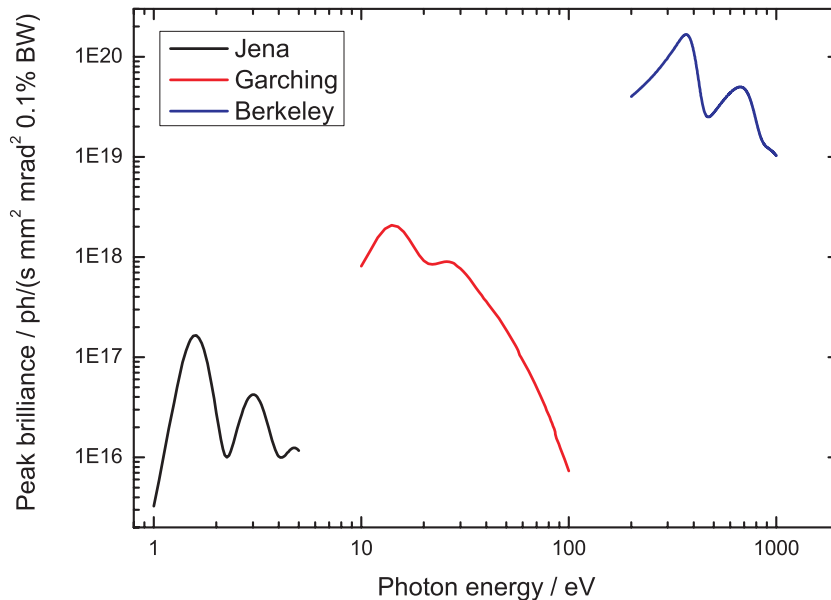
Figure 6.1: Synchrotron radiation based on nowadays available laser-produced electron beams. Shown are spectra of incoherent synchrotron radiation simulated with SPECTRA [52]. For all spectra, the undulator described in Sec. 3.5.1 is considered with an electron bunch of $5\,\mu$m length, $5\,\mu$m diameter and 2.5 mrad divergence. The "Jena" simulation corresponds to the shot of Fig. 5.3, the "Garching" run to [12] and "Berkeley" plot to [14], regarding the underlying electron spectra.

of $16.7\,$fs duration, $5\,\mu$m diameter and 2.5 mrad divergence passing through the Jena undulator (cf. Sec. 3.5.1). Results are shown in Fig. 6.1. The "Jena" run corresponds to the shot shown in Fig. 5.3, centered at 65 MeV with a bandwidth of 5% and 10 pC of charge. "Garching" is based on an electron spectrum peaked at 200 MeV, with 8%

bandwidth and also 10 pC of charge [12]. The "Berkeley" simulation considers a 1 GeV beam with 2% bandwidth and 30 pC charge [14].

The spectra show for all runs the fundamental of undulator radiation but also the second harmonic signal. Photon energies covering the whole EUV range up to 1 keV could be produced with nowadays possible laser-accelerated electron beams. The electron energy spectral width also affects the radiation spectrum. The comparatively large bandwidth for "Garching" leads to a significant smear-out of the fundamental and second harmonic radiation.

6.3.2 SASE-FEL

So far, with electron energies in the 100-MeV to GeV range, VUV and soft x-ray radiation could be produced. But it must be noted that this is incoherent synchrotron radiation. Coherent radiation, which increases the spectral peak brilliance, can only be obtained in the high-gain FEL regime. For the use of pre-bunched electron beams, the electron pulse duration would have to be in the attosecond range.

Considering a laser-driven SASE-FEL, many parameters cumulate. The gain length, given by Eq. (2.51), should be not longer than ~ 1 m in order to keep the undulator small. Therefore, the Pierce parameter, see Eq. (2.50), has to be large. This may be accomplished via the high current density which a laser-accelerated electron bunch has due to its short duration and low transverse emittance, cf. Sec. 4.3.3. However, the mentioned equations disregard electron beam energy spread. To date, the energy spread is a few percent which is too large for that purpose.

Despite those problems, the gain length may be estimated with Eqs. (2.50) and (2.51). Considering again the Jena undulator, driven by a 1 GeV, 50 pC, 10 fs electron beam focused to $20\,\mu$m beam radius, the gain length is about 2.5 m. Even for a 100 pC, 5 fs pulse, the gain length is 1.6 m. Tuning the energy down, i.e. using a 200 MeV, 50 pC, 10 fs electron beam focused to $20\,\mu$m beam radius, reduces the gain length to 50 cm. Therefore, a 5 m long undulator would suffice for a laser-baser SASE-FEL operating at about 15 eV photon energy.

These examples show that undulators with short periods are more effective for reducing the wavelength than increasing the electron energy. This is followed by the Garching group (Grüner *et al.* , [90]) with a 5 mm period length undulator. Furthermore, beam focusing is essential to keep the current density high and constant over the undulator length. Therefore, spatially stable electron beams must be generated.

6.3.3 Seeded FEL

If a synchrotron radiation source is based on laser-accelerated electron beams, a short-pulse high-power laser system is present. Therefore it is rather simple to split the laser pulses at some point and establish several highly synchronized laser beams. Power, pulse duration, wavelength and delay of those beams may be chosen freely.

With a second ultra-short laser beam it is possible to generate high harmonics of the laser wavelength (HHG), either from gases [91, 92] or from solids [93, 94]. Those harmonics can can range up to the keV range and are ideal as seed for a FEL. Advantageous are the facts that this radiation takes the spatial and temporal coherence of the driving laser pulse and may have sub-femtosecond pulse durations. Furthermore, no synchronization problems will occur between pump and seed as they have a common source. Similar schemes are proposed for conventional synchrotron radiation facilities, called High-Gain Harmonic Generation (HGHG) and self-seeding [95]. However, the pulse durations are still limited by conventional accelerator technology, whereas an all-optical approach may access the sub-femtosecond range.

6.3.4 Synchronism

Nowadays, conventional synchrotron radiation facilities pursue a route to shorten their pulses. From a conventional accelerator, the electron pulses are several 10 ps long. With big efforts, the pulse duration may be reduced to $\sim$ 100 fs. But if the radiation pulses allow for atomic spatial resolution, it is natural that also dynamics with an atomic timescale are of interest. For that, pulse durations of the order of femtoseconds or shorter are needed. Furthermore, dynamics are studies via pump-probe experiments, for what two short pulses with a precise delay between them are necessary.

At conventional facilities, many efforts must be undertaken in order to meet those demands. The best working scheme uses a chirped electron pulse with some final compression [96, 5]. In addition, a femtosecond laser which delivers the pump pulses for time-resolved experiments is synchronized to the accelerator radio-frequency. But this synchronism is the main difficulty. The actual delay between both must be measured for every shot. This can be done via electro-optic sampling [78, 97]. This technique has a limited time resolution to about 50 fs due to frequency ranges of the used nonlinear electro-optic materials.

All those problems can be easily solved at laser-driven synchrotron radiation sources. As mentioned above, the laser system can be designed such that several pulses with

different properties can be produced from one optical oscillator. For pump-probe experiments, the pump pulse is usually a short pulse of weak intensity, and the probe pulse would be a synchrotron radiation pulse generated from a relativistically intense laser pulse via a laser-plasma accelerator. Then, the time resolution is limited by the laser pulse duration which is also the natural limit in that case.

6.3.5 Flexibility

Furthermore, many methods of ultrafast and relativistic optics could be added and mixed. For instance, the pump wavelength could be shifted in a wide range from UV wavelengths to the IR range via parametric processes and frequency conversion, but the ultra-short pulse duration would be maintained. It can be also imagined that the synchrotron radiation pulses is be used for excitation since it has higher photon energies and therefore higher penetration depths. The probe pulse might then be an optical pulse or also a synchrotron pulse, generated by a second laser-plasma accelerator and undulator, depending on the purpose – there is no principle restriction. Further it is possible to leave out one undulator and use the short and energetic electron pulse directly for pump or probe, or to use different laser-plasma interactions to generate proton or ion pulses [98, 99, 100].

6.3.6 Size, costs and operation

In comparison to a conventional synchrotron radiation facility, a laser-based one would be much smaller and less expensive. No large buildings for a power-consuming accelerator with lots of radiation shielding would be needed. They just need a table-top laser system and can be afforded and operated by a university institute in a university lab. Of course, instead of up to 30 simultaneous beamlines with highly reliable radiation properties, only one experiment could be carried out at a time. But there are only about 70 synchrotron radiation facilities running [101] which attract a large user community due to the various applications [4]. Therefore it is worth to explore the capabilities of laser-based synchrotron radiation facilities. In the worst case, they are just additional sources, providing more access to users. But they promise to be the ideal choice for experiments with high time-resolution. This is already a demand from the users, but difficult to meet by conventional facilities. So, it might be the right time for laser-plasma accelerators to take this chance and show their potential.

Bibliography

[1] Laue, M. v. "Concerning the detection of x-ray interferences". Nobel prize laureate lecture (1914).

[2] *X-Ray Data Booklet* (Center for X-ray Optics and Advanced Light Source, Lawrence Berkeley National Laboratory).

[3] Attwood, D. T. *Soft X-Rays and Extreme Ultraviolet Radiation* (Cambridge University Press) (2000).

[4] Bilderback, D. H., Elleaume, P., and Weckert, E. "Review of third and next generation synchrotron light sources". Journal Of Physics B - Atomic Molecular And Optical Physics **38**(9), S773–S797 (2005).

[5] Ayvazyan, V., Baboi, N., Bahr, J., et al. "First operation of a free-electron laser generating gw power radiation at 32 nm wavelength". European Physical Journal D **37**(2), 297–303 (2006).

[6] Chapman, H., Barty, A., Bogan, M., et al. "Femtosecond diffractive imaging with a soft-x-ray free-electron laser". Nature Physics **2**, 839–843 (2006).

[7] Tajima, T. and Dawson, J. M. "Laser electron-accelerator". Physical Review Letters **43**(4), 267–270 (1979).

[8] Strickland, D. and Mourou, G. "Compression of amplified chirped optical pulses". Optics Communications **56**(3), 219–221 (1985).

[9] Mangles, S., Murphy, C., Najmudin, Z., et al. "Monoenergetic beams of relativistic electrons from intense laser-plasma interactions". Nature **431**, 535–538 (2004).

[10] Geddes, C., Toth, C., van Tilborg, J., et al. "High-quality electron beams from a laser wakefield accelerator using plasma-channel guiding". Nature **431**, 538–541 (2004).

[11] Faure, J., Glinec, Y., Pukhov, A., et al. "A laser-plasma accelerator producing monoenergetic electron beams". Nature **431**, 541–544 (2004).

[12] Osterhoff, J., Popp, A., Major, Z., et al. "Generation of stable, low-divergence electron beams by laser-wakefield acceleration in a steady-state-flow gas cell". Physical Review Letters **101**(8), 085002 (2008).

[13] Faure, J., Rechatin, C., Norlin, A., et al. "Controlled injection and acceleration of electrons in plasma wakefields by colliding laser pulses". Nature **444**, 737–739 (2006).

[14] Leemans, W., Nagler, B., Gonsalves, et al. "Gev electron beams from a centimetre-scale accelerator". Nature Physics **2**, 696–699 (2006).

[15] Karsch, S., Osterhoff, J., Popp, A., et al. "Gev-scale electron acceleration in a gas-filled capillary discharge waveguide". New Journal Of Physics **9**, 415 (2007).

[16] Pittman, M., Ferré, S., Rousseau, J., et al. "Design and characterization of a near-diffraction-limited femtosecond 100-TW 10-Hz high-intensity laser system". Applied Physics B - Lasers And Optics **74**(6), 529–535 (2002).

[17] Esarey, E., Sprangle, P., Krall, J., et al. "Overview of plasma-based accelerator concepts". IEEE Transactions on Plasma Science **24**(2), 252–288 (1996).

[18] Pukhov, A., Sheng, Z. M., and Meyer-ter Vehn, J. "Particle acceleration in relativistic laser channels". Physics Of Plasmas **6**(7), 2847–2854 (1999).

[19] Pukhov, A. and Meyer-ter Vehn, J. "Laser wake field acceleration: the highly nonlinear broken-wave regime". Applied Physics B - Lasers And Optics **74**, 355–361 (2002).

[20] "Euroleap: European laser electron controlled acceleration in plasmas to gev energy range".

[21] Schlenvoigt, H. P., Haupt, K., Debus, A., et al. "A compact synchrotron radiation source driven by a laser-plasma wakefield accelerator". Nature Physics **4**(2), 130–133 (2008).

[22] Schlenvoigt, H. P., Haupt, K., Debus, A., et al. "Synchrotron radiation from laser-accelerated monoenergetic electrons". Ieee Transactions On Plasma Science **36**(4), 1773–1781 (2008).

[23] Kaluza, M., Schlenvoigt, H.-P., Mangles, S., et al. "Visualization of the electron-acceleration process in a table-top laser-plasma accelerator" to be published – submitted.

[24] Sarachik, E. S. and Schappert, G. T. "Classical theory of scattering of intense laser radiation by free electrons". Physical Review D **1**(10), 2738 (1970).

[25] Esarey, E., Ride, S. K., and Sprangle, P. "Nonlinear thomson scattering of intense laser-pulses from beams and plasmas". Physical Review E **48**(4), 3003–3021 (1993).

[26] Mangles, S. *Measurements of Relativistic Electrons from Intense Laser-Plasma Interactions*. Ph.D. thesis, Plasma Physics Group, Imperial College London (2005).

[27] Kruer, W. L. *The physics of laser plasma interactions* (Addison-Wesley) (1988).

[28] Quesnel, B. and Mora, P. "Theory and simulation of the interaction of ultraintense laser pulses with electrons in vacuum". Physical Review E **58**(3), 3719–3732 (1998).

[29] Bauer, D., Mulser, P., and Steeb, W. H. "Relativistic ponderomotive force, uphill acceleration, and transition to chaos". Physical Review Letters **75**(25), 4622–4625 (1995).

[30] Mori, W. B. "The physics of the nonlinear optics of plasmas at relativistic intensities for short-pulse lasers". IEEE Journal Of Quantum Electronics **33**(11), 1942–1953 (1997).

[31] Decker, C. D. and Mori, W. B. "Group-velocity of large-amplitude electromagnetic-waves in a plasma". Physical Review Letters **72**(4), 490–493 (1994).

[32] Sun, G. Z., Ott, E., Lee, Y. C., et al. "Self-focusing of short intense pulses in plasmas". Physics Of Fluids **30**(2), 526–532 (1987).

[33] Batani, D., Joachain, C. J., Martellucci, S., et al. (eds.). *Atoms, Solids, and Plasmas in Super-Intense Laser Fields* (Kluwer Academic) (2001).

[34] Chen, F. F. *Introduction to Plasma Physics and Controlled Fusion* (Plenum Press).

[35] Brinkmann, R., Flöttmann, K., Roßbach, J., et al. "Tesla technical design report, part ii: The accelerator" (2001).

[36] Gorbunov, L. M. and Kirsanov, V. I. "Excitation of plasma-waves by short electromagnetic-wave packets". Zhurnal Eksperimentalnoi I Teoreticheskoi Fiziki **93**(2), 509–518 (1987).

[37] Sprangle, P., Esarey, E., Ting, A., et al. "Laser wakefield acceleration and relativistic optical guiding". Applied Physics Letters **53**(22), 2146–2148 (1988).

[38] Geddes, C. G. R., Toth, C., van Tilborg, J., et al. "Production of high-quality electron bunches by dephasing and beam loading in channeled and unchanneled laser plasma accelerators". Physics Of Plasmas **12**(5), 056709 (2005).

[39] Malka, V., Faure, J., Marques, J. R., et al. "Characterization of electron beams produced by ultrashort (30 fs) laser pulses". Physics Of Plasmas **8**(6), 2605–2608 (2001).

[40] Malka, V., Fritzler, S., Lefebvre, E., et al. "Electron acceleration by a wake field forced by an intense ultrashort laser pulse". Science **298**(5598), 1596–1600 (2002).

[41] Najmudin, Z., Krushelnick, K., Clark, E. L., et al. "Self-modulated wakefield and forced laser wakefield acceleration of electrons". Physics Of Plasmas **10**(5), 2071–2077 (2003).

[42] Pukhov, A., Gordienko, S., Kiselev, S., et al. "The bubble regime of laser-plasma acceleration: monoenergetic electrons and the scalability". Plasma Physics And Controlled Fusion **46**, B179–B186 (2004).

[43] Kostyukov, I., Pukhov, A., and Kiselev, S. "Phenomenological theory of laser-plasma interaction in "bubble" regime". Physics Of Plasmas **11**(11), 5256–5264 (2004).

[44] Gordienko, S. and Pukhov, A. "Scalings for ultrarelativistic laser plasmas and quasimonoenergetic electrons". Physics Of Plasmas **12**(4), 043109 (2005).

[45] Malka, V., Faure, J., Glinec, Y., et al. "Monoenergetic electron beam optimization in the bubble regime". Physics Of Plasmas **12**(5), 056702 (2005).

[46] Hidding, B., Amthor, K. U., Liesfeld, B., et al. "Generation of quasimonoenergetic electron bunches with 80-fs laser pulses". Physical Review Letters **96**(10), 105004 (2006).

[47] Gahn, C., Tsakiris, G. D., Pukhov, A., et al. "Multi-mev electron beam generation by direct laser acceleration in high-density plasma channels". Physical Review Letters **83**(23), 4772–4775 (1999).

[48] Lau, Y. Y., He, F., Umstadter, D. P., et al. "Nonlinear thomson scattering: A tutorial". Physics Of Plasmas **10**(5), 2155–2162 (2003).

[49] Liesfeld, B. *A Photon Collider at Relativistic Intensity*. Ph.D. thesis, Friedrich-Schiller-Universität Jena (2006).

[50] Thomas, A. G. R., Mangles, S. P. D., Najmudin, Z., et al. "Measurements of wave-breaking radiation from a laser-wakefield accelerator". Physical Review Letters **98**(5) (2007).

[51] Hutchinson, I. H. *Principles of Plasma Diagnostics* (Cambridge University Press).

[52] Tanaka, T. and Kitamura, H. "Spectra: a synchrotron radiation calculation code". Journal Of Synchrotron Radiation **8**, 1221–1228 (2001).

[53] Leemans, W. P., Esarey, E., van Tilborg, J., et al. "Radiation from laser accelerated electron bunches: Coherent terahertz and femtosecond x-rays". IEEE Transactions on Plasma Science **33**(1), 8–22 (2005).

[54] van Tilborg, J., Schroeder, C., Filip, C., et al. "Temporal characterization of femtosecond laser-plasma-accelerated electron bunches using terahertz radiation". Physical Review Letters **96**(1), 014801 (2006).

[55] van Tilborg, J., Schroeder, C. B., Filip, C. V., et al. "Terahertz radiation as a bunch diagnostic for laser-wakefield-accelerated electron bunches". Physics Of Plasmas **13**(5), 056704 (2006).

[56] Ohkubo, T., Maekawa, A., Tsujii, R., et al. "Temporal characteristics of monoenergetic electron beams generated by the laser wakefield acceleration". Physical Review Special Topics-Accelerators And Beams **10**(3), 031301 (2007).

[57] Bonifacio, R., Pellegrini, C., and Narducci, L. M. "Collective instabilities and high-gain regime in a free-electron laser". Optics Communications **50**(6), 373–378 (1984).

[58] Dattoli, G., Renieri, A., and Torre, A. *Lectures on Free Electron Laser Theory and related Topics* (World Scientific) (1993).

[59] Clarke, J. A. *The Science and Technology of Undulators and Wigglers* (Oxford Science Publications) (2004).

[60] Malka, V., Coulaud, C., Geindre, J. P., et al. "Characterization of neutral density profile in a wide range of pressure of cylindrical pulsed gas jets". Review Of Scientific Instruments **71**(6), 2329–2333 (2000).

[61] Schwoerer, H., Gibbon, P., Dusterer, S., et al. "Mev x rays and photoneutrons from femtosecond laser-produced plasmas". Physical Review Letters **86**(11), 2317–2320 (2001).

[62] Liesfeld, B., Bernhardt, J., Amthor, K. U., et al. "Single-shot autocorrelation at relativistic intensity". Applied Physics Letters **86**(16), 16110 (2005).

[63] Schwoerer, H., Liesfeld, B., Schlenvoigt, H. P., et al. "Thomson-backscattered x rays from laser-accelerated electrons". Physical Review Letters **96**(1), 014802 (2006).

[64] Amthor, K.-U. *Laser Plasma Accelerators for Charged Particles*. Ph.D. thesis, Friedrich-Schiller-Universität Jena (2006).

[65] Kaluza, M. C., Santala, M. I. K., Schreiber, J., et al. "Time-sequence imaging of relativistic laser-plasma interactions using a novel two-color probe pulse". Applied Physics B - Lasers And Optics **92**(4), 475–479 (2008).

[66] Najmudin, Z., Krushelnick, K., Tatarakis, M., et al. "The effect of high intensity laser propagation instabilities on channel formation in underdense plasmas". Physics Of Plasmas **10**(2), 438–442 (2003).

[67] Benattar, R., Popovics, C., and Sigel, R. "Polarized-light interferometer for laser fusion studies". Review Of Scientific Instruments **50**(12), 1583–1585 (1979).

[68] Maksimchuk, A., Reed, S., Bulanov, S. S., et al. "Studies of laser wakefield structures and electron acceleration in underdense plasmas". Physics Of Plasmas **15**(5), 056703 (2008).

[69] Glinec, Y., Faure, J., Guemnie-Tafo, A., et al. "Absolute calibration for a broad range single shot electron spectrometer". Review Of Scientific Instruments **77**(10), 103301 (2006).

[70] van der Geer, S. and de Loos, M. "GPT – General Particle Tracer".

[71] Tanaka, K. A., Yabuuchi, T., Sato, T., et al. "Calibration of imaging plate for high energy electron spectrometer". Review Of Scientific Instruments **76**(1), 013507 (2005).

[72] Jackson, J. *Classical Electrodynamics*.

[73] Thomas, A. G. R., Najmudin, Z., Mangles, S. P. D., et al. "Effect of laser-focusing conditions on propagation and monoenergetic electron production in laser-wakefield accelerators". Physical Review Letters **98**(9) (2007).

[74] Walton, B. *Optical diagnostics of laser plasma particle acceleration experiments*. Ph.D. thesis, Plasma Physics Group, Imperial College London (2004).

[75] Fonseca, R., Silva, L., Tsung, F., et al. "Osiris: A three-dimensional, fully relativistic particle in cell code for modeling plasma based accelerators". In *Computational Science – ICCS 2002* (Springer), vol. 2331 of *Lecture Notes in Computer Science*, pages 342 – 351 (2002).

[76] Lu, W., Huang, C., Zhou, M., et al. "Nonlinear theory for relativistic plasma wakefields in the blowout regime". Physical Review Letters **96**(16), 165002 (2006).

[77] Arnold, A., Buttig, H., Janssen, D., et al. "A high-brightness srf photoelectron injector for fel light sources". Nuclear Instruments & Methods In Physics Research Section A - Accelerators Spectrometers Detectors And Associated Equipment **593**(1-2), 57–62 (2008).

[78] Berden, G., Gillespie, W. A., Jamison, S. P., et al. "Benchmarking of electro-optic monitors for femtosecond electron bunches". Physical Review Letters **99**(16), 164801 (2007).

[79] Schroeder, C. B., Esarey, E., van Tilborg, J., et al. "Theory of coherent transition radiation generated at a plasma-vacuum interface". Physical Review E **69**(1), 016501 (2004).

[80] Glinec, Y., Faure, J., Norlin, A., et al. "Observation of fine structures in laser-driven electron beams using coherent transition radiation". Physical Review Letters **98**(19), 194801 (2007).

[81] Geissler, M., Schreiber, J., and Meyer-Ter-Vehn, J. "Bubble acceleration of electrons with few-cycle laser pulses". New Journal Of Physics **8**, 186 (2006).

[82] Spence, D. J. and Hooker, S. M. "Investigation of a hydrogen plasma waveguide". Physical Review E **6302**(1), 015401 (2001).

[83] Nakamura, K., Nagler, B., Toth, C., et al. "Gev electron beams from a centimeter-scale channel guided laser wakefield accelerator". Physics Of Plasmas **14**(5), 056708 (2007).

[84] Hooker, S. M., Brunetti, E., Esarey, E., et al. "Gev plasma accelerators driven in waveguides". Plasma Physics And Controlled Fusion **49**(12B), B403–B410 (2007).

[85] Rowlands-Rees, T. P., Kamperidis, C., Kneip, S., et al. "Laser-driven acceleration of electrons in a partially ionized plasma channel". Physical Review Letters **100**(10), 105005 (2008).

[86] Broks, B. H. P., Garloff, K., and van der Mullen, J. J. A. M. "Nonlocal-thermal-equilibrium model of a pulsed capillary discharge waveguide". Physical Review E **71**(1), 016401 (2005).

[87] Broks, B. H. P., van Dijk, W., and van der Mullen, J. J. A. M. "Parameter study of a pulsed capillary discharge waveguide". Journal Of Physics D - Applied Physics **39**(11), 2377–2383 (2006).

[88] Broks, B. H. P., Van Dijk, W., van der Mullen, J. J. A. W., et al. "Modeling of a square pulsed capillary discharge waveguide for interferometry measurements". Physics Of Plasmas **14**(2), 023501 (2007).

[89] Nicolai, M. "Bau und Charakterisierung einer Plasma-Kapillare für Hochintensitätslaser-Plasma-Experimente". Diplomarbeit (diploma thesis), Friedrich-Schiller-Universität Jena (2008).

[90] Grüner, F., Becker, S., Schramm, U., et al. "Design considerations for table-top, laser-based vuv and x-ray free electron lasers". Applied Physics B - Lasers And Optics **86**(3), 431–435 (2007).

[91] Agostini, P. and DiMauro, L. F. "The physics of attosecond light pulses". Reports On Progress In Physics **67**(6), 813–855 (2004).

[92] Winterfeldt, C., Spielmann, C., and Gerber, G. "Colloquium: Optimal control of high-harmonic generation". Reviews Of Modern Physics **80**(1), 117–140 (2008).

[93] Dromey, B., Zepf, M., Gopal, A., et al. "High harmonic generation in the relativistic limit". Nature Physics **2**(7), 456–459 (2006).

[94] Quere, F., Thaury, C., George, H., et al. "Basic mechanisms of laser high-order harmonic generation from plasma mirrors". Journal Of Modern Optics **55**(16), 2711–2721 (2008).

[95] Feldhaus, J., Arthur, J., and Hastings, J. B. "X-ray free-electron lasers". Journal Of Physics B - Atomic Molecular And Optical Physics **38**(9), S799–S819 (2005).

[96] Bentson, L., Bolton, P., Bong, E., et al. "Fel research and development at the slac sub-picosecond photon source, spps". Nuclear Instruments & Methods In Physics Research Section A - Accelerators Spectrometers Detectors And Associated Equipment **507**(1-2), 205–209 (2003).

[97] Cavalieri, A. L., Fritz, D. M., Lee, S. H., et al. "Clocking femtosecond x rays". Physical Review Letters **94**(11), 114801 (2005).

[98] Hegelich, B. M., Albright, B. J., Cobble, J., et al. "Laser acceleration of quasi-monoenergetic mev ion beams". Nature **439**(7075), 441–444 (2006).

[99] Schwoerer, H., Pfotenhauer, S., Jäckel, O., et al. "Laser-plasma acceleration of quasi-monoenergetic protons from microstructured targets". Nature **439**(7075), 445–448 (2006).

[100] Pfotenhauer, S. M., Jäckel, O., Sachtleben, A., et al. "Spectral shaping of laser generated proton beams". New Journal Of Physics **10**, 033034 (2008).

[101] www.lightsources.org.

List of Figures

Acknowledgments

Ehrenwörtliche Erklärung

Ich erkläre hiermit ehrenwörtlich, dass ich die vorliegende Arbeit selbständig, ohne unzulässige Hilfe Dritter und ohne Benutzung anderer als der angegebenen Hilfsmittel und Literatur angefertigt habe. Die aus anderen Quellen direkt oder indirekt übernommenen Daten und Konzepte sind unter Angabe der Quelle gekennzeichnet.

Bei der Auswahl und Auswertung folgenden Materials haben mir die nachstehend aufgeführten Personen in der jeweils beschriebenen Weise unentgeltlich geholfen:

1. Kerstin Haupt: Design und Charakterisierung des Undulators; Vorauswahl und Vermessung von Elektronen- und optischen Spektren

2. Alexander Debus: Berechnung von Synchrotronstrahlungsspektren aus gemessenen Elektronenspektren; Kalibrierungen der Spektrometer

3. Prof. Dr. Malte Kaluza: Auswertung von Polarogrammen

4. Dr. Stuart Mangles (Imperial College, London): PIC-Simulationen mit OSIRIS zu den gemessenen Magnetfeldern

5. Sebastinan Podleska: ZEMAX-Simulation der Abbildung der Synchrotronstrahlung in das Spektrometer

Weitere Personen waren an der inhaltlich-materiellen Erstellung der vorliegenden Arbeit nicht beteiligt. Insbesondere habe ich hierfür nicht die entgeltliche Hilfe von Vermittlungs- bzw. Beratungsdiensten (Promotionsberater oder andere Personen) in Anspruch genommen. Niemand hat von mir unmittelbar oder mittelbar geldwerte Leistungen für Arbeiten erhalten, die im Zusammenhang mit dem Inhalt der vorgelegten Dissertation stehen.

Die Arbeit wurde bisher weder im In- noch im Ausland in gleicher oder ähnlicher Form einer anderen Prüfungsbehörde vorgelegt.

Die geltende Promotionsordnung der Physikalisch-Astronomischen Fakultät ist mir bekannt.

Ich versichere ehrenwörtlich, dass ich nach bestem Wissen die reine Wahrheit gesagt und nichts verschwiegen habe.

Jena, den